UNIVERSIDADE FEDERAL DE CATALÃO
INSTITUTO DE MATEMÁTICA E TECNOLOGIA
PROGRAMA DE PÓS-GRADUAÇÃO EM MODELAGEM E OTIMIZAÇÃO

Emanuel Victor Borges de Morais Cruvinel

INVESTIGATION OF DISSIPATIVE EFFECTS IN PERIODIC STRUCTURES

MASTER'S DISSERTATION

CATALÃO – GO, 2022

UNIVERSIDADE FEDERAL DE GOIÁS
UNIDADE ACADÊMICA ESPECIAL DE MATEMÁTICA E TECNOLOGIA

TERMO DE CIÊNCIA E DE AUTORIZAÇÃO (TECA) PARA DISPONIBILIZAR VERSÕES ELETRÔNICAS DE TESES E DISSERTAÇÕES NA BIBLIOTECA DIGITAL DA UFG

Na qualidade de titular dos direitos de autor, autorizo a Universidade Federal de Goiás (UFG) a disponibilizar, gratuitamente, por meio da Biblioteca Digital de Teses e Dissertações (BDTD/UFG), regulamentada pela Resolução CEPEC nº 832/2007, sem ressarcimento dos direitos autorais, de acordo com a Lei 9.610/98, o documento conforme permissões assinaladas abaixo, para fins de leitura, impressão e/ou download, a título de divulgação da produção científica brasileira, a partir desta data.

O conteúdo das Teses e Dissertações disponibilizado na BDTD/UFG é de responsabilidade exclusiva do autor. Ao encaminhar o produto final, o autor(a) e o(a) orientador(a) firmam o compromisso de que o trabalho não contém nenhuma violação de quaisquer direitos autorais ou outro direito de terceiros.

1. Identificação do material bibliográfico

[x] Dissertação [ ] Tese

2. Nome completo do autor

Emanuel Victor Borges de Morais Cruvinel

3. Título do trabalho

INVESTIGATION OF DISSIPATIVE EFFECTS IN PERIODIC STRUCTURES

4. Informações de acesso ao documento (este campo deve ser preenchido pelo orientador)

Concorda com a liberação total do documento [x] SIM [ ] NÃO[1]

[1] Neste caso o documento será embargado por até um ano a partir da data de defesa. Após esse período, a possível disponibilização ocorrerá apenas mediante:
a) consulta ao(à) autor(a) e ao(à) orientador(a);
b) novo Termo de Ciência e de Autorização (TECA) assinado e inserido no arquivo da tese ou dissertação.
O documento não será disponibilizado durante o período de embargo.
Casos de embargo:
- Solicitação de registro de patente;
- Submissão de artigo em revista científica;
- Publicação como capítulo de livro;
- Publicação da dissertação/tese em livro.

Obs. Este termo deverá ser assinado no SEI pelo orientador e pelo autor.

Documento assinado eletronicamente por **Romes Antonio Borges**, **Orientador**, em 29/04/2022, às 14:32, conforme horário oficial de Brasília, com fundamento no § 3º do art. 4º do Decreto nº 10.543, de 13 de novembro de 2020.

Documento assinado eletronicamente por **EMANUEL VICTOR BORGES DE MORAIS CRUVINEL**, **Discente**, em 02/05/2022, às 08:25, conforme horário oficial de Brasília, com fundamento no § 3º do art. 4º do Decreto nº 10.543, de 13 de novembro de 2020.

A autenticidade deste documento pode ser conferida no site https://sei.ufg.br/sei/controlador_externo.php?acao=documento_conferir&id_orgao_acesso_externo=0, informando o código verificador **2864417** e o código CRC **99E48638**.

EMANUEL VICTOR BORGES DE MORAIS CRUVINEL

INVESTIGATION OF DISSIPATIVE EFFECTS IN PERIODIC STRUCTURES

Master's Dissertation submitted to the Institute of Mathematics and Technology of the Federal University of Catalão, as a fulfillment of the requirements for the degree of Master in Modeling and Optimization.
Focus Area: Modeling and Optimization.

Advisor:
Romes A. Borges

Co-Advisor:
Domingos A. Rade

CATALÃO – GO

2022

Ficha de identificação da obra elaborada pelo autor, através do
Programa de Geração Automática do Sistema de Bibliotecas da UFCAT.

Cruvinel, Emanuel Victor Borges de Morais
Investigation of Dissipative Effects in Periodic Structures / Emanuel Victor Borges de Morais Cruvinel. - 2022.
106, f.

Orientador: Prof. Dr. Romes Antônio Borges; co-orientador Prof. Dr. Domingos Alves Rade.
Dissertação (Mestrado) - Universidade Federal de Catalão, Instituto de Matemática e Tecnologia, Catalão, Programa de Pós-Graduação em Modelagem e Otimização, Catalão, 2022.
Bibliografia.
Inclui siglas, abreviaturas, símbolos, gráfico, tabelas, lista de figuras, lista de tabelas.

1. periodic structures. 2. stop bands. 3. band gaps. 4. damping . 5. acoustic metamaterials. I. Borges, Romes Antônio, orient. II. Título.

CDU 621

UNIVERSIDADE FEDERAL DE GOIÁS

UNIDADE ACADÊMICA ESPECIAL DE MATEMÁTICA E TECNOLOGIA

ATA DE DEFESA DE DISSERTAÇÃO

Ata nº 14 da sessão de Defesa de Dissertação de **Emanuel Victor Borges de Morais Cruvinel**, que confere o título de **Mestre(a) em Modelagem e Otimização**, na área de concentração em **Modelagem e Otimização**.

Aos vinte e nove dias do mês de abril de 2022, a partir das 09h00min, na sala web-conferência, realizou-se a sessão pública de Defesa de Dissertação, intitulada *"INVESTIGATION OF DISSIPATIVE EFFECTS IN PERIODIC STRUCTURES"* nas dependências da Universidade Federal de Catalão, onde os programas de pós-graduação *Stricto Sensu* em funcionamento encontram-se provisoriamente vinculados à Universidade Federal de Goiás, em virtude de procedimentos técnicos relacionados à CAPES, já sendo realizada a transferência da Biblioteca Digital de Dissertações e Teses (BDTD). Assim, justifica-se os nomes das instituições neste documento, uma no cabeçalho (UFG), outra no corpo do texto (UFCAT). Os trabalhos foram instalados pelo(a) **Orientador(a), Professor(a) Doutor(a) Romes Antonio Borges (PPGMO/IMTec/UFCAT), com a participação dos demais membros da Banca Examinadora: Professor(a) Doutor(a) Domingos Alves Rade (ITA), Coorientador, Professor(a) Doutor(a) Adriano Todorovic Fabro (FT / UnB), membro titular externo; Professor(a) Doutor(a) José dos Reis Vieira de Moura Júnior (PPGMO/IMTec/UFCAT), membro titular interno.** A Banca Examinadora reuniu-se em sessão secreta a fim de concluir o julgamento da Dissertação, tendo sida o candidato (X) Aprovado ( ) Reprovado pelos seus membros. Proclamados os resultados pelo **Professor Doutor Romes Antonio Borges**, Presidente da Banca Examinadora, foram encerrados os trabalhos e, para constar, lavrou-se a presente ata que é assinada pelos Membros da Banca Examinadora, aos vinte e nove dias do mês de abril de dois mil e vinte e dois.

Obs: "*Banca Examinadora de Qualificação/Defesa Pública de Dissertação/Tese realizada em conformidade com a Portaria da CAPES n. 36, de 19 de março de 2020, de acordo com seu segundo artigo:*

Art. 2o A suspensão de que trata esta Portaria não afasta a possibilidade de defesas de tese utilizando tecnologias de comunicação à distância, quando admissíveis pelo programa de pós-graduação stricto sensu, nos termos da regulamentação do Ministério da Educação."

TÍTULO SUGERIDO PELA BANCA

Documento assinado eletronicamente por **Romes Antonio Borges**, **Professor do Magistério Superior**, em 29/04/2022, às 11:32, conforme horário oficial de Brasília, com fundamento no § 3º do art. 4º do Decreto nº 10.543, de 13 de novembro de 2020.

Documento assinado eletronicamente por **ADRIANO TODOROVIC FABRO**, **Usuário Externo**, em 29/04/2022, às 11:33, conforme horário oficial de Brasília, com fundamento no § 3º do art. 4º do Decreto nº 10.543, de 13 de novembro de 2020.

Documento assinado eletronicamente por **Domingos Alves Rade**, **Usuário Externo**, em 29/04/2022, às 11:34, conforme horário oficial de Brasília, com fundamento no § 3º do art. 4º do Decreto nº 10.543, de 13 de novembro de 2020.

Documento assinado eletronicamente por **Jose Dos Reis Vieira De Moura Junior**, **Professor do Magistério Superior**, em 29/04/2022, às 11:37, conforme horário oficial de Brasília, com fundamento no § 3º do art. 4º do Decreto nº 10.543, de 13 de novembro de 2020.

A autenticidade deste documento pode ser conferida no site https://sei.ufg.br/sei/controlador_externo.php?acao=documento_conferir&id_orgao_acesso_externo=0, informando o código verificador **2864342** e o código CRC **6C366CBC**.

Referência: Processo nº 23070.018774/2022-82 SEI nº 2864342

RESUMO

CRUVINEL, E.V.B.M. Investigação dos efeitos dissipativos em estruturas periódicas. 2022. 106 p. Dissertação (Mestrado em Modelagem e Otimização) – Instituto de Matemática e Tecnologia, Universidade Federal de Catalão, Catalão – GO.

Estruturas periódicas são compostas de subestruturas idênticas ou células conectadas, com sua periodicidade caracterizada por descontinuidades geométricas ou materiais. Devido à periodicidade, estas estruturas apresentam características dinâmicas especiais, agindo como filtros mecânicos para ondas elásticas propagantes em intervalos específicos de frequência, conhecido como bandas atenuantes. A maior parte das investigações anteriores não levaram em consideração os efeitos de dissipação de energia. Entretanto, estruturas de engenharia dissipam energia através de vários mecanismos, por exemplo, devido ao atrito entre conexões, abertura e fechamento de micro trincas ou atrito interno. Dissipação de energia, também caracterizado como amortecimento vibracional, pode alterar as bandas de frequência da estrutura, logo modificando o comportamento da propagação de ondas. O objetivo desta dissertação é analisar o efeito do amortecimento na atenuação das ondas elásticas de estruturas periódicas quando submetidas à excitação harmônica forçada. Os modelos de amortecimento viscoso, histerético e viscoelástico aplicados a quatro configurações de estruturas periódicas, com e sem ressonadores internos, modelados como sistemas de parâmetro concentrado massa-mola-amortecedor serão investigados. Tais modelos de amortecimento também serão aplicados para duas configurações de estruturas periódicas contínuas, a barra compósita e a viga sanduíche. Para cada configuração, as equações do movimento da célula unitária são deduzidas, e a matriz de transferência é implementada para modelar a propagação das ondas elásticas na estrutura periódica, além de obter a constante de propagação que permite a construção das curvas de dispersão. Diferentes níveis de amortecimento são considerados, e seus efeitos em passa bandas, bandas atenuantes e resposta da função em frequência serão analisados. É mostrado que a introdução do amortecimento em estruturas periódicas alteram as curvas de dispersão, aumentando o nível de atenuação nas regiões de passa banda. É mostrado também que para o caso do amortecimento viscoelástico, as bandas atenuantes se deslocam no eixo da frequência.

Palavras-chaves: estruturas periódicas , bandas atenuantes, band gaps, amortecimento, metamateriais acústicos.

ABSTRACT

CRUVINEL, E.V.B.M. Investigation of dissipative effects in periodic structures. 2022. 106 p. Master's degree in Modeling and Optimization – Institute of Mathematics and Technology, Federal University of Catalão, Catalão – GO - Brazil.

Periodic structures are composed of identical substructures or cells that are connected end to end in a similar manner, with their periodicity characterized by geometrical or material discontinuity. Due to their periodicity, these structures present special dynamic characteristics, acting as a mechanical filter for elastic waves propagating in specific frequency intervals, known as stop bands or band gaps. Most of previous investigations disregard energy dissipation effects. However, engineering structures dissipate energy by various mechanisms when they vibrate, for instance, due to friction at connections, opening and closing of material microcracks or internal material friction when deformed. Energy dissipation, also known as vibration damping, can alter frequency band structures, thus modifying the behavior of wave propagation. The purpose of this dissertation is to analyze the effects of damping on the attenuation of elastic waves in periodic structures when subjected to forced harmonic excitation. The viscous and hysteretic damping models are investigated when applied to four different configurations of periodic structures, with and without internal resonators, modeled as lumped mass-spring-damper subsystems. Also, these damping models will also be applied for periodic continuous structures, the composite rod and the sandwich beam. For each configuration, the equations of motion of the unit cell are derived, and the transfer matrix method is implemented to model the elastic wave propagation along the periodic structure and to obtain the propagation constant that allows the construction of dispersion curves. Different levels of damping are considered, and their effects in pass bands, stop bands and frequency response functions are analyzed. It is shown that the dispersion curves are altered when adding damping in periodic structures, increasing the attenuation level in the pass band regions. It is also shown that in the case of viscoelastic damping, the band gaps are shifted in the frequency axis.

Keywords: periodic structures, stop bands, band gaps, damping, acoustic metamaterials.

LIST OF FIGURES

LIST OF TABLES

SUMMARY

Chapter 1

INTRODUCTION

The increased complexity in engineering systems has led researchers to devote their attention in the obtention of materials with properties not commonly found in nature. This new class of materials is called metamaterials (CUI; LIU; SMITH, 2010; DEYMIER, 2013; BANERJEE, 2011). Recently, metamaterials have been received attention and investment from governments and companies due to potential technologies that they are able to deploy, ranging from sound filtering, seismic protection, ultrasonic sensors and super lens, to new antennas and vibration attenuation.

Metamaterials are particularly capable of handling electromagnetic and mechanical waves due to local resonances and scattering phenomena that arises from their geometric and/or material pattern. Metamaterials can also be tailored to withstand large mechanical loads where conventional materials would fail (INJETI; DARAIO; BHATTACHARYA, 2019).

Regarding antenna systems, Wu *et al.* (2005) studied the effect of using metamaterials as an antenna substrate. They concluded that metamaterials are capable of improving the antenna gain due to the manipulation of the effective permittivity and permeability of the electromagnetic field.

Metamaterials are able to increase images sharpness. In the optics field, Pendry (2000) used a slab of negative refractive index material to bring light to a perfect focus. The metamaterial used was a silver wire structure with lattice spacing, and it was capable of restoring the phase of electromagnetic propagating waves and the amplitude of evanescent states.

Another example of wave propagation control is found in Rudykh and Boyce (2014). The authors analyzed the propagation of elastic waves in a flexible, layered material with textured nanoscale wrinkles. Applying a mechanical load beyond the critical compression strain increases the wrinkles amplitudes of the interfacial layer, creating a system of periodic scatterers which reflects and interfere with wave propagation. The formation of wrinkling interfaces can be used to create frequency band gaps and filter undesirable frequencies.

As it was cited earlier, metamaterials are also employed in mechanical systems for

vibration attenuation. Such class of metamaterial is commonly composed of a pattern in geometry, material, or even both, and it is usually referred as periodic structure. Here, the central idea is to attenuate or even suppress the propagation of elastic waves in the structure, thus reducing the displacement amplitude levels of the mechanical system. Periodic structures are capable of filtering elastic waves, thus attenuating vibration on certain range of frequencies. Such periodicity may arise from the geometry of the structure, material property, or a combination of both. Two examples of periodicity in a rod are depicted in Figure 1.1:

Figure 1.1 – a) Homogeneous rod, b) Rod with geometric periodicity and c) Rod with material periodicity.

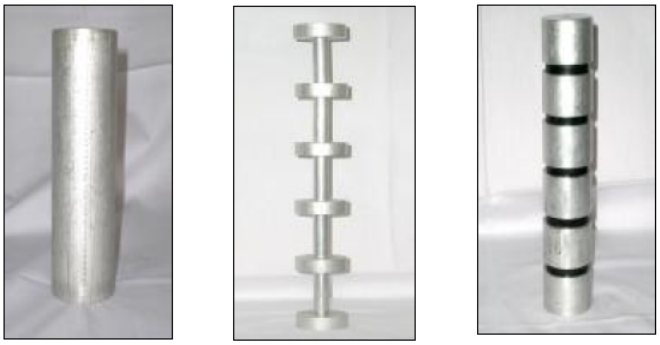

Source: (ASIRI; ALJAWI, 2006).

The phenomenon of elastic waves filtering occurs due to Bragg scattering or local resonances in the interface where material or geometric discontinuity is presented (SIGALAS; ECONOMOU, 1992). The frequency bands where vibration energy is not allowed to pass are called band gaps or stop bands, whereas the opposite is called pass bands.

The theory of periodic structures was first introduced by Brillouin (1946) and later on Mead (1970) extended the theory to many different mechanic structural designs. Since then, many other authors have been contributing to the study of periodic structures.

Common terminologies in the field of periodic structures are phononic crystals and acoustic metamaterials. The former terminology is applied to structures where the band gaps occur due to Bragg scattering, therefore the periodicity and position of the scatterers are very important to obtain desired properties (KHELIF; ADIBI, 2015). As for metamaterials, their structures usually involve local resonators, and normally resonate at lower frequencies compared to Bragg scattering. In this case, metamaterials might possess local resonances and Bragg scattering.

In Figure 1.2 it is shown an example of phononic crystal and metamaterial, represented by a mass-spring-damper system:

Figure 1.2 – a) An example of phononic crystal, b) An example of metamaterial

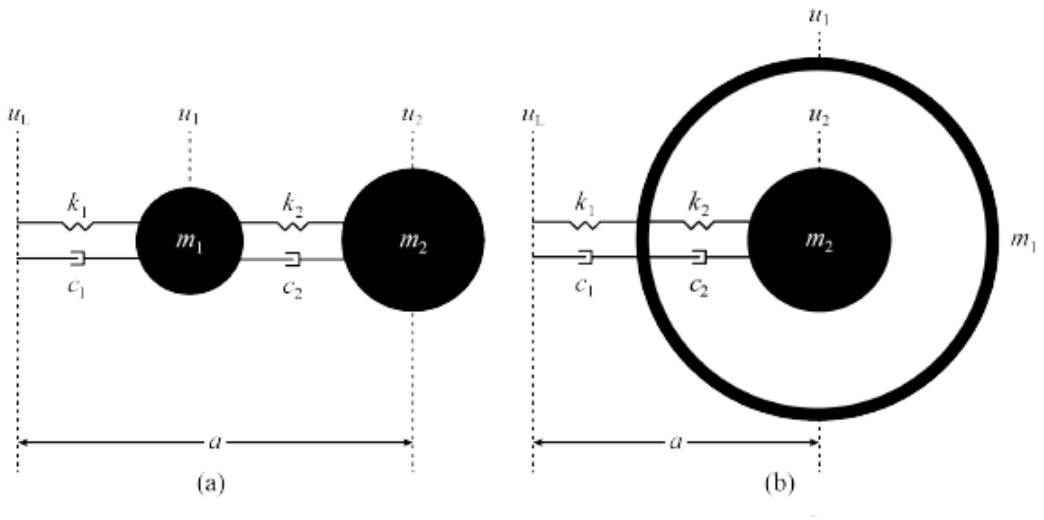

Source: (FRAZIER, 2015).

In Figure 1.3 it is depicted a dispersion diagram showing the band gaps originated by phononic crystals and metamaterials in Figure 1.2. The dispersion diagrams are divided in left and right panes from the origin (Wavenumber = 0), where the left side shows the attenuation factor and the right side shows the phase constant of the periodic structure.

Figure 1.3 – a) Phononic Crystal with band gaps due to Bragg scattering and b) Metamaterial with band gaps due to Bragg scattering and local resonances.

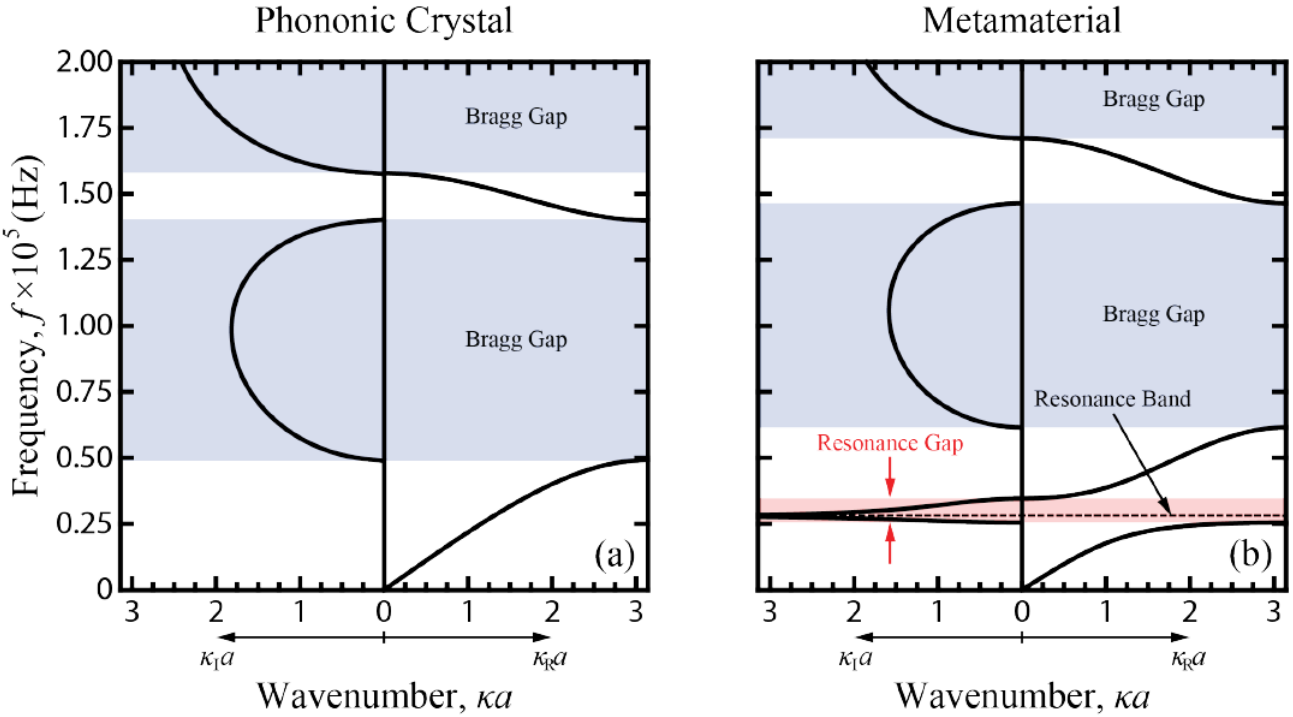

Source: (FRAZIER, 2015).

For the phononic crystal band frequency in Figure 1.3 a), it can be observed two band gaps region due to Bragg scattering, the first in a interval of 75 - 125 kHz and the second in 160 - 200 kHz. Inside these frequency range, the elastic waves are highly attenuated, decreasing the vibration amplitude across the structure. As for the other frequency ranges, the elastic waves can freely propagate, thus being called pass bands.

The acoustic metamaterial in Figure 1.3 b) shows three band gap regions. Notice in this case the existence of a band gap at low frequency of 25 kHz caused by the resonance of the mass m_2 located inside mass m_1. This local resonance is what defines the term acoustic metamaterial rather than phononic crystal. In the same way, this local resonance attenuates the propagation of elastic waves when the structure is submitted to this particularly low frequency, thus mitigating the amplitude of the vibration in this configuration of periodic structure.

For practical applications, in Figure 1.4 it is shown an example of metamaterial structure (ASSOUAR *et al.*, 2012) utilized for low frequency sound attenuation:

Figure 1.4 – Metamaterial for low frequency sound attenuation.

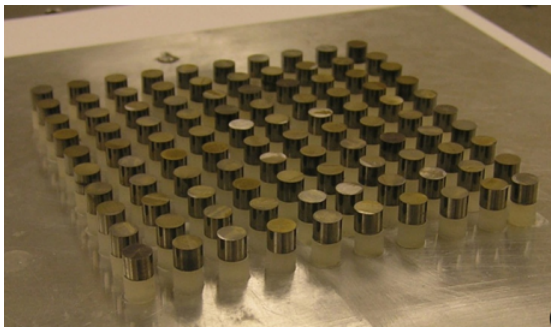

Source: (ASSOUAR *et al.*, 2012).

The aluminum plate is arranged with a periodic array of composite stubs made of tungsten and silicone rubber. Using tungsten and silicone rubber thicknesses of 8 mm and 5 mm, the metamaterial was capable of attenuating sound waves in the frequency range of 800 - 2800 Hz.

For automotive systems, Asiri and Aljawi (2006) studied the design of a periodic mount to suppress vibration transmission from a vehicle engine to the car body. By using a periodic mount with material and geometrical discontinuities, a desired reduced transmissibility was achieved.

Another example of phononic crystal applied in automotive systems can be found in (WAN; SHAO; CHENG, 2017). The authors applied a phononic crystal structure in the roof of a car to suppress low frequencies noise. Their periodic structure can be tuned to suppress sound in a range between 67 - 200 Hz. In Figure 1.5 it is depicted the unit cell of the phononic crystal, the location where the phononic crystal was installed and the reduction in vibration

transmission achieved:

Figure 1.5 – a) Unit cell of the phononic crystal, b) Phononic crystals installed in the car roof, c) Vibration transmission with and without phononic crystal in the roof.

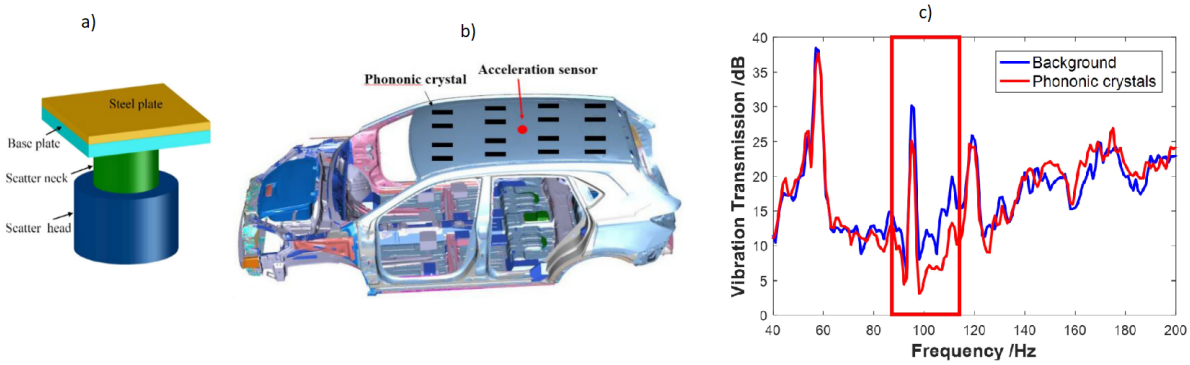

Source: (WAN; SHAO; CHENG, 2017).

The stability of an oil platform is essential for well drilling and structure reliability. Asiri and AL-Zahrani (2014) studied the application of material and geometry periodicity in offshore platform legs to attenuate vibrations caused by sea wave motion. It was found that the design of a periodic leg was capable of reducing the propagation of elastic waves throughout the platform in a broad range of frequencies (0-3000 Hz).

In any mechanical system there is loss of kinetic and potential energy. The phenomenon in which vibration amplitude diminishes over time is called damping.

Sources of damping can be divided in inherent or added damping. The former deals with damping due to structural joints, material microcracks, damping due to a surround fluid (air, water), whereas the latter deals with some kind of energy dissipation mechanism that is added to structure in order to reduce vibration or sound transmission. In this case, special alloys or composite materials might be added to the structure, as well as viscoelastic materials or vibration absorbers.

Several damping models are available in literature, and their implementation relies on the type of energy dissipation mechanisms in the structure. However, from a practical perspective, it is rather difficult to find all the types of energy loss in a mechanical system, and often the analyst employs a simplification of these models to account for all sources of damping presented in the structure.

The viscous damping model is the most employed model for the analysis of damping in structures due to its mathematical simplicity, especially for mechanical systems modeled with just one single degree-of-freedom. This damping model is commonly applied in structures with shock absorbers or immerse in fluids, and the damping force is proportional to the velocity.

Another commonly employed damping model is the hysteretic damping model, usu-

ally utilized to model damping due to structural joints or material damping. In this particular damping model, the damping force is independent of structural frequency excitation, and there is a constant relation between the damping ratio and loss factor at the resonant peaks in the frequency domain of the structure.

In structures with viscoelastic materials added to suppress vibration, such as rubber mounts or constrained layer damping treatment, several mathematical models are used to characterize the behavior of these viscoelastic materials for damping, such as Kelvin-Voigt, Maxwell, Golla-Hughes-McTavish (GHM) and Generalized Maxwell Model (GMM). Viscoelastic materials possess a frequency-temperature dependency on its material properties, making it a challenge during the mathematical modeling development.

Since periodic structures are mechanical systems, they are also subjected to damping phenomenon. Therefore, any kind of energy dissipating mechanism should be included in the analysis of elastic wave propagation in periodic structures, as it could affect the formation of pass bands and band gaps.

Farzbod (2010) proposed a general framework for applying a Bloch analysis in damped systems to investigate the damping effect on dispersion curves. The results reveal that damping may introduce wavenumber band gaps and bending of dispersion curves. In this case, dispersion curves and wavenumbers may have two or more temporal frequencies.

Chen *et al.* (2016) introduced viscous dampers in a chain of metamaterials to investigate the dissipative effects on pass bands and band gaps. It was shown that a band gap merging phenomenon occurs when increasing the level of damping attenuation of the viscous dampers, as observed in Figure 1.6:

Figure 1.6 – a) Metamaterial with viscous dampers, b) Attenuation diagram of metamaterial, damping level represented by τ.

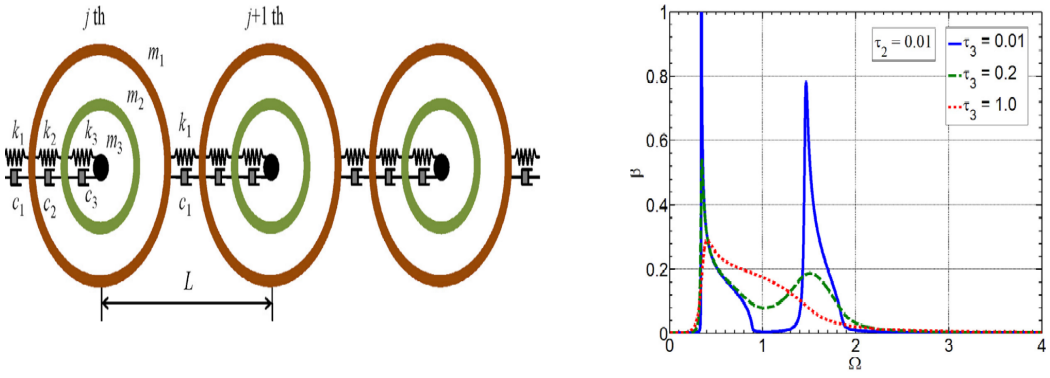

Source: (CHEN *et al.*, 2016).

For viscoelastic damping, Zhao and Wei (2009) analyzed the damping effect on one dimensional periodic structure caused by the viscoelastic host material. It was found that the viscoelastic parameters of the host material change the location and width of band gaps.

Regarding exotic types of damped periodic structures, Zheng, Li and Baz (2011) developed a periodic mount composed of viscoelastic cores, as depicted in Figure 1.7:

Figure 1.7 – Periodic mount using viscoelastic core.

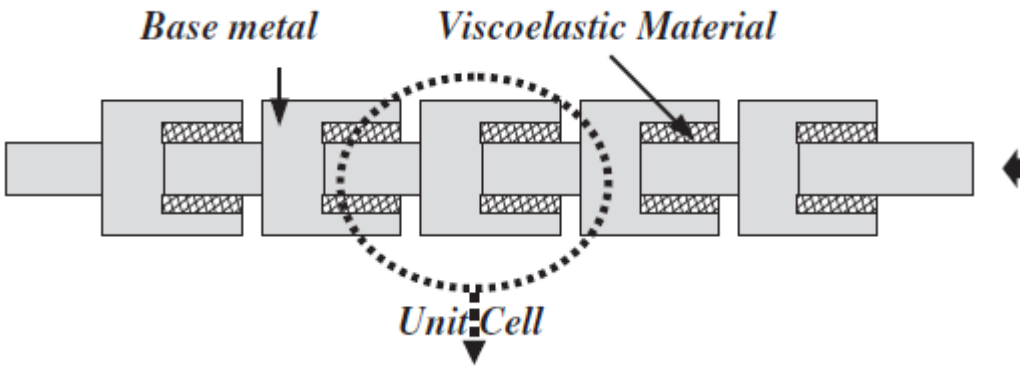

Source: (ZHENG; LI; BAZ, 2011).

The base metal was made of aluminum, while the viscoelastic material was made of rubber. The proposed design covered a wide frequency band gap region (0-14kHz). The authors claimed that their proposed periodic mount may find many applications where vibration must be attenuated, such as in gear support struts, engine mounts in automobiles and aircrafts, as well as in underwater vehicles.

Hussein and Frazier (2010) presented a theoretical formalism for the study of wave dispersion in damped elastic periodic materials, considering Rayleigh and general damping. Their results show that damping may radically change the frequency band structure, hence altering band gaps. Also, using general damping with the framework of free waves propagation, a wavenumber band gap also occurred.

Frazier (2015) studied the effect of energy dissipation (thus damping) in 1D phononic crystals and metamaterials. Using the framework of prescribed waves, it was found that material damping attenuates the transmission of energy between adjacent unit cells, resulting in spatial attenuation across the structure.

A hybrid phononic crystal with hysteretic damping was studied in Guo *et al.* (2018). It was investigated the effect of hysteretic damping in band gaps and power flow of the periodic structure, where it was found that hysteretic damping contributed to decrease the attenuation level of band gaps when increasing damping.

Belle (2019) investigated the effect of damping in band gaps for vibro-acoustic performance of locally resonant metamaterials on vibration and acoustic insulation. It was found that adding damping effectively reduced the peak attenuation of the structure, and that it was also possible to broaden the frequency range of attenuation. The impact on the acoustic insulation performance was only limitedly addressed.

Wang *et al.* (2020) studied the impact of particle damping on band gaps of phononic crystals. By filling the aluminum shell dampers with steel balls in an aluminum plate, it was found that the phononic crystal presented excellent medium and low frequencies damping characteristics, extremely wide-band gap and low frequency domain vibration damping characteristics.

Figure 1.8 – a) Particle damping phononic crystal structure, b) Periodic unit cell structure, c) Top view of periodic cell unit, d) Picture of the resonant structure with particle damping

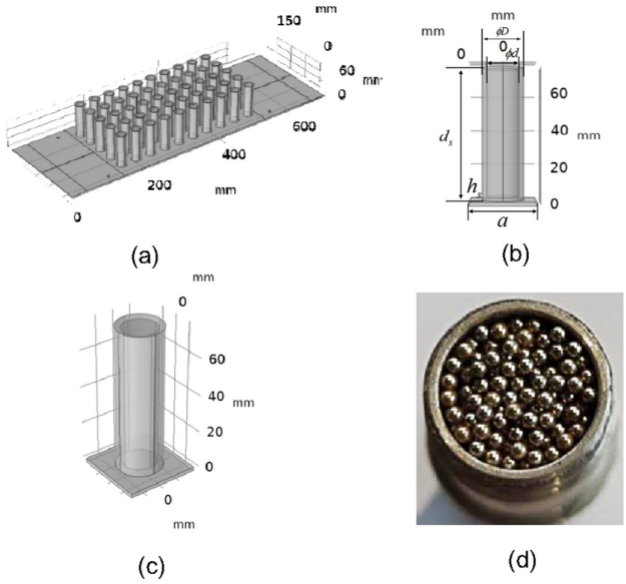

Source: (WANG *et al.*, 2020).

In order to analyze band gaps and pass bands in periodic structures, two frameworks are generally used, namely the free wave propagation and the prescribed wave. The former follows an approach $\omega = \omega(k)$, where ω denotes the frequency and k the wavenumber. In this case, the wavenumber is selected to be a real number, and the frequency solutions are permitted to be complex. This approach represents a medium permitting free dissipative wave motion as the result of an impulse loading for instance (KRATTIGER; PHANI; HUSSEIN, 2017).

On the other hand, the prescribed wave framework represents a periodic structure submitted to a harmonic sustained frequency, like a harmonic force. In this case, the formulation is given by $k = k(\omega)$, where the frequencies are selected to be real and the wavenumber solutions are permitted to be complex.

In Figure 1.9 it is shown the dispersion diagrams for both frameworks utilized to study the band gaps in periodic structures when damping is added:

Figure 1.9 – a) Dispersion diagram using free wave propagation, b) Dispersion diagram using prescribed wave propagation.

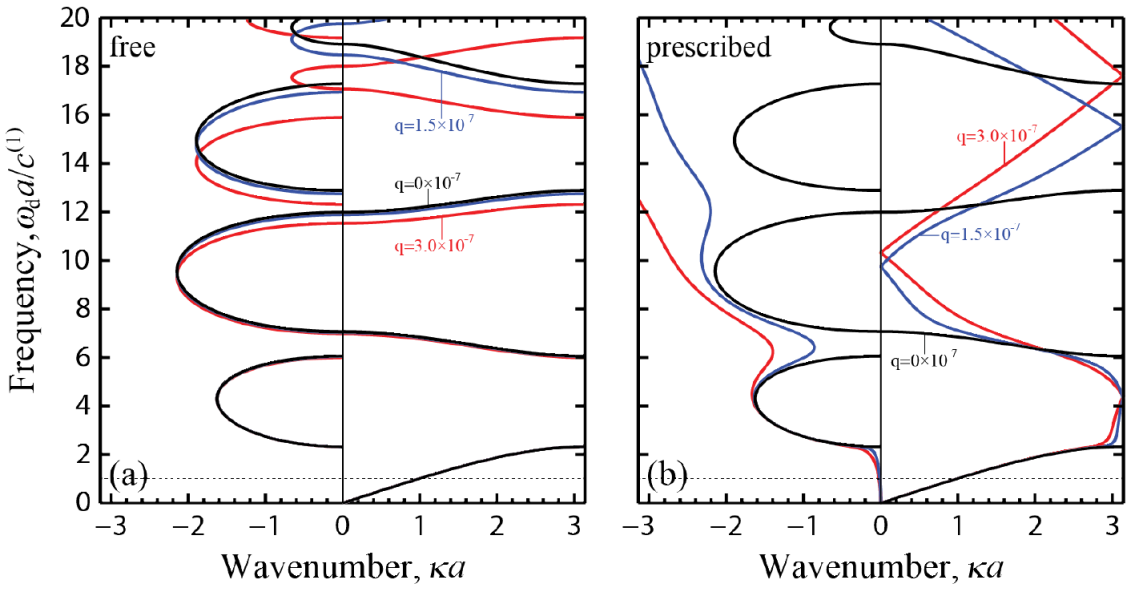

Source: (FRAZIER, 2015).

With no damping, represented by the expression $q = 0$, both frameworks describe the same pattern of pass bands and band gaps. However, as the damping increases, for instance $q = 1.5 \times 10^{-7}$, it can be seen totally different patterns in the band gaps. In the case of free wave propagation, the band gaps are shifted by a small amount, whereas in the case of the prescribed wave propagation it is seen that for frequencies above $\frac{\omega_d a}{c} = 5$, only band gaps exist.

1.1 Objectives

There is a vast literature regarding mechanical periodic structures. However, most of previous studies neglect energy dissipation effects. It is well known that real structures dissipate some amount of energy by various mechanisms such as friction at structural connections, internal friction, opening and closing of microcracks and so on. This energy dissipation might alter the behavior of wave propagation, impacting frequency band structures.

Considering the analysis of periodic structures, two frameworks are commonly used for the study of wave propagation: the free wave and prescribed wave propagation. The former is suited for the analysis of wave propagation when an initial displacement, velocity or impulse load is applied to the structure, whereas the latter is suited for the analysis of harmonically excited structures.

Nearly all studies focus on the effect of damping in periodic structures using the free wave propagation framework. Since many of the vibration problems in engineering are submitted to a harmonic force, the framework of prescribed waves will be utilized. Hence, this

dissertation is devoted to the study of several damping models in periodic structures using the framework of prescribed wave propagation and their impact on pass bands and band gaps of discrete and continuous periodic structures.

The damping models studied herein are the proportional and non-proportional viscous damping, the hysteretic damping and the viscoelastic damping. For the specific case of the viscoelastic damping, frequency and temperature effects on the viscoelastic material are considered.

1.2 Dissertation structure

In Chapter 2 it will be introduced the concept of band gaps and pass bands in mechanical periodic structures. Additionally, the transfer matrix method is described, as it will be useful to calculate the attenuation factor of the periodic structures. Furthermore, the band gaps and pass bands of a simple periodic beam are calculated using the transfer matrix method.

The different damping models are shown in Chapter 3. The models studied herein are the proportional viscous, non-proportional viscous, hysteretic and viscoelastic damping Each model is discussed in detail along with equations.

Chapter 4 presents the results of the different damping models and their impact on the attenuation factor of each structure: a mass-spring-damper system, a periodic composite rod and a periodic sandwich beam with viscoelastic cores.

Finally, in Chapter 5, conclusions regarding the dissertation herein are presented, as well as future perspectives. Moreover, the bibliography is also displayed.

Chapter 2

Methods for drawing dispersion curves

In this chapter two methods for drawing dispersion curves of periodic structures are illustrated, namely the transfer matrix method and the determinantal equation approach.

To understand wave propagation in periodic structures and therefore the calculation of band gaps, an example of a diatomic mass-spring-damper model is introduced. In Figure 2.1 the infinite diatomic mass-spring-damper chain is shown:

Figure 2.1 – a) Diatomic mass damper spring system, b) Unit cell of the system.

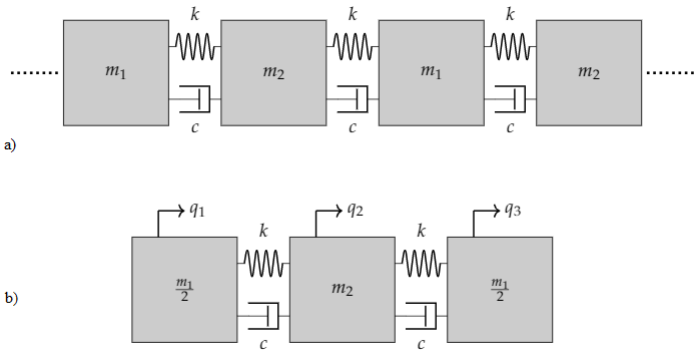

Source: The author.

The following equations are obtained after applying Newton's law of motion in the unit cell of Figure 2.1 b):

$$\begin{aligned} \frac{m_1}{2}\ddot{q}_1 + c(\dot{q}_1 - \dot{q}_2) + k(q_1 - q_2) &= f_1 \\ m_2\ddot{q}_2 + c(2\dot{q}_2 - \dot{q}_1 - \dot{q}_3 + k(2q_2 - q_1 - q_3) &= f_2 \\ \frac{m_1}{2}\ddot{q}_3 + c(\dot{q}_3 - \dot{q}_2) + k(q_3 - q_2) &= f_3 \end{aligned} \tag{2.1}$$

The variables q_1, q_2 and q_3 represent the displacement degrees of freedom with associated external forces f_1, f_2 and f_3.

The set of equations in Eq. (2.1) can be expressed in matrix form as follow:

$$\mathbf{M}=\begin{bmatrix}\frac{m_1}{2} & 0 & 0\\ 0 & m_2 & 0\\ 0 & 0 & \frac{m_1}{2}\end{bmatrix},\mathbf{C}=\begin{bmatrix}c & -c & 0\\ -c & 2c & -c\\ 0 & -c & c\end{bmatrix},\mathbf{K}=\begin{bmatrix}k & -k & 0\\ -k & 2k & -k\\ 0 & -k & k\end{bmatrix},\mathbf{q}=\begin{bmatrix}q_1\\ q_2\\ q_3\end{bmatrix},\mathbf{f}=\begin{bmatrix}f_1\\ f_2\\ f_3\end{bmatrix} \tag{2.2}$$

The matrix form development is extremely important when analyzing continuous systems such as bar and beams, as the numerical model such as the finite element method is required for the discretization of the unit cell.

With the matrix form, Newton's law of motion in the time domain is written as:

$$\mathbf{M}\ddot{\mathbf{q}}+\mathbf{C}\dot{\mathbf{q}}+\mathbf{K}\mathbf{q}=\mathbf{f} \tag{2.3}$$

However, using the assumption of harmonic motion, Eq. (2.3) is written in the frequency domain. Using Fourier transform in Eq. (2.3) and rearranging it:

$$(\mathbf{K}+j\omega\mathbf{C}-\omega^2\mathbf{M})\mathbf{q}=\mathbf{f} \tag{2.4}$$

The term inside the parentheses in Eq. (2.4) is called the dynamic stiffness matrix (DSM), and it is particularly useful in the analysis of wave propagation in structures:

$$\mathbf{D}=\mathbf{K}+j\omega\mathbf{C}-\omega^2\mathbf{M} \tag{2.5}$$

With the dynamic stiffness matrix obtained in Eq. (2.5), it is now possible to apply two methods to draw the dispersion curves, namely the transfer matrix method and the determinantal equation approach.

2.1 Transfer Matrix Method

The transfer matrix method was first conceived in the 1920s to analyze the vibration of one dimensional linear systems with an elastic construct (RUI; WANG; ZHANG, 2018). In the context of periodic structures, the transfer matrix method couples the forces and displacements between adjacent cells, and make it possible to calculate dispersion curves when applying Floquet-Bloch theorem.

Using the unit cell of Figure 2.1, it is convenient to partition it into left (L), inner (I) and right boundaries (R). In Figure 2.2 it is shown the partitioned adjacent unit cells (n) and (n+1):

Figure 2.2 – Diatomic mass damper spring system in a) and unit cell in b).

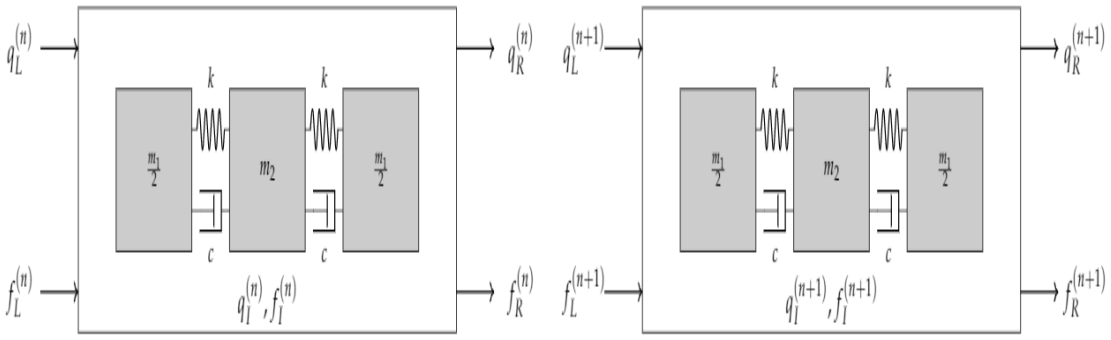

Source: The author.

Decomposing the dynamic stiffness matrix into left (L), right (R) and interior (I) degrees of freedom and by not applying external forces on the interior nodes, the following expression is obtained:

$$\begin{bmatrix} \overline{\mathbf{D}}_{\mathbf{LL}} & \overline{\mathbf{D}}_{\mathbf{LI}} & \overline{\mathbf{D}}_{\mathbf{LR}} \\ \overline{\mathbf{D}}_{\mathbf{IL}} & \overline{\mathbf{D}}_{\mathbf{II}} & \overline{\mathbf{D}}_{\mathbf{IR}} \\ \overline{\mathbf{D}}_{\mathbf{RL}} & \overline{\mathbf{D}}_{\mathbf{RI}} & \overline{\mathbf{D}}_{\mathbf{RR}} \end{bmatrix} \begin{bmatrix} \mathbf{q}_{\mathbf{L}} \\ \mathbf{q}_{\mathbf{I}} \\ \mathbf{q}_{\mathbf{R}} \end{bmatrix} = \begin{bmatrix} \mathbf{f}_{\mathbf{L}} \\ \mathbf{0} \\ \mathbf{f}_{\mathbf{R}} \end{bmatrix} \tag{2.6}$$

Since the interior degrees of freedom are not subject to any type of force/moment, the decomposed DSM is condensed on left and right boundaries only:

$$\begin{bmatrix} \mathbf{D}_{\mathbf{LL}} & \mathbf{D}_{\mathbf{LR}} \\ \mathbf{D}_{\mathbf{RL}} & \mathbf{D}_{\mathbf{RR}} \end{bmatrix} \begin{bmatrix} \mathbf{q}_{\mathbf{L}} \\ \mathbf{q}_{\mathbf{R}} \end{bmatrix} = \begin{bmatrix} \mathbf{f}_{\mathbf{L}} \\ \mathbf{f}_{\mathbf{R}} \end{bmatrix} \tag{2.7}$$

with $\mathbf{D_{xx}} = \overline{\mathbf{D}}_{\mathbf{xx}} - \overline{\mathbf{D}}_{\mathbf{xI}} \overline{\mathbf{D}}_{\mathbf{II}}^{-1} \overline{\mathbf{D}}_{\mathbf{Ix}}$, where the subscript **xx** denotes the degrees of freedom of left (L) or right (R) side boundaries.

Let **T** be a matrix that relates displacements and forces between two adjacent cells (n) and (n+1), it then follows:

$$\mathbf{T} \begin{bmatrix} \mathbf{q_L}^{(n)} \\ \mathbf{f_L}^{(n)} \end{bmatrix} = \begin{bmatrix} \mathbf{q_R}^{(n)} \\ -\mathbf{f_R}^{(n)} \end{bmatrix} = \begin{bmatrix} \mathbf{q}_{\mathbf{L}}^{(n+1)} \\ \mathbf{f}_{\mathbf{L}}^{(n+1)} \end{bmatrix} \tag{2.8}$$

Combining Eqs (2.7) and (2.8), the transfer matrix T is obtained:

$$\mathbf{T} = \begin{bmatrix} -\mathbf{D_{LR}}^{-1}\mathbf{D_{LL}} & \mathbf{D_{LR}}^{-1} \\ -\mathbf{D_{RL}} + \mathbf{D_{RR}}\mathbf{D_{LR}}^{-1}\mathbf{D_{LL}} & -\mathbf{D_{RR}}\mathbf{D_{LR}}^{-1} \end{bmatrix} \tag{2.9}$$

The displacements and forces at the left end of a unit cell are related to the displacements and forces of at the right end of the nth cell by multiplying the transfer matrix of each

unit cell in sucession.

$$\begin{bmatrix} \mathbf{q_R}^{(n)} \\ \mathbf{f_R}^{(n)} \end{bmatrix} = \mathbf{T}_n \mathbf{T}_{(n-1)} ... \mathbf{T}_1 \begin{bmatrix} \mathbf{q_L}^{(1)} \\ \mathbf{f_L}^{(1)} \end{bmatrix} = \mathbf{T} \begin{bmatrix} \mathbf{q_L}^{(1)} \\ \mathbf{f_L}^{(1)} \end{bmatrix} \tag{2.10}$$

The Floquet-Bloch theorem states that the time harmonic response at any point in an unit cell is the same of the corresponding point in an unit cell with a phase difference of e^{ika} (HUSSEIN; KHAJEHTOURIAN; ABEDINNASAB, 2014), where i is the complex number, k is the wavenumber and a is the length of the unit cell. Thus, for any structure with repetitive unit cells, one can use Floquet-Bloch theorem to understand wave propagation in the entire structure by only analyzing the wave motion within a single unit cell (PHANI; HUSSEIN, 2017). The Floquet-Bloch theorem is given by Eq. (2.11) :

$$f(x+a) = e^{ika} f(x) \tag{2.11}$$

One observation is that Floquet-Bloch theorem applies to infinite periodic structures, i.e. structures with no boundaries (DOMADIYA *et al.*, 2016). In practice, structures are finite in nature, thus presenting boundaries that reflects elastic waves. Moreover, the discontinuities in these periodic structures causes reflection, transmission and wave mode interchange. However, it has been demonstrated by many studies (SONTI; NARAYANA, 2006; YILMAZ; HULBERT, 2017; DOMADIYA *et al.*, 2016) that the location of band gaps in an infinite periodic structure matches with its finite counterpart. For instance, Belle (2019) studied the sound transmission loss between infinite and finite phononic crystals and locally resonant metamaterials, with results shown in Figure 2.3:

Figure 2.3 – a) Sound Transmission Loss for infinite and finite locally resonant metamaterials, b) Sound Transmission Loss for infinite and finite phononic crystals.

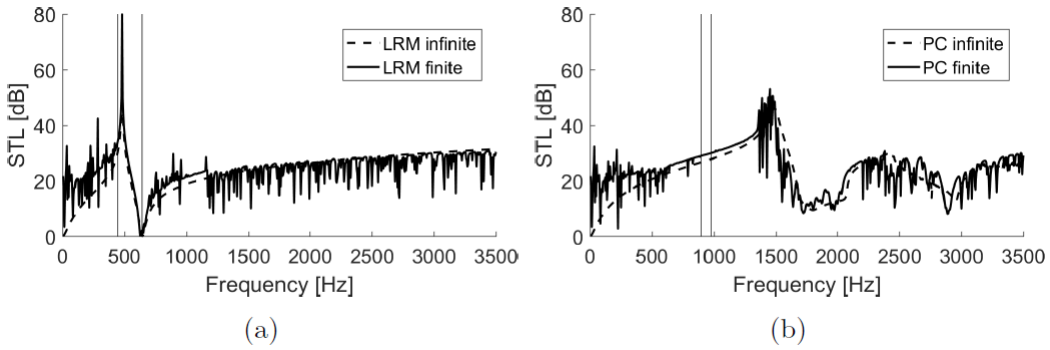

Source: (BELLE, 2019).

It can be seen in Figure 2.3 a good agreement between the finite and its infinite counterpart in terms of sound transmission loss, demonstrating that modeling a finite periodic

structure using its unit cell and applying Floquet-Bloch theorem is sufficient to get accurate results.

When applying Eq. (2.11) to the displacement and forces of the unit cell, the following relation is obtained:

$$\begin{bmatrix} \mathbf{q_R}^{(n)} \\ \mathbf{f_R}^{(n)} \end{bmatrix} = e^{ika} \begin{bmatrix} \mathbf{q_L}^{(1)} \\ \mathbf{f_L}^{(1)} \end{bmatrix} \tag{2.12}$$

From Eq. (2.10) and Eq. (2.12):

$$(\mathbf{T} - \lambda \mathbf{I}) \begin{bmatrix} \mathbf{q_L}^{(1)} \\ \mathbf{f_L}^{(1)} \end{bmatrix} = 0 \tag{2.13}$$

where λ are the eigenvalues of the $\mathbf{T}$ matrix, with $\lambda = e^{ika}$. In order to calculate stop bands and pass bands of periodic structures, the eigenvalues of the transfer matrix must be calculated. The physical meaning of the eigenvalues is given below:

- If $|\lambda| = 1$, a pass band condition is defined
- If $|\lambda| < 1$, a stop band condition is defined.

The eigenvalue λ can also be rewritten in terms of phase change and amplitude ratio as:

$$\lambda = e^{\mu} = e^{\alpha + j\beta} \tag{2.14}$$

Where μ is defined as the propagation constant, with the real part α representing the attenuation factor (logarithmic decay of the state vector) and β the phase difference between adjacent cells (BAZ, 2019).

Consequently, the stop and pass band conditions can be written in terms of α:

- If $\alpha = 0$, we obtain a pass band, as there is no amplitude attenuation.
- If $\alpha \neq 0$, we obtain a stop band, with an amplitude attenuation defined by the value of α.

Using the steps summarized in the above flowchart, the attenuation factor diagram of the diatomic mass spring damper is given in Figure 2.4:

Figure 2.4 – Attenuation factor diagram of diatomic mass spring damper system.

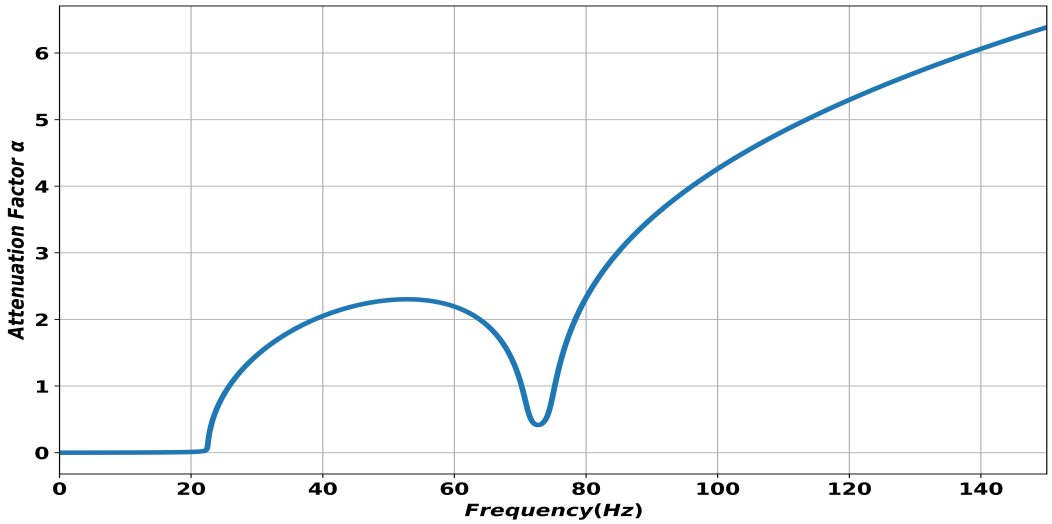

Source: The author.

It is observed in Figure 2.4 that between approximately 0-20 Hz the attenuation factor is zero, meaning that this is a pass band region, where elastic waves are free to propagate. Then the attenuation factor increases from 23-72 Hz, so this is considered a band gap region, where the elastic waves are attenuated. The presence of damping in the system attenuates the elastic waves in the region between 72-74 Hz. From 74-150 Hz the attenuation factor keeps increasing, meaning that the elastic waves are highly attenuated in this frequency range.

In Figure 2.5 it is depicted the phase constant diagram of the periodic structure:

Figure 2.5 – Attenuation factor diagram of diatomic mass spring damper system.

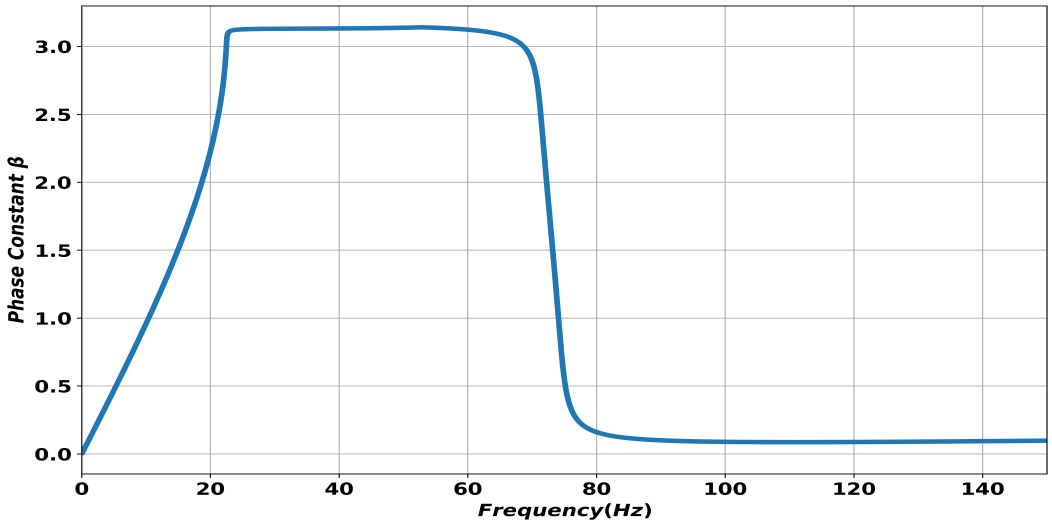

Source: The author.

The phase constant relates the phase difference between adjacent unit cells. For instance, a phase constant value of zero means that the adjacent unit cells are moving in phase,

whereas a phase constant value of π would mean that the adjacent unit cells are moving totally out of phase.

In Figure 2.6 it is shown the FRF of the diatomic mass spring damper system composed of ten unit cells:

Figure 2.6 – Frequency response of the diatomic mass spring damper system.

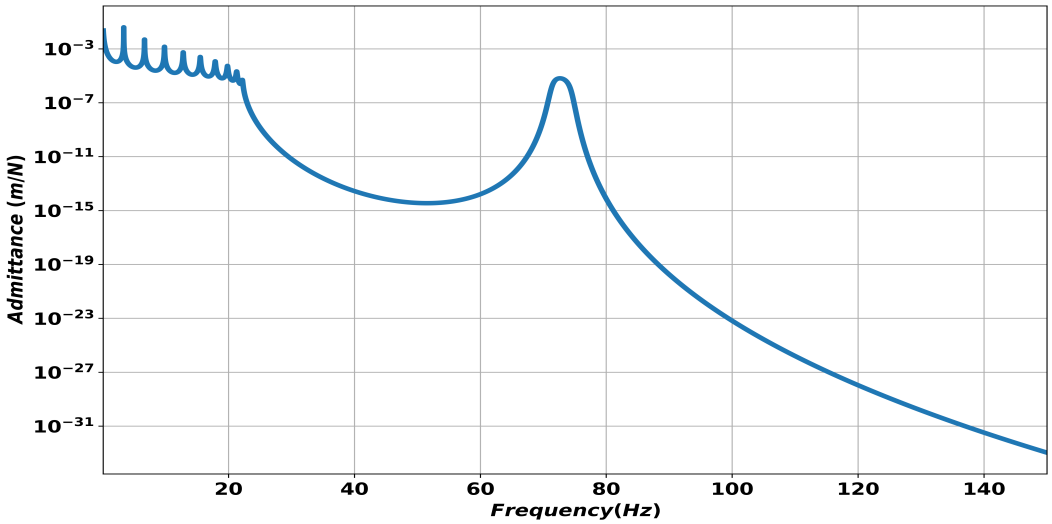

Source: The author.

Notice that inside the band gap zones located at 20 - 72 Hz and 74 - 150 Hz the displacement of the mass is greatly reduced. Hence, the engineer can design structures that block propagation of elastic waves at selectable frequencies.

2.2 Determinantal Equation Approach

The determinantal equation approach is another method utilized to calculate the dispersion curves. It consists on finding the complex roots of a determinant equation. These roots are in fact the propagation constant of the periodic structure. For instance, MEAD (1986) used this method to calculate the propagation constant μ in periodic Timoshenko beams and stiffened plates.

For the determinantal equation approach, similar steps are taken from the transfer matrix method. Starting with the decomposed dynamic stiffness matrix from Eq. (2.7), it is possible to write the displacement terms $\mathbf{q}$ and forces $\mathbf{f}$ using Floquet-Bloch theorem in Eq. (2.11) as follows:

$$\begin{aligned} \mathbf{q_R} &= \mathbf{q_L} e^{-ika} \\ \mathbf{f_R} &= -\mathbf{f_L} e^{-ika} \end{aligned} \tag{2.15}$$

Substituting the relations from Eq. (2.15) in Eq. (2.7) leads to following matrix equa-

tion in Eq. (2.16):

$$\begin{bmatrix} \mathbf{D_{LL}} & \mathbf{D_{LR}} \\ \mathbf{D_{RL}} & \mathbf{D_{RR}} \end{bmatrix} \begin{bmatrix} \mathbf{I} \\ \mathbf{I}e^{-ika} \end{bmatrix} [\mathbf{q_L}] = \begin{bmatrix} \mathbf{I} \\ -\mathbf{I}e^{-ika} \end{bmatrix} [\mathbf{f_L}] \tag{2.16}$$

Next the external excitation forces are set to zero. In this case, Eq. (2.16) is multiplied on both sides by $[\mathbf{I}e^{-ika} \quad \mathbf{I}]$:

$$\begin{bmatrix} \mathbf{I}e^{-ika} & \mathbf{I} \end{bmatrix} \begin{bmatrix} \mathbf{D_{LL}} & \mathbf{D_{LR}} \\ \mathbf{D_{RL}} & \mathbf{D_{RR}} \end{bmatrix} \begin{bmatrix} \mathbf{I} \\ \mathbf{I}e^{-ika} \end{bmatrix} [\mathbf{q_L}] = \begin{bmatrix} \mathbf{I}e^{-ika} & \mathbf{I} \end{bmatrix} \begin{bmatrix} \mathbf{I} \\ -\mathbf{I}e^{-ika} \end{bmatrix} [\mathbf{f_L}] \tag{2.17}$$

Eq. (2.17) results in a homogeneous matrix equation whose determinant leads to the propagation constants. Hence, from Eq. (2.17) the determinantal equation is given by Eq. (2.18):

$$\left| \mathbf{D_{RL}} + (\mathbf{D_{LL}} + \mathbf{D_{RR}})e^{-ika} + \mathbf{D_{LR}}e^{-2ika} \right| = 0 \tag{2.18}$$

The solution of the determinant of Eq. (2.18) leads to the propagation constant $\mu = ika = \alpha + j\beta$, where it was previously defined that the values of the attenuation constant α dictates the conditions of pass bands and stop bands to occur.

Both methods leads to the goal of drawing dispersion curves for periodic structures, however the transfer matrix method is used throughout the entire dissertation due to its ease of numerical implementation, although numerical instabilities can arise in the solution of the eigenvalue problem at higher frequencies (GOPALAKRISHNAN, 2016). Nonetheless, the determinantal equation approach can also be employed, for instance, in implementations using symbolic math packages.

Chapter 3

Damping Models

Damping is the ability of a mechanical system to convert part of the vibrational energy into another form (often heat or sound), thus reducing the vibration amplitude over time. The primary mechanisms of inherently damping in mechanical systems are classified in three categories: internal damping, structural damping and fluid damping (SILVA, 2007).

In order to further reduce the vibration of a mechanical systems, passive or active external dampers may be added to the system. The former dampens the system without requiring an active source of power, as opposed to the latter. Examples of passive dampers are shock absorbers used in economy cars and constrained layer damping used in bridges, whereas active dampers can be found in self-propelled sprayer booms (MELLOTT, 2019) and luxury cars.

Often, the sources of passive damping in a system are very difficult to identify. The various types of damping may be present at the same time, such as viscous, Coulomb, and hysteretic damping.

As discussed in the introduction, damping alters the wave propagation characteristic in a structure, hence modifying the dispersion curves and impacting the location and width of band gaps and pass bands.

In this dissertation, three damping models along with their impact on band gaps and pass bands are covered: viscous, hysteretic and viscoelastic damping. The next section will describe each model in detail.

3.1 Viscous Damping

Viscous damping is commonly found in structures presenting shock absorbers or immersed in fluids like gas, air, water, etc. The damping force is proportional to the velocity of the vibrating structure.

3.1.1 Viscous Damping in Single Degree-of-Freedom System

As stated in the previous section, the damping force is proportional to the velocity of the vibrating structure, being represented by the following expression:

$$F_{damping} = -c\dot{x} \tag{3.1}$$

For the Single Degree-of-Freedom (SDOF) mechanical system in Figure 3.1, the equation of motion obtained is given in Eq. (3.2):

Figure 3.1 – SDOF mechanical system.

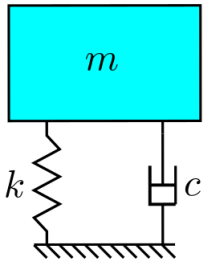

Source: The author.

$$m\ddot{x} + c\dot{x} + kx = 0 \tag{3.2}$$

To solve Eq. (3.2), the following solution is assumed:

$$x(t) = Ce^{yt} \tag{3.3}$$

Where C and y are constants. Substituting Eq. (3.3) in Eq. (3.2):

$$my^2 + cy + k = 0 \tag{3.4}$$

Hence, the two roots of Eq. (3.4) are:

$$y_{1,2} = -\frac{c}{2m} \pm \sqrt{\left(\frac{c}{2m}\right)^2 - \frac{k}{m}} \tag{3.5}$$

Using Eq. (3.5), the value of the damping coefficient c that makes the radical equals zero is called critical damping, and it is defined as:

$$c_c = 2\sqrt{km} = 2m\omega_n \tag{3.6}$$

The parameter that describes the oscillatory behavior of any damped system is called damping ratio, and it is obtained by the ratio of the damping coefficient to the system critical damping:

$$\zeta = \frac{c}{c_c} = \frac{c}{2m\omega_n} \tag{3.7}$$

Substituting Eq. (3.7) and (3.5) in Eq. (3.3), the general solution for the free SDOF system is:

$$x(t) = C_1 e^{\left(-\zeta+\sqrt{\zeta^2-1}\right)\omega_n t} + C_2 e^{\left(-\zeta-\sqrt{\zeta^2-1}\right)\omega_n t} \tag{3.8}$$

Where C_1 and C_2 are constants obtained by initial conditions.

The value of ζ defines how the system will oscillate over time. In this sense, the four cases are:

- $\zeta = 0$: Undamped system
- $0 < \zeta < 1$: Underdamped system
- $\zeta = 1$: Critically damped system
- $\zeta > 1$: Overdamped system

In the undamped case, the system vibrates without any decay in motion. For the underdamped system, the structure oscillates over time, with a frequency of vibration less than the undamped system. The critically damped system possesses no vibration, and the system returns to its equilibrium point in the shortest time. In the overdamped state, the system also does not vibrate, but it takes longer to return to the equilibrium point. In Figure 3.2 it is observed the free vibration response of the SDOF for the four damping ratio cases:

Figure 3.2 – Free vibration response for different damping ratio values

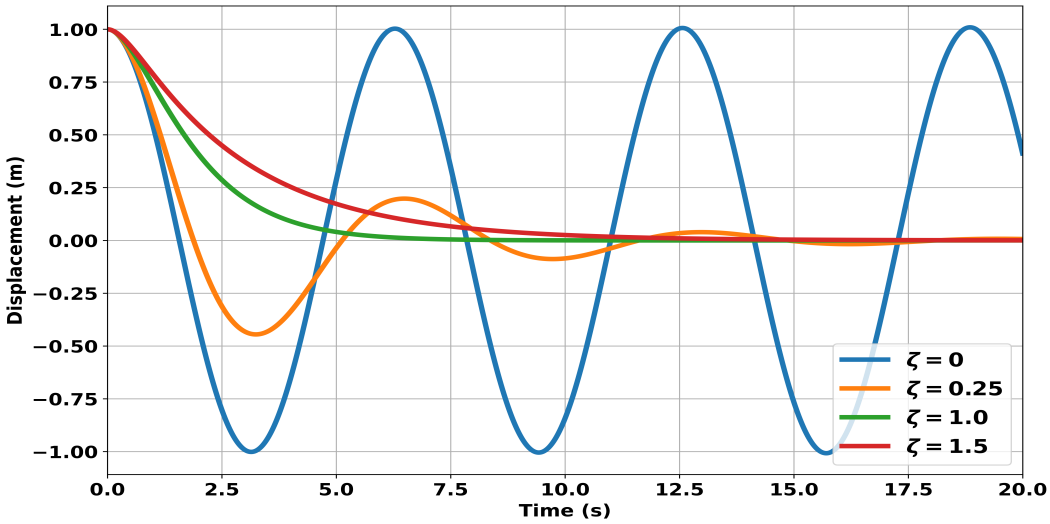

Source: The author.

For structures subjected to harmonic excitation, the SDOF equation of motion takes the following format:

$$m\ddot{x} + c\dot{x} + kx = f cos(\omega\ t) \tag{3.9}$$

It is useful to place Eq. (3.9) in the frequency domain, therefore:

$$-\omega^2 m + j\omega\ c + k = \frac{F}{X} \tag{3.10}$$

Rearranging Eq. (3.10) and making the substitution $\frac{c}{m} = 2\zeta\omega_n$, the frequency response function of the SDOF is obtained:

$$\left|\frac{X}{F}\right| = \left|\frac{1}{-\omega^2 + 2j\zeta\omega\omega_n + \omega_n^2}\right| \tag{3.11}$$

The effect of the damping ratio is observed in the FRF of the SDOF in Figure 3.3:

Figure 3.3 – Frequency response function of SDOF for various damping ratio levels

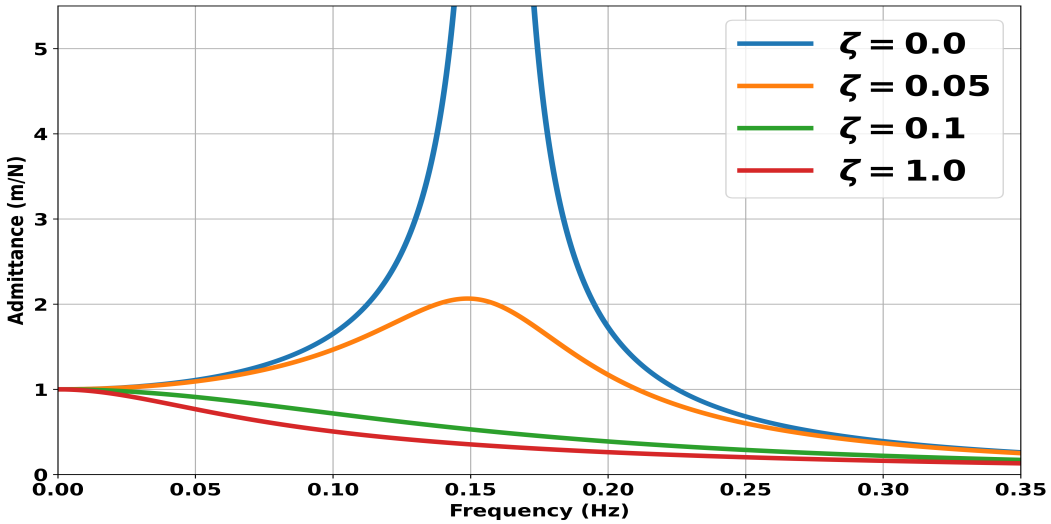

Source: The author.

From Figure 3.3 it is observed that the admittance level decreases as the damping ratio increases, with its effect specially pronounced at the natural frequency ω_n.

3.1.2 Viscous damping in Multiple Degree-of-Freedom

For a Multiple Degree-of-Freedom system (MDOF), the equation of motion of the vibrating structure with viscous damping is represented in Eq. (3.12) :

$$\mathbf{M}\ddot{\mathbf{x}} + \mathbf{C}\dot{\mathbf{x}} + \mathbf{K}\mathbf{x} = \mathbf{F}(t) \tag{3.12}$$

The damping matrix $\mathbf{C}$ in the viscous damping model falls into two categories: proportional and non-proportional damping, although the obtention of damping ratios is not trivial in the latter case.

In order to properly address the characteristics of the damping matrix, it is useful to place Eq. (3.12) in modal coordinates, where the set of coupled differential equations are transformed into a set of independent equations. In this case, the modal matrix ϕ is obtained such as the following relations in Eq. (3.13) are true:

$$\begin{aligned} \boldsymbol{\phi}^T \mathbf{M} \boldsymbol{\phi} &= \mathbf{I} \\ \boldsymbol{\phi}^T \mathbf{K} \boldsymbol{\phi} &= \boldsymbol{\Omega}^2 \end{aligned} \tag{3.13}$$

Where $\mathbf{I}$ is the identity matrix and Ω^2 the matrix of natural frequencies of the undamped structure. Using the modal coordinates transformation $q(t) = \phi z(t)$ and the relations in Eq. (3.13) in Eq. (3.12), the equations of motion in modal coordinates are shown in Eq. (3.14):

$$\mathbf{I}\ddot{\mathbf{z}} + \bar{\mathbf{C}}\dot{\mathbf{z}} + \Omega^2\mathbf{z} = \mathbf{F}\prime(t) \tag{3.14}$$

Where $\overline{\mathbf{C}} = \phi^{\mathbf{T}}\mathbf{C}\phi$ is the modal damping matrix and $\mathbf{F}'(t)$ the modal forcing function. The modal damping matrix $\overline{\mathbf{C}}$ will be useful to relate the damping constants of the structure with the damping ratios.

3.1.3 Proportional viscous damping

The proportional damping model assumes that the damping matrix $\mathbf{C}$ is a linear combination of the mass and stiffness matrix, represented by Eq. (3.15):

$$\mathbf{C} = \mu\,\mathbf{M} + \upsilon\,\mathbf{K} \tag{3.15}$$

In fact, the condition for proportional damping was obtained by Caughey and O'kelly (1964), where it can be demonstrated that in order for a damping matrix to be proportional, the following relation in Eq. (3.16) must be satisfied:

$$\mathbf{C}\mathbf{M}^{-1}\mathbf{K} = \mathbf{K}\mathbf{M}^{-1}\mathbf{C} \tag{3.16}$$

The approximation obtained in Eq. (3.15) is called Classical Rayleigh Damping, and it is widely used in structural damping modeling. The damping ratio obtained by μ and υ coefficients is shown in Eq. (3.17):

$$\zeta_i = \frac{1}{2}\left(\frac{\mu}{\omega_i} + \upsilon\omega_i\right) \tag{3.17}$$

From Eq. 3.17 it is noticed that the damping ratio related to the μ term is inversely proportional to the frequency, whereas the damping ratio related to the υ term increases linearly with the frequency. The plot shown in Figure 3.4 shows the contribution of each term separately and combined:

Figure 3.4 – Rayleigh Damping

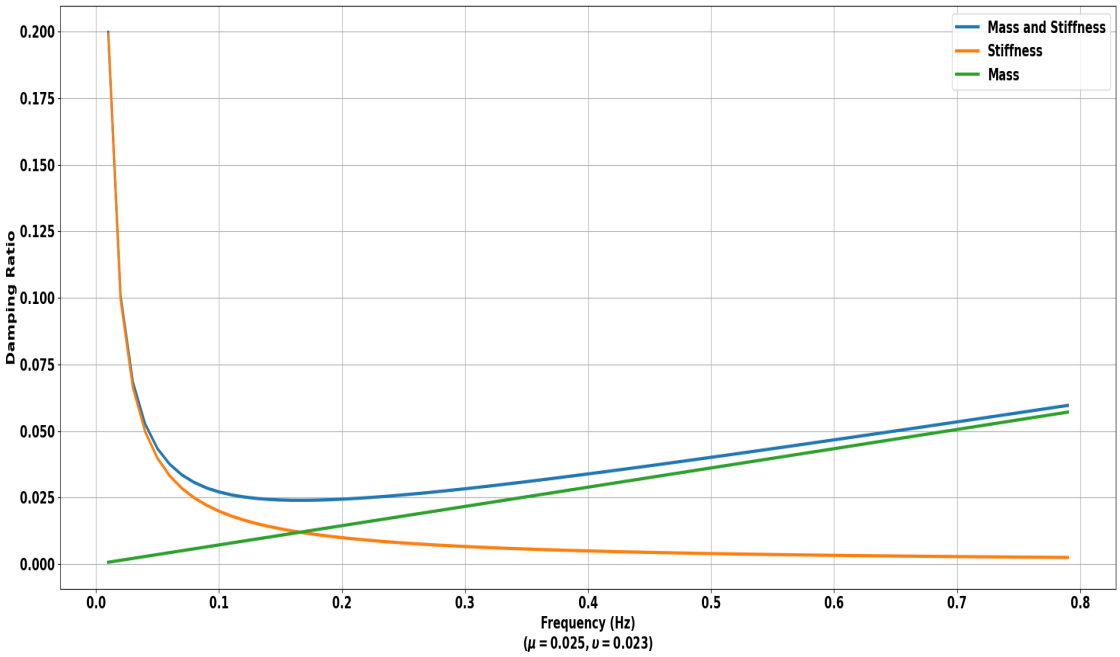

Source: The author.

3.1.4 Non proportinal viscous damping

When the damping matrix **C** does not satisfy the relation in Eq. (3.16) it is no longer considered proportional. In this case, the structure possesses complex modes and the damping ratios cannot be obtained by means of Eq. (3.17). However, using the assumption that the system is lightly damped ($\zeta_i < 0.3$)(LIANG; LEE, 1991), the off-diagonal terms of the modal damping matrix in Eq. (3.14) are neglected, and the damping ratios are obtained following Eq. (3.18):

$$\zeta_i = \frac{\bar{c}_{ii}}{2\omega_i} \tag{3.18}$$

Where $\overline{c_{ii}}$ are the diagonal elements of the modal damping matrix $\overline{\mathbf{C}}$ derived in Eq. (3.14).

3.2 Hysteretic damping

Hysteretic damping is characterized by material or structure inherent friction, leading to a damping phenomenon regardless of frequency excitation. The equation of motion for the SDOF with hysteretic damping shown in Figure 3.5 is given in Eq. (3.19):

Figure 3.5 – SDOF with hysteretic damping

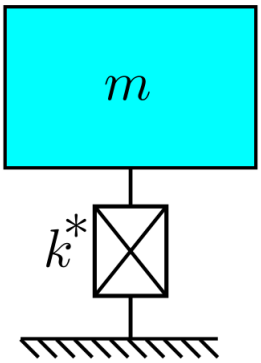

Source: The author.

$$m\ddot{x} + k^* x = F(t) \tag{3.19}$$

The stiffness in Eq. (3.19) is complex, with $k^* = k\left(1 + j\eta\right)$. The real part represents the static stiffness, whereas the imaginary part measures the hysteretic damping given by the loss factor η. Notice that the hysteretic damping is proportional to the displacement rather than velocity, as it is in the viscous damping model. It is also known that when the hysteretic damping is modeled as an equivalent viscous damping model (BEARDS; MIOA, 1996), the relation between the loss factor and the damping ratio at the local resonance is given in Eq. (3.20):

$$\zeta = \frac{\eta}{2} \tag{3.20}$$

By placing Eq. (3.19) in the frequency domain and rearranging it, the expression for the admittance is given in Eq. (3.21):

$$\left|\frac{X}{F}\right| = \left|\frac{1}{k(1 - \left(\frac{\omega}{\omega_n}\right)^2 + j\eta)}\right| \tag{3.21}$$

The effect of the loss factor in the FRF of the SDOF is shown in Figure 3.6:

Figure 3.6 – Frequency Response Function of SDOF for various loss factor values

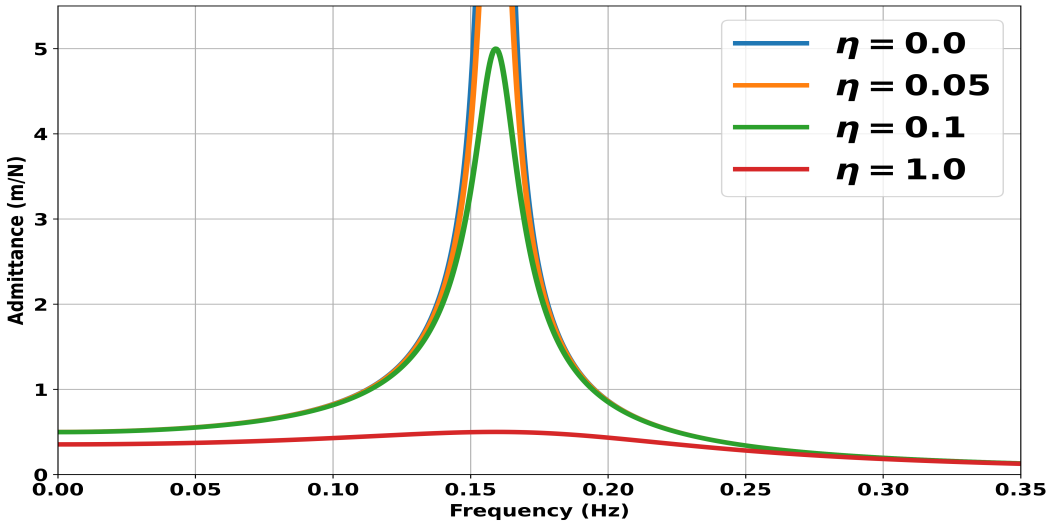

Source: The author.

It is noticeable in Figure 3.6 the attenuation of the admittance level in the resonant frequency caused by hysteretic damping. Therefore, inherent friction of structures is an important factor that contributes to decrease the overall vibration level.

Since in materials or structures the stiffness and damping are often coupled (BEARDS; MIOA, 1996), the elastic (and hence the shear) modulus is also represented by a complex number, shown in Eq. (3.22):

$$\begin{aligned} E^* &= E\left(1 + j\eta\right) \\ G^* &= G(1 + j\eta) \end{aligned} \tag{3.22}$$

Therefore, the equation of motion with hysteretic damping for MDOF system is give in Eq. (3.23):

$$\mathbf{M}\ddot{\mathbf{x}} + \mathbf{K}\left(1 + j\eta\right)\mathbf{x} = \mathbf{F}(t) \tag{3.23}$$

One key aspect of hysteretic damping is the frequency independent behavior. In this case, the damping ratios of resonant modes in the MDOF system have the same values, regardless of forcing frequency excitation.

3.3 Viscoelastic Damping

Viscoelastic materials (VEM) are capable of reducing vibration amplitude in structures. The process of deforming the viscoelastic material leads to the loss of part of the vibration energy due to viscous dissipation as heat (CHAKRABORTY; RATNA, 2020). Common

applications of viscoelastic materials are in engine cushions, computer hard drives and composite structures. In Figure 3.7 it is depicted a Fibre Reinforced Plastic Lightweight Structure internally damped with a special viscoelastic material made of flexible thermoset resin to damp frequencies between 50 - 2000 Hz. This structure is employed in the aerospace industry:

Figure 3.7 – Fibre Reinforced Plastic Lightweight Structure internally damped with VEM

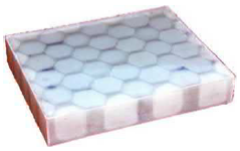

Source: (CHAKRABORTY; RATNA, 2020).

Viscoelastic materials possess a frequency and temperature dependent properties due to the relaxation time of the molecules or chain segments. Considering the effect of frequency and temperature, the viscoelastic material storage modulus E' and loss factor η are divided into three distinct regions: glassy, transition and rubbery.

In the glassy region, the VEM storage modulus possesses its highest storage modulus value and drops slightly when the temperature increases. As for the loss factor, its value increases with temperature. Moving to the transition region, the VEM becomes soft and drops its storage modulus value even further, whereas the loss factor achieves its maximum value. Finally, in the rubbery region, the VEM acts like a very soft material, with minimum storage modulus and loss factor value. These effects can be observed in Figure 3.8:

Figure 3.8 – Effect of temperature on storage modulus and loss factor of a viscoelastic material

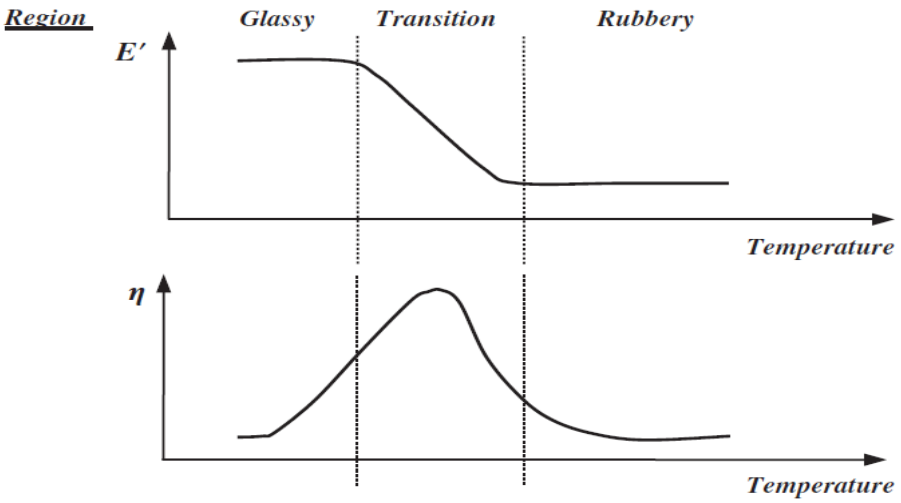

Source: (BAZ, 2019).

Moving to the frequency dependency, the viscoelastic behavior is the inverse of the temperature. In Figure 3.9 this effect is observed:

Figure 3.9 – Effect of operating frequency on storage modulus and loss factor of a viscoelastic material

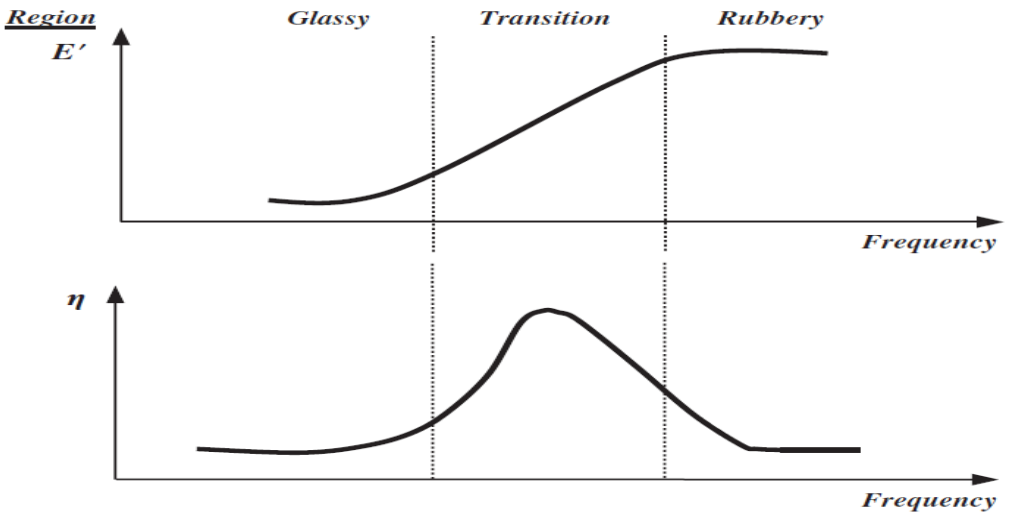

Source: (BAZ, 2019).

Classical viscoelastic material models are available in literature such as the Maxwell, Kelvin-Voigt and Poynting-Thomson models. However, due to their simplicity, they do not replicate the dynamic behavior of real VEMs. Currently, there are more powerful models capable of reproducing VEMs dynamic characteristics, for instance, the Fractional Derivative Model (FD) (BAHRAINI *et al.*, 2013), the Golla–Hughes–MacTavish (GHM) (FRISWELL; INMAN; LAM, 1997) and the Generalized Maxwell Model (GMM) (IDESMAN; NIEKAMP; STEIN, 2001) . A detailed description of the GMM is given, as it will be used over this dissertation.

3.4 Generalized Maxwell Model

The behavior of a VEM can be modelled by the so-called Generalized Maxwell Model (GMM). The GMM is currently used in various commercial finite element software, such as Abaqus®, ANSYS® and COMSOL Multiphysics®.

The viscoelastic material elastic or shear modulus following the GMM is represented in the frequency domain as:

$$E(s) = E_0(1 + \sum_{i=1}^{n} \frac{\alpha_i \rho_i s}{\rho_i s + 1}) \tag{3.24}$$

where E_0 is the equilibrium modulus, α_i the ith relative modulus and ρ_i the ith relaxation time.

An illustration of the GMM implemented in a single degree of freedom spring-mass system is given below. This method can be generalized to many degrees of freedom. The steps below can be found in Baz (2019).

Starting with the equation of motion in the Laplace domain:

$$\mathbf{M}s^2X(s)+\mathbf{K}(s)\mathbf{X}(s)=\mathbf{F}(s) \tag{3.25}$$

where $\mathbf{M}$ is the mass of the system, $\mathbf{K}$ is the stiffness of the VEM and $\mathbf{F}$ the force function. Introducing Eq. (3.24) in Eq. (3.25) gives:

$$\mathbf{M}s^2X(s)+\mathbf{K}\left(1+\frac{\alpha_n\rho_n s}{\rho_n s+1}\right)\mathbf{X}(s)=\mathbf{F}(s) \tag{3.26}$$

Let $\mathbf{Z}(s)$ be defined as an internal variable such that:

$$\mathbf{Z}=\frac{1/\rho_n}{s+1/\rho_n}\mathbf{X} \tag{3.27}$$

In the time domain, Eq. (3.27) takes the form below:

$$\dot{z}=\frac{1}{\rho_n}(x-z) \tag{3.28}$$

Substituting Eq. (3.27) in Eq. (3.26) gives:

$$\mathbf{M}s^2\mathbf{X}(s)+\mathbf{K}\mathbf{X}(s)+\mathbf{K}\alpha_n\rho_n s\mathbf{Z}(s)=\mathbf{F}(s) \tag{3.29}$$

Moving Eq. (3.29) to the time domain and substituting Eq. (3.28) gives:

$$\mathbf{M}\ddot{\mathbf{x}}+\mathbf{K}\mathbf{x}+\mathbf{K}\alpha_n(\mathbf{x}-\mathbf{z})=\mathbf{F}(t) \tag{3.30}$$

Eqs. (3.30) and (3.28) are combined in matrix form:

$$\begin{bmatrix}\mathbf{M}&0\\0&0\end{bmatrix}\begin{pmatrix}\ddot{\mathbf{x}}\\\ddot{\mathbf{z}}\end{pmatrix}+\begin{bmatrix}0&0\\0&1\end{bmatrix}\begin{pmatrix}\dot{\mathbf{x}}\\\dot{\mathbf{z}}\end{pmatrix}+\begin{bmatrix}\mathbf{K}(1+\alpha_n)&-\mathbf{K}\alpha_n\\-1/\rho_n&1/\rho_n\end{bmatrix}\begin{pmatrix}\mathbf{x}\\\mathbf{z}\end{pmatrix}=\begin{pmatrix}\mathbf{F}(t)\\0\end{pmatrix} \tag{3.31}$$

Multiplying the second row of Eq. (3.31) by $\mathbf{K}\alpha_n\rho_n$ gives us a new system with symmetric matrices:

$$\begin{bmatrix}\mathbf{M}&0\\0&0\end{bmatrix}\begin{pmatrix}\ddot{\mathbf{x}}\\\ddot{\mathbf{z}}\end{pmatrix}+\begin{bmatrix}0&0\\0&\mathbf{K}\alpha_n\rho_n\end{bmatrix}\begin{pmatrix}\dot{\mathbf{x}}\\\dot{\mathbf{z}}\end{pmatrix}+\begin{bmatrix}\mathbf{K}(1+\alpha_n)&-\mathbf{K}\alpha_n\\-\mathbf{K}\alpha_n&\mathbf{K}\alpha_n\end{bmatrix}\begin{pmatrix}x\\z\end{pmatrix}=\begin{pmatrix}\mathbf{F}(t)\\0\end{pmatrix} \tag{3.32}$$

The mass matrix of Eq. (3.32) is singular, hence the necessity of applying a static condensation method, such as Guyan reduction. After applying it, the internal variable **z** disappears, thus leaving:

$$\mathbf{M}\ddot{\mathbf{x}} + \mathbf{K}\alpha_n\rho_n\dot{\mathbf{x}} + \mathbf{K}\mathbf{x} = \mathbf{F}(t) \tag{3.33}$$

Observe that the system is damped by the terms **K**, α_n and ρ_n, which represents the VEM stiffness and parameters respectively. Thus, Eq. (3.33) is solved for **x** either via time or frequency domain.

Without loss of generality, the multi degree of freedom can be obtained the same way as for the single degree of freedom. Then:

$$\begin{bmatrix} \mathbf{M}_s+\mathbf{M}_v & 0 & 0 & \cdots & 0 \\ 0 & 0 & 0 & \cdots & 0 \\ 0 & 0 & 0 & \cdots & 0 \\ \cdots & \cdots & \cdots & \cdots & \cdots \\ 0 & 0 & 0 & \cdots & 0 \end{bmatrix} \begin{pmatrix} \ddot{\mathbf{x}} \\ \ddot{\mathbf{z}}_1 \\ \ddot{\mathbf{z}}_2 \\ \cdots \\ \ddot{\mathbf{z}}_n \end{pmatrix} + \begin{bmatrix} 0 & 0 & 0 & \cdots & 0 \\ 0 & \mathbf{K}_v\alpha_1\rho_1 & 0 & \cdots & 0 \\ 0 & 0 & \mathbf{K}_v\alpha_2\rho_2 & \cdots & 0 \\ \cdots & \cdots & \cdots & \cdots & \cdots \\ 0 & 0 & 0 & \cdots & \mathbf{K}_v\alpha_n\rho_n \end{bmatrix} \begin{pmatrix} \dot{\mathbf{x}} \\ \dot{\mathbf{z}}_1 \\ \dot{\mathbf{z}}_2 \\ \cdots \\ \dot{\mathbf{z}}_n \end{pmatrix} + \\ \begin{bmatrix} \mathbf{K}_s+\mathbf{K}_v(1+\alpha_1+\alpha_2+\ldots+\alpha_n) & -\mathbf{K}_v\alpha_1 & -\mathbf{K}_v\alpha_2 & \cdots & -\mathbf{K}_v\alpha_n \\ -\mathbf{K}_v\alpha_1 & \mathbf{K}_v\alpha_1 & 0 & \cdots & 0 \\ -\mathbf{K}_v\alpha_2 & 0 & \mathbf{K}_v\alpha_2 & \cdots & 0 \\ \cdots & \cdots & \cdots & \cdots & \cdots \\ -\mathbf{K}_v\alpha_n & 0 & 0 & \cdots & \mathbf{K}_v\alpha_n \end{bmatrix} \begin{pmatrix} \mathbf{x} \\ \mathbf{z_1} \\ \mathbf{z_2} \\ \cdots \\ \mathbf{z_n} \end{pmatrix} \tag{3.34}$$

where **M** and **K** are the global mass and stiffness matrix, and α_i and ρ_i the ith relative and relaxation modulus respectively.

One important variable that affects the properties of the VEM is the form factor, which depends on the material shape and size (KULIK; BOIKO, 2018). The form factor γ ranges from zero to one and it influences the value of the elasticity modulus of the material sample. In the work herein, two form factors will be used, one controlling the relative moduli nd the other the relaxation time. In this case, Eq. (3.24) is modified to account for the form factor terms, and thus Eq. (3.35) is obtained:

$$E(s) = E_0(1 + \sum_{i=1}^{n} \frac{\gamma_\alpha\alpha_i\gamma_\rho\rho_i s}{\gamma_\rho\rho_i s + 1}) \tag{3.35}$$

where γ_α is the form factor associated with the relative moduli coefficients and γ_ρ is the form factor associated with the relaxation time coefficients. In this work the form factors will be introduced to lower the natural damping of selected VEM so it can be possible to observe the influence of viscoelastic behavior on band gaps and pass bands. By not using the

provided factors, the damping provided by VEM places the periodic structure in an overdamped state, thus not being possible to observe the influence of viscoelasticity in the dispersion curves and FRFs.

Chapter 4

Results

In this chapter an investigation of dissipative effects in periodic structures will be presented. Such structures are going to be divided in two categories: discrete and continuous periodic structures. It is of fundamental importance to first study discrete systems, as those are used to gain an understanding of how the vibrating system behaves in a fundamental level, and how the damping will influence the characteristic of these systems in terms of FRF and dispersion diagrams. For instance, discrete systems are used in the modeling of the quarter car suspension to gain insights of the vibration response of the car. Dynamic vibration absorbers are also modeled as discrete systems in order to obtain an understanding of the vibration attenuation level of the structure where the absorber is inserted.

The conclusions obtained in discrete systems may also be applied to continuous systems, which in this case will be discretized by the finite element method, hence becoming in practice a discrete multi degree-of-freedom system.

The introduction of a discrete system with its equation of motion is made, followed by the calculation of pass bands and band gaps of the structure without damping. Thereafter, the effect of each damping model is analyzed individually in the structure by applying several damping ratio values, and their impact on pass bands and band gaps are discussed.

Finally, the same investigation is applied to the continuous systems. The structure is discretized via the finite element method and the equations of motion are obtained, followed by the FRF and dispersion curves. Next, it is implemented the damping models in these structures to observe the effect in band gaps and pass bands.

The effects of the proportional viscous damping (PVD), non-proportional viscous damping (NPVD), hysteretic damping (HD) and viscoelastic damping (VD) models in pass bands and band gaps are discussed for discrete and continuous mechanical systems. For the first discrete system studied, a thorough analysis is carried out showing the development of the non-proportional viscous damping model.

4.1 Lumped mass spring damper system

The investigation of damping effects on discrete systems is carried out in this section, represented by four different periodic structures configurations, two phononic crystals (PC) and two metamaterials (MM). For each model, the equations of motion are derived along with their matrix form, and the different damping models are applied, namely the non-proportional viscous, proportional viscous, hysteretic damping and viscoelastic damping. For the sake of simplicity, the damping ratio is only applied to the first vibrating mode of the unit cell under free-free boundary conditions for each configuration, and its effect over the frequency response function of the last cell and the dispersion diagram is observed along the periodic structure composed of ten unit cells. The mass, stiffness and damping ratio parameters are listed in Table 4.1:

Table 4.1 – Parameter values for mass, stiffness and damping ratio.

Parameter	Value	Unit
m_1, m_2, m_3	1, 10, 10	kg
k_1, k_2, k_3, k_4, k_r	100000	N/m
ζ_1	[0, 0.001, 0.01, 0.02]	dimensionless

Source: The author.

The viscoelastic material parameters represented by the storage modulus, relative moduli α_i and relaxation time ρ_i are shown in Table 4.2, for a reference temperature of 20 ^{o}C.

Table 4.2 – VEM material parameters at 20 ^{o}C.

Parameter	Value	Unit
K (storage modulus)	0.18	MN/m
α_i	[4.6 x 10^{-1}, 3.1 x 10^{-7}, 1.8 x 10^{-7}, 1 x 10^{-7}, 3.7 x 10^{-8}]	dimensionless
ρ_i	[3.1 x 10^{-1}, 2.1 x 10^{-7}, 1.2 x 10^{-7}, 7.1 x 10^{-8}, 2.6 x 10^{-8}]	seconds

Source: The author.

The increase in temperature shifts the storage modulus and loss factor curves. In this case, new values for the relative moduli and relaxation time are calculated to fit the new curves generated.

4.1.1 Case 1: Damped diatomic phononic crystal

The first case investigated is the damped diatomic phononic crystal. This phononic crystal is well known in the literature as it represents the most basic periodic structure that possess at least two band gap regions. In this case dampers will be added to the structure and the damping models are applied in order to gain insights on what effects each damping model may have in the location or width of band gaps and pass bands of this simple case.

The mechanical system with its unit cell is depicted in Figure 4.1:

Figure 4.1 – a) Damped diatomic phononic crystal and b) Unit cell of the respective system

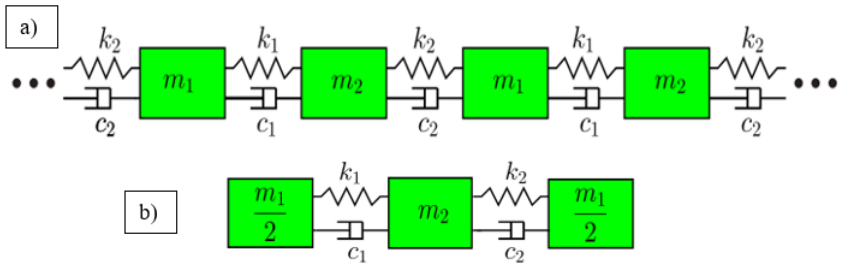

Source: The author.

The equation of motion for the unit cell of the damped diatomic phononic crystal is given in Eq (4.1):

$$\begin{gathered}\frac{m_1}{2}\ddot{q}_1 + c_1\left(\dot{q}_1 - \dot{q}_2\right) + k_1\left(q_1 - q_2\right) = f_1 \\ m_2\ddot{q}_2 + c_1\left(\dot{q}_2 - \dot{q}_1\right) + c_2\left(\dot{q}_2 - \dot{q}_3\right) + k_1\left(q_2 - q_1\right) + k_2\left(q_2 - q_3\right) = f_2 \\ \frac{m_1}{2}\ddot{q}_3 + c_2\left(\dot{q}_2 - \dot{q}_3\right) + k_2\left(q_2 - q_3\right) = f_3\end{gathered} \tag{4.1}$$

The mass, damping and stiffness matrix are derived from Eq. (4.1):

$$\mathbf{M} = \begin{bmatrix} \frac{m_1}{2} & 0 & 0 \\ 0 & m_2 & 0 \\ 0 & 0 & \frac{m_1}{2} \end{bmatrix}, \mathbf{C} = \begin{bmatrix} c_1 & -c_1 & 0 \\ -c_1 & c_1 + c_2 & -c_2 \\ 0 & -c_2 & c_2 \end{bmatrix}, \mathbf{K} = \begin{bmatrix} k_1 & -k_1 & 0 \\ -k_1 & k_1 + k_2 & -k_2 \\ 0 & -k_2 & k_2 \end{bmatrix} \tag{4.2}$$

The first analysis is conducted using non-proportional viscous damping (NPVD). With the values provided in Table 4.1, this condition requires that $\mathbf{K}\mathbf{M}^{-1}\mathbf{C} \neq \mathbf{C}\mathbf{M}^{-1}\mathbf{K}$, so careful must be taken when selecting damping coefficient values which satisfy the non-proportionality condition in Eq. (3.16).

In order to obtain the expression of the damping ratio, a numerical approach is followed. The values of mass and stiffness from Table 4.1 are substituted in Eq. (4.2):

$$\mathbf{M} = \begin{bmatrix} 0.5 & 0 & 0 \\ 0 & 10 & 0 \\ 0 & 0 & 0.5 \end{bmatrix}, \mathbf{K} = \begin{bmatrix} 100000 & -100000 & 0 \\ -100000 & 200000 & -100000 \\ 0 & -100000 & 100000 \end{bmatrix} \tag{4.3}$$

The eigenvalue problem to obtain the natural frequencies ω and eigenvectors ψ of the undamped unit cell under free-free boundary conditions is solved using Eq. (4.4):

$$\left(\mathbf{K} - \omega^2\mathbf{M}\right)[\boldsymbol{\psi}] = 0 \tag{4.4}$$

The values of the natural frequencies ω and the eigenvectors $\boldsymbol{\psi}$ of the unit cell after solving Eq. (4.4) via MATLAB® are given below in Eq. (4.5):

$$\omega = [0,\ 447,\ 469]\,, \quad \boldsymbol{\psi} = \begin{bmatrix} 0.577 & -0.707 & 0.705 \\ 0.577 & 0 & -0.070 \\ 0.577 & 0.707 & -0.705 \end{bmatrix} \tag{4.5}$$

The modal matrix $\boldsymbol{\phi}$ is obtained through the normalization of the mass matrix in Eq. (3.13). Hence, $\boldsymbol{\phi}$ is given by Eq. (4.6):

$$\boldsymbol{\phi} = \frac{\boldsymbol{\psi}}{\sqrt{\boldsymbol{\psi}^{\mathbf{T}}\boldsymbol{M}\boldsymbol{\psi}}} = \begin{bmatrix} 0.301 & -1 & 0.953 \\ 0.301 & 0 & -0.095 \\ 0.301 & 1 & 0.953 \end{bmatrix} \tag{4.6}$$

The modal damping matrix $\overline{\mathbf{C}}$ is then obtained via Eq. (3.14):

$$\overline{\mathbf{C}} = \boldsymbol{\phi}^{\mathbf{T}}\mathbf{C}\boldsymbol{\phi} = \begin{bmatrix} 0 & 0 & 0 \\ 0 & c_1 + c_2 & 1.05c_2 - 1.05c_1 \\ 0 & 1.05c_2 - 1.05c_1 & 1.1c_1 + 1.1c_2 \end{bmatrix} \tag{4.7}$$

Assuming light damping, the damping ratio expression of the unit cell for the first and second vibrating mode is obtained using Eq. (3.18):

$$\zeta_1 = \frac{\overline{c_{11}}}{2\omega_1} = \frac{c_1 + c_2}{894} \tag{4.8}$$

$$\zeta_2 = \frac{\overline{c_{22}}}{2\omega_2} = \frac{1.1(c_1 + c_2)}{938} \tag{4.9}$$

As it was stated earlier, care must be taken when selecting damping coefficient values to satisfy the non-proportionality condition. Herein, $c_1 = 0.1\ Ns/m$ and c_2 was calculated as a function of ζ_1, as it can be seen in Eq. (4.10). The damping ratio values were provided in Table 4.1.

$$c_2 = 894\zeta_1 - c_1 \tag{4.10}$$

The second analysis uses the proportional viscous damping (PVD) model. From Eq. (2.2), the damping matrix is proportional to the stiffness matrix, which requires that $\mathbf{C} = \upsilon\mathbf{K}$, where υ is the scalar proportional factor of the stiffness matrix from Eq. (3.15). For this case, the damping ratio is defined as in Eq. (3.17). Notice that due to the non-diagonal terms presented in the damping matrix it is not possible to obtain the scalar proportional factor

μ of the mass matrix, and this fact holds true throughout this dissertation for all the other periodic structures.

The third analysis applies the hysteretic damping (HD). In this situation the damping matrix is ignored, and the stiffness matrix becomes complex, as it was stated in Eq. (3.19) and Eq. (3.22). The damping ratio follows the formulation of equivalent viscous model, which takes place in Eq. (3.20). In this case, the loss factor η is chosen such that its value corresponds to the damping ratio values defined in Table 4.1.

Using the damping models listed above, the FRF of the unit cell for different damping models with different damping ratios are shown in Figure 4.2:

Figure 4.2 – FRF of unit cell of Case 1 for a) non viscous damping, b) viscous damping and c) hysteretic damping

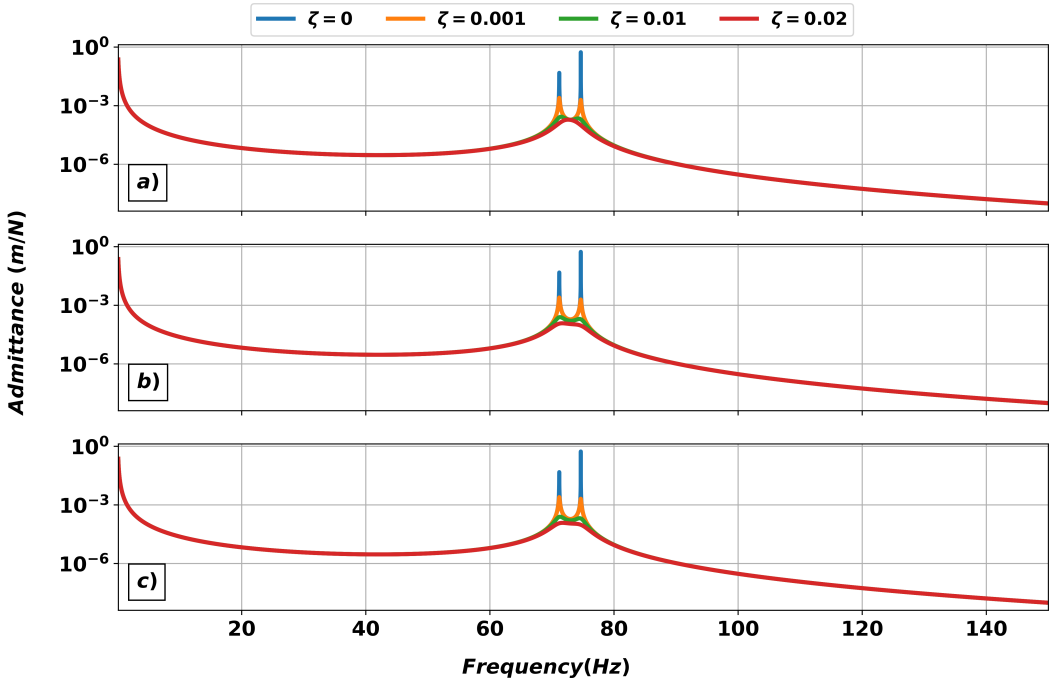

Source: The author.

It is noticeable in Figure 4.2 that as the damping ratio increases, the amplitudes of both resonances are attenuated until they merge into one single resonance. The FRF of the periodic structure composed of ten cells is shown in Figure 4.3:

Figure 4.3 – FRF of Case 1 composed of ten cells for a) non prop viscous damping, b) proportional viscous damping and c) hysteretic damping

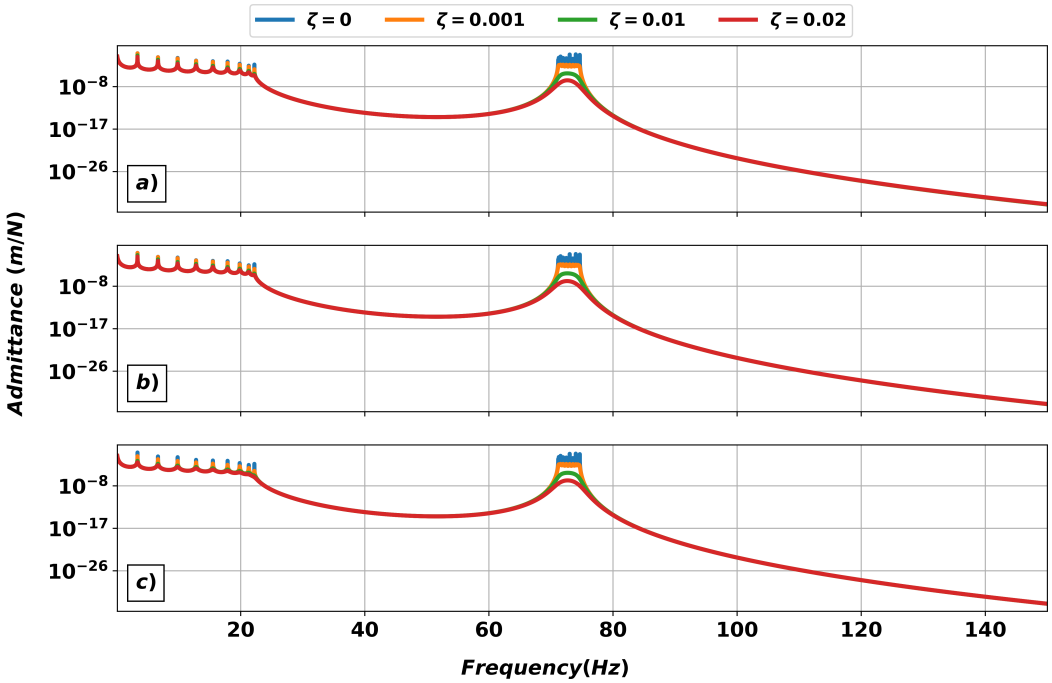

Source: The author.

The FRF in Figure 4.3 shows two band gaps regions located between 22-71 Hz and 74-150 Hz. As the damping ratio increases, the modes between the first and second band gap are more attenuated compared to the modes before the first band gap region. There are no apparent differences in width nor location of band gaps in the frequency range for the current damping models.

In Figure 4.4 it is depicted the dispersion diagrams of the damped diatomic PC for each damping model with several damping ratio values. The left side of Figure 4.4 shows the attenuation factor diagram and the right side shows the phase constant for different damping models with various damping ratios:

Figure 4.4 – Dispersion diagram of Case 1: a1) attenuation factor for NPVD, b1) attenuation factor for PVD, c1) attenuation factor for HD, a2) phase constant for NPVD, b2) phase constant for PVD, c1) phase constant for HD

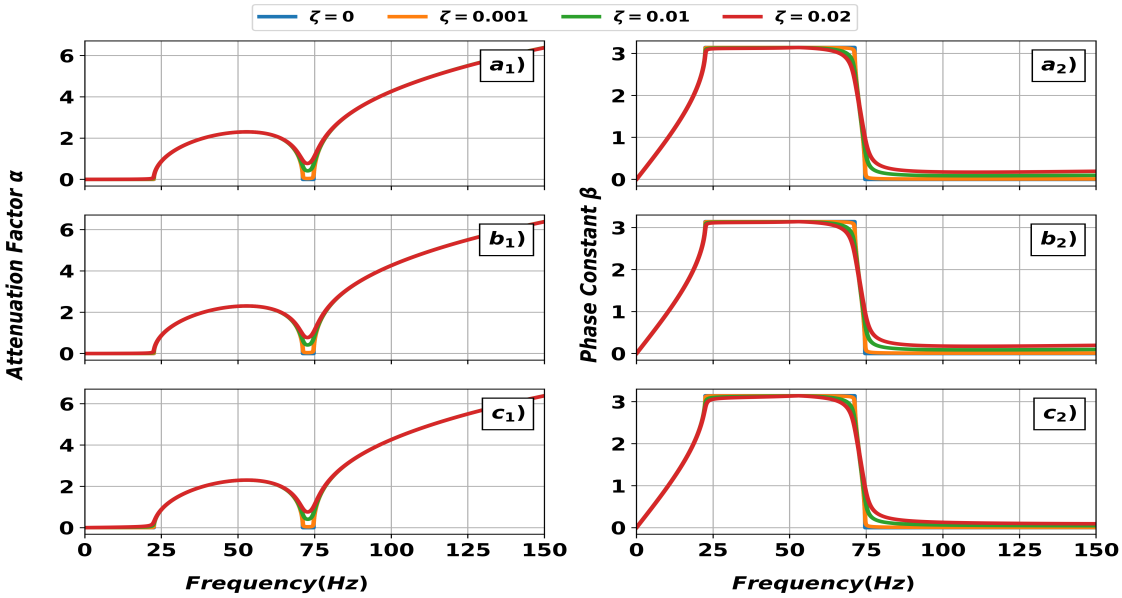

Source: The author.

The dispersion diagram in Figure 4.4 shows that there are no pass bands when damping is introduced in the structure when looking at the attenuation factor plot. Moreover, the values in the phase constant subplot do not reach the bounding values of the irreducible Brillouin zone (zero and π) when the damping ratio increases, meaning that the phase difference between adjacent unit cells are always between in or out-of phase. This attenuation is more pronounced in the transition from the first to the second band gap.

Now the viscoelastic damping model is applied to the first case. Following Eq. (3.24), the parameters that describe the VEM properties were listed in Table 4.2.

The form factors herein vary accordingly to obtain the desired damping ratio in the first vibrating mode of the unit cell. In Figure 4.5 it is shown the master curves for different levels of damping ratio at a temperature of 20 ^{o}C after applying different form factor values:

Figure 4.5 – Master Curve of viscoelastic material at a temperature of 20 ^{o}C for various damping ratios

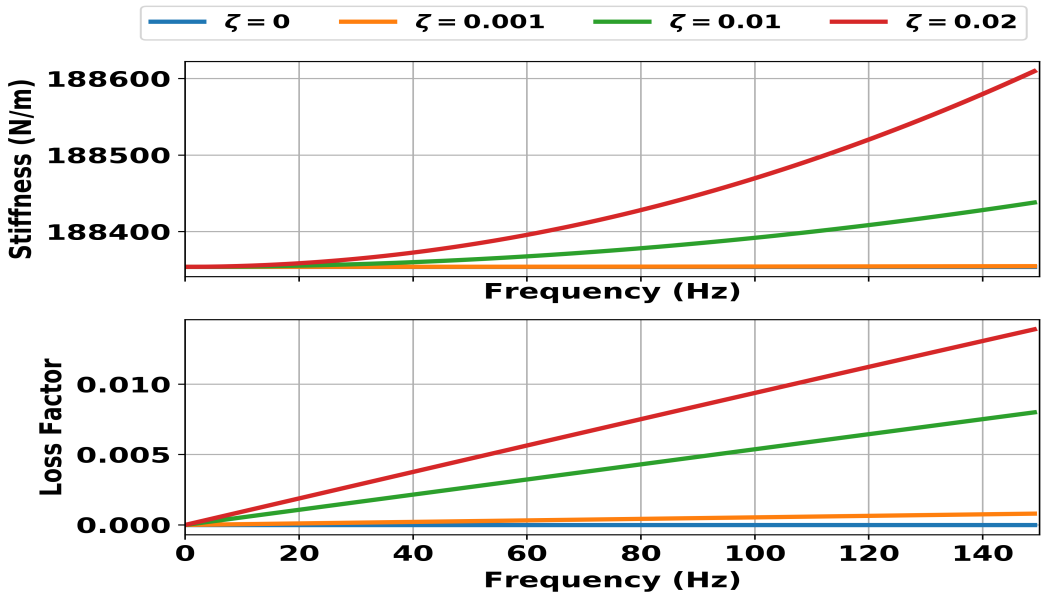

Source: The author.

It is observed in Figure 4.6 the FRF for different levels of damping ratio for three types of damping models, namely the proportional viscous damping, the hysteretic damping and the viscoelastic damping:

Figure 4.6 – FRF of Case 1 composed of ten cells for a) proportional viscous damping, b) hysteretic damping and c) viscoelastic damping model

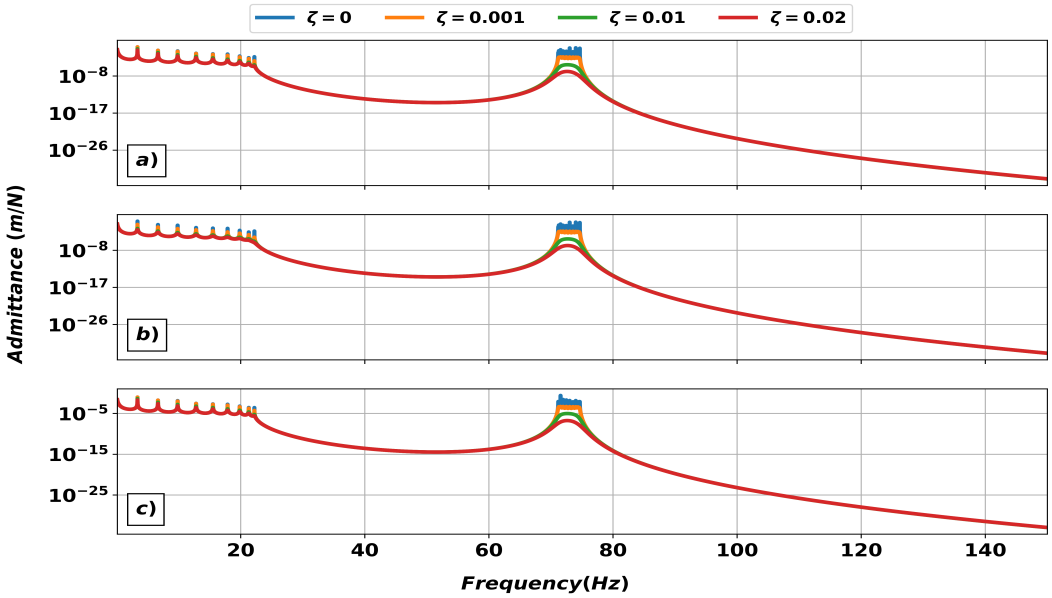

Source: The author.

Observing Figure 4.6, it is barely noticeable the difference between the viscoelastic model applied in this case compared to the other damping models. The admittance level in

the FRF decreases as the damping ratio increases in the pass band regions and the band gaps are not affected whatsoever.

In Figure 4.7 it is plotted the dispersion diagram for the three types of damping models:

Figure 4.7 – Dispersion diagram of Case 1: a1) attenuation factor for PVD, b1) attenuation factor for HD, c1) attenuation factor for VD, a2) phase constant for PVD, b2) phase constant for HD, c1) phase constant for VD

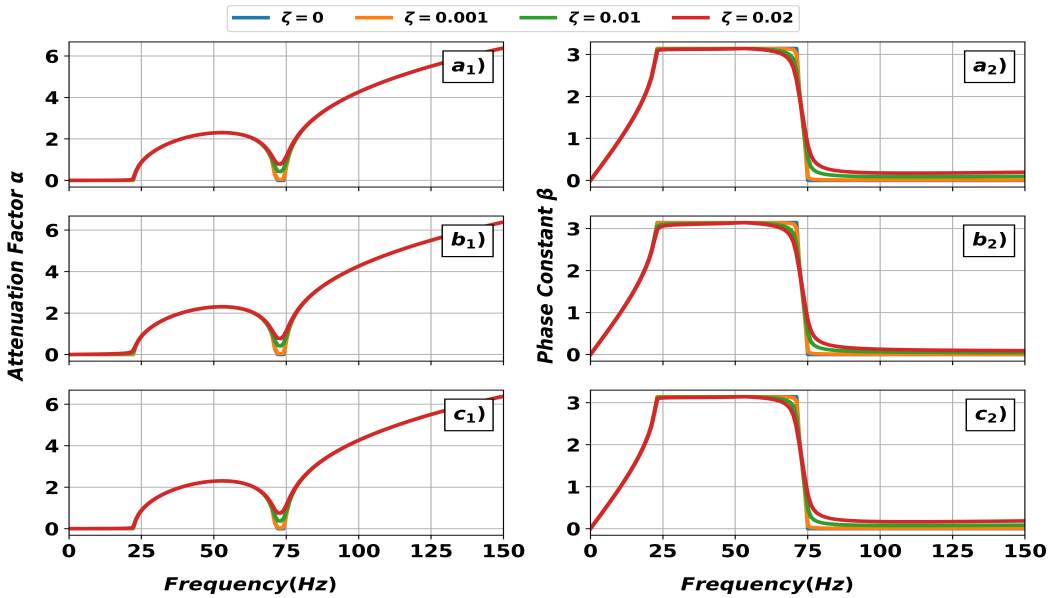

Source: The author.

From Figure 4.7 the same conclusions are drawn when compared to other damping models. The pass bands are eliminated and the bounding values of the phase constant are no more reachable.

The effect of temperature in the VEM is studied herein. The form factor is obtained such as to keep the damping ratio $\zeta = 0.02$. The master curves of the VEM under the influence of temperature variation are depicted in Figure 4.8:

Figure 4.8 – Master curve of the material used in the viscoelastic damping model

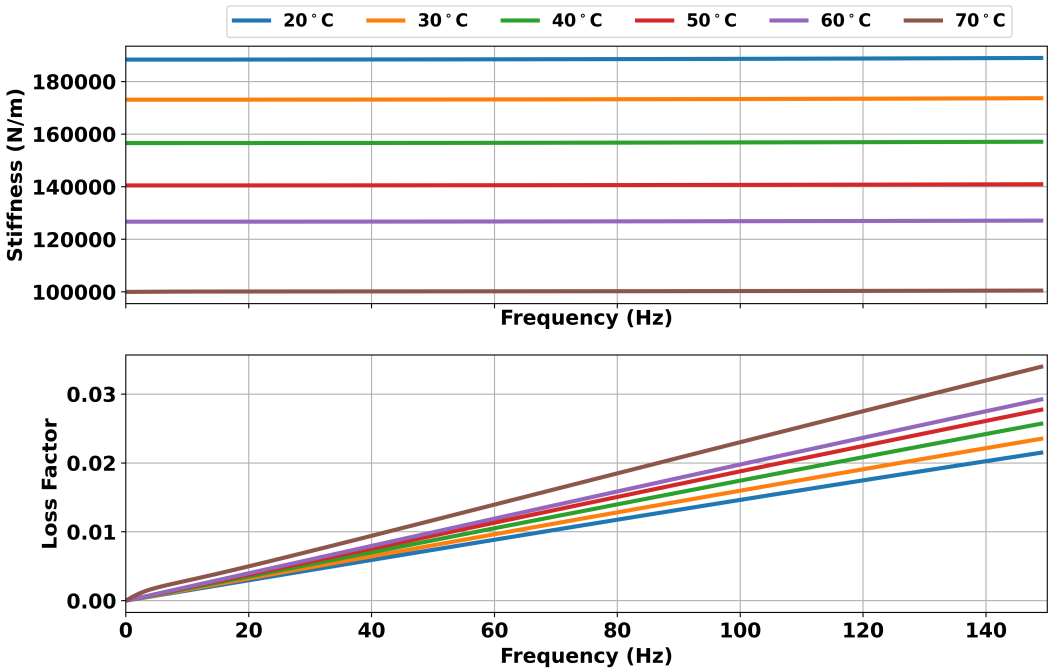

Source: The author.

As seen in Figure 4.8, this VEM is characterized in the transition zone, as depicted in Figure 3.8. As the temperature increases, the material softens and the loss factor achieves its peak value before dropping with higher temperatures. Due to the selected form factor value, the stiffness values do not increase within this frequency range of 0-150 Hz.

The temperature effect in the viscoelastic model in the FRF of the periodic structure is observed in Figure 4.9:

Figure 4.9 – FRF of Case 1 composed of ten cells for viscoelastic damping model with temperature effect

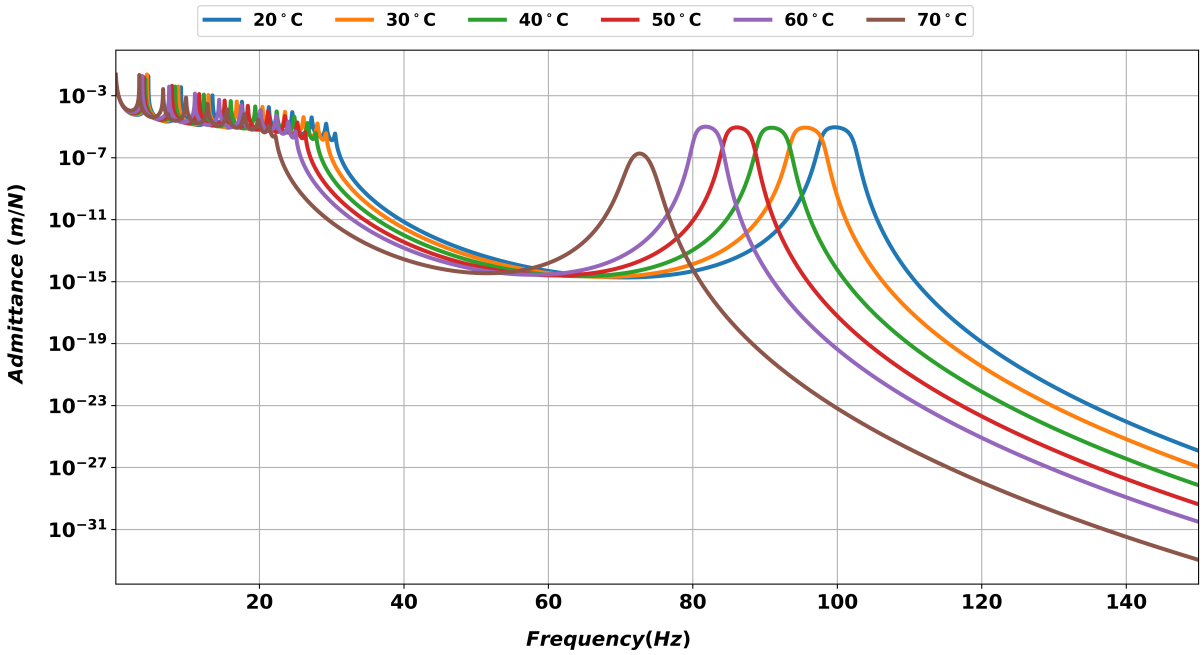

Source: The author.

It is observed in Figure 4.9 that the band gaps are shifted due to changes in stiffness, as already demonstrated in the master curves of Figure 4.8. Moreover, it is also observed that the damping ratio increases with frequency and temperature. Clearly, the resonant peak at 75 Hz for the temperature of 70 ^{o}C is more attenuated compared to its counterparts at different temperatures due to a higher loss factor, as depicted in Figure 4.8.

The dispersion diagram in Figure 4.10 corroborates the observations of the FRF. In this case, it is observed that the attenuation factor and phase constant values were shifted towards lower frequencies when the temperature increases.

Figure 4.10 – Dispersion diagram of Case 1 composed of ten cells for viscoelastic damping model with temperature effect

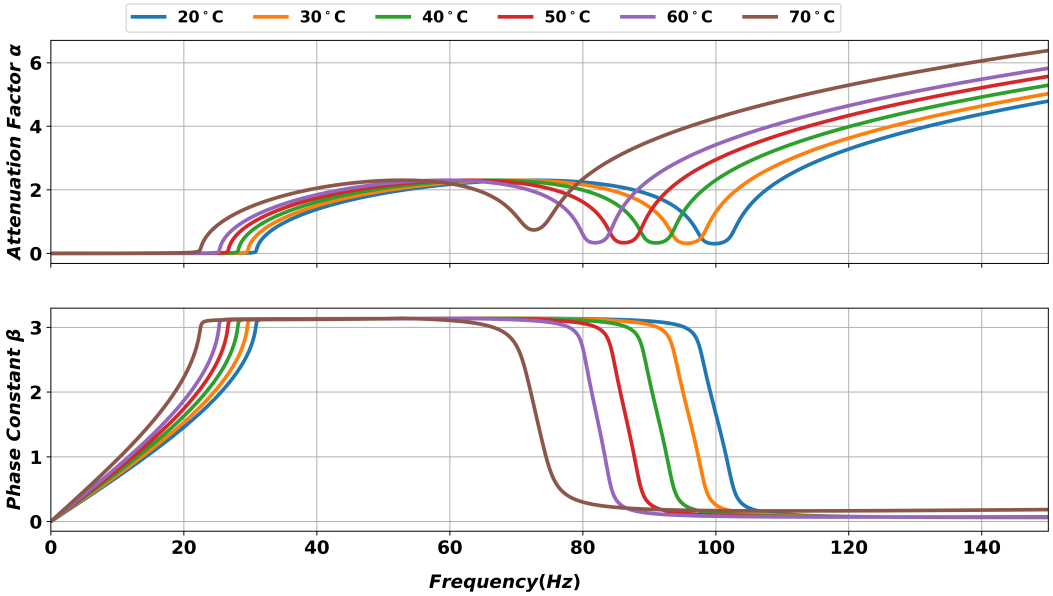

Source: The author.

Following all the results of applying different damping models to Case 1, it could be seen that the band gaps do not change their width or location when applying different damping models with varying damping ratio. However, the pass bands get attenuated regardless of the damping model applied. The type of damping model applied did not influence the attenuation level in the pass bands region.

When applying the viscoelastic damping model with temperature-frequency effect it could be observed the shift in band gaps and pass bands when increasing the temperature. As it was commented earlier, this behavior happens due to the shift in stiffness values with frequency and temperature, hence modifying the location and also the attenuation in the band gaps.

4.1.2 Case 2: Damped diatomic phononic crystal with grounded masses

The second case investigated is a damped diatomic phononic crystal with grounded masses, representing, for instance, a periodic structure with periodic foundations. The goal of using this topology is to observe how the masses attached to grounded springs and dampers will contribute in the band gaps and pass bands in terms of attenuation. The topology of the system and its unit cell is depicted in Figure 4.11:

Figure 4.11 – a) Periodic structure of Case 2 and b) Unit cell

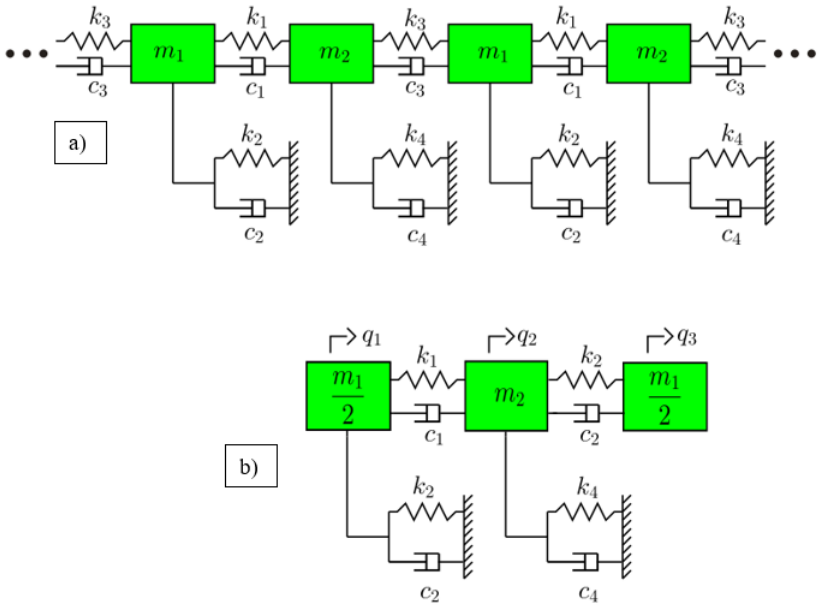

Source: The author.

The equations of motion for the unit cell are given below:

$$\begin{gathered}\frac{m_1}{2}\ddot{q}_1+(c_1+c_2)\,\dot{q}_1-c_2\dot{q}_2+(k_1+k_2)\,q_1-k_2q_2=f_1\\ m_2\ddot{q}_2-c_2\dot{q}_1+(c_2+c_3+c_4)\,\dot{q}_2-c_4\dot{q}_3-k_2q_1+(k_2+k_3+k_4)\,q_2-k_4q_3=f_2\\ \frac{m_1}{2}\ddot{q}_3-c_2\dot{q}_2+c_2\dot{q}_3-k_2q_2+k_2q_3=f_3\end{gathered}\tag{4.11}$$

Following the steps of section 2.1, it is useful to place Eq. (4.11) in matrix form:

$$\mathbf{M}=\begin{bmatrix}\frac{m_1}{2}&0&0\\0&m_2&0\\0&0&\frac{m_1}{2}\end{bmatrix},\mathbf{C}=\begin{bmatrix}c_1+c_2&-c_2&0\\-c_2&c_2+c_3+c_4&-c_4\\0&-c_2&c_2\end{bmatrix},\mathbf{K}=\begin{bmatrix}k_1+k_2&-k_2&0\\-k_2&k_2+k_3+k_4&-k_4\\0&-k_2&k_2\end{bmatrix}\tag{4.12}$$

The damping matrix $\mathbf{C}$ in the second case is also non-proportional, as $\mathbf{KM^{-1}C}\neq\mathbf{CM^{-1}K}$. Using the modal coordinates approach along with the light damping assumption to obtain the damping ratio values, the following damping ratio expression is obtained for the first vibrating mode of the unit cell:

$$\zeta_1=\frac{0.0251c_1+0.0217c_2+0.0933c_3+5.34E-4c_4}{2\omega_1}\tag{4.13}$$

It is observed in Eq. (4.13) that the damping ratio is a function of several damping coefficients, and that several combinations of their values would lead to the same damping

ratio at the first resonant frequency of the unit cell. Then, for the analysis of the second case, it was chosen $c_1 = c_2 = c_4 = 1\ Ns/m$ and thus, c_3 is calculated in function of the damping ratio values provided in Table 4.1.(4.1).

The FRF of the unit cell and the periodic structure for different damping models and various damping ratios are plotted respectively in Figure 4.12 and Figure 4.13:

Figure 4.12 – FRF of the unit cell for different damping ratios, a) non prop viscous damping, b) proportional viscous damping and c) hysteretic damping

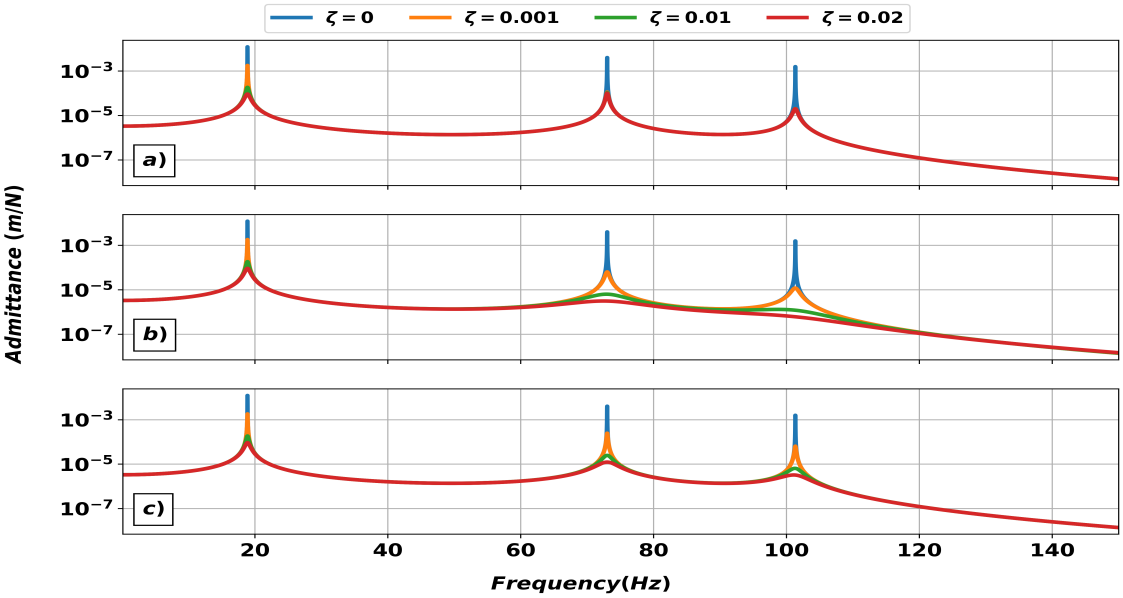

Source: The author.

Figure 4.13 – FRF of the unit cell for different damping ratios, a) non prop viscous damping, b) proportional viscous damping and c) hysteretic damping

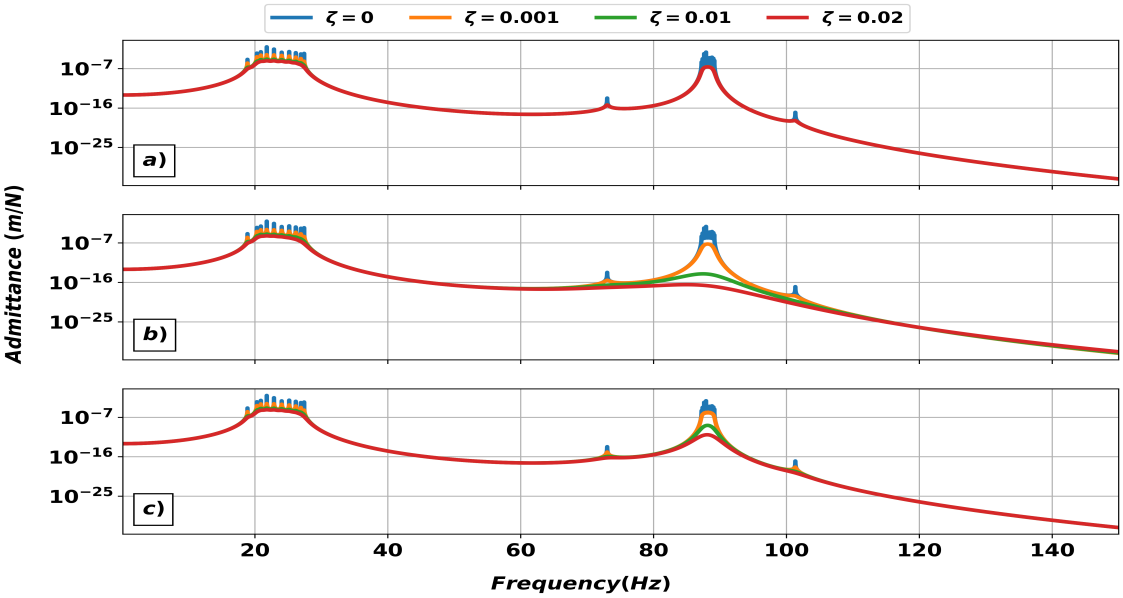

Source: The author.

In Figure 4.13, three distinct band gap intervals are detectable: 0-19 Hz, 27-87 Hz and 89 Hz and above. An interesting phenomenon is the band gap merging caused by damping the first mode of the periodic structure. As the damping ratio increases, the admittance level located between the first and second band gap intervals decreases. The proportional damping greatly attenuates the resonant modes between 80-100 Hz, followed by the hysteretic damping. The non-proportional viscous attenuates the resonant modes in this frequency range only by a small amount. It can be observed resonant modes inside band gaps, one located approximately at 75 Hz and the second one at 103 Hz. These resonant modes are attenuated as the damping ratio increases, regardless of the damping model utilized. Therefore, it is a good strategy to add damping to periodic structures when resonant modes are present inside band gaps, as it will reduce the vibrational amplitude if the structure is submitted to harmonic forces of the same resonance frequency located inside the band gaps.

The dispersion diagrams of the periodic structure for different damping ratio values and damping models are depicted in Figure 4.14:

Figure 4.14 – Dispersion diagram of Case 1: a1) attenuation factor for NPVD, b1) attenuation factor for PVD, c1) attenuation factor for HD, a2) phase constant for NPVD, b2) phase constant for PVD, c1) phase constant for HD

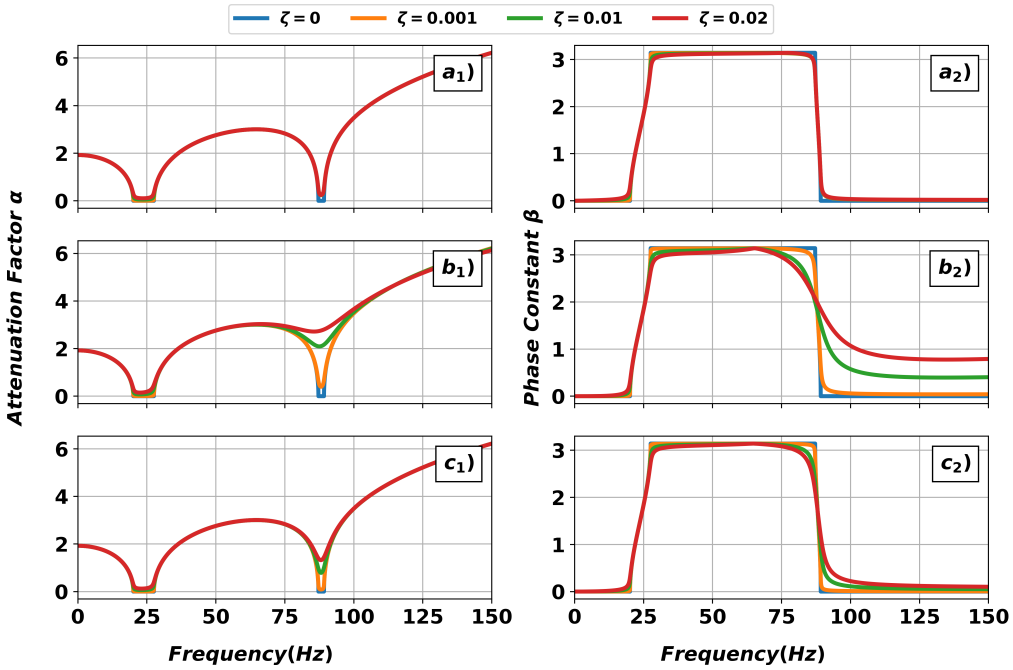

Source: The author.

Similar to Case 1, adding damping to the periodic structure contributes to attenuate the vibration levels where the pass bands are located, as it is seen in Figure 4.14. The band gap merging phenomenon is observed for the proportional damping in Figure 4.14 b_1) when $\zeta = 0.02$. This phenomenon could also be observed for the hysteretic damping if an increased damping ratio value were used. The non-proportional viscous damping shows almost no

modification in the attenuation factor values regardless of damping ratio values.

The phase constant values located in the transition zones between the pass bands and band gaps also do not reach the bounding values zero or π values, meaning that in these frequencies the adjacent unit cells of the periodic structure are never in or out of phase regarding each unit cell. The phase constant of the periodic structure using the proportional viscous damping model presents a great variation in its value for frequency range of 75-150 Hz as the damping ratio increases. For instance, when no damping ratio is applied, $\beta = 0$, and for $\zeta = 0.02$, $\beta = 0.9$ for a frequency value of 110 Hz. This is related to the higher amount of damping in this frequency range that the model presents as compared to the others. Notice that for the non-proportional viscous damping the phase constant value is almost the same regardless of damping ratio.

Moving to the viscoelastic damping model, the FRF of the viscoelastic damping model for Case 2 is compared against the proportional viscous and hysteretic damping for several damping ratio values, which are depicted Figure 4.15:

Figure 4.15 – FRF of Case 2 composed of ten cells for a) proportional viscous damping, b) hysteretic damping and c) viscoelastic damping model

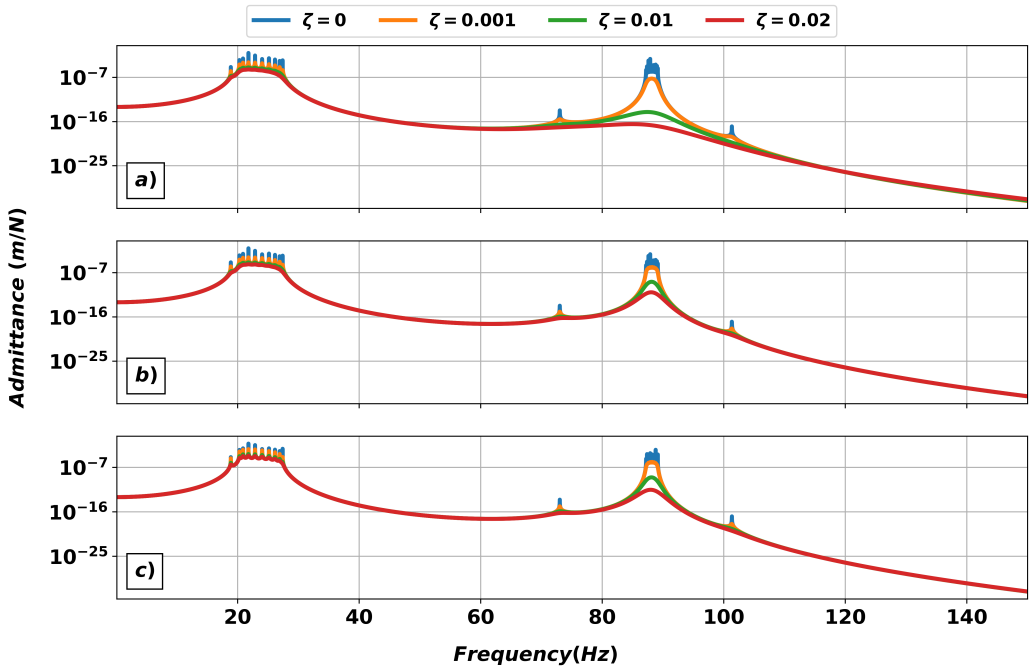

Source: The author.

As observed in Figure 4.15 c), the FRF of the viscoleastic damping model looks similar to the hysteretic damping model in in 4.15 b) due to similar loss factor values across the frequencies of the viscoelastic case. The proportional viscous damping follows this behavior until reaching the frequency range of 82 - 95 Hz. When entering the third band gap region, this damping model possess similar values compared to the other two.

The dispersion diagram of Case 2 including the viscoelastic damping model is shown in Figure 4.16:

Figure 4.16 – Dispersion diagram of Case 2: a1) attenuation factor for PVD b1) attenuation factor for HD, c1) attenuation factor for VD, a2) phase constant for PVD, b2) phase constant for HD, c1) phase constant for VD

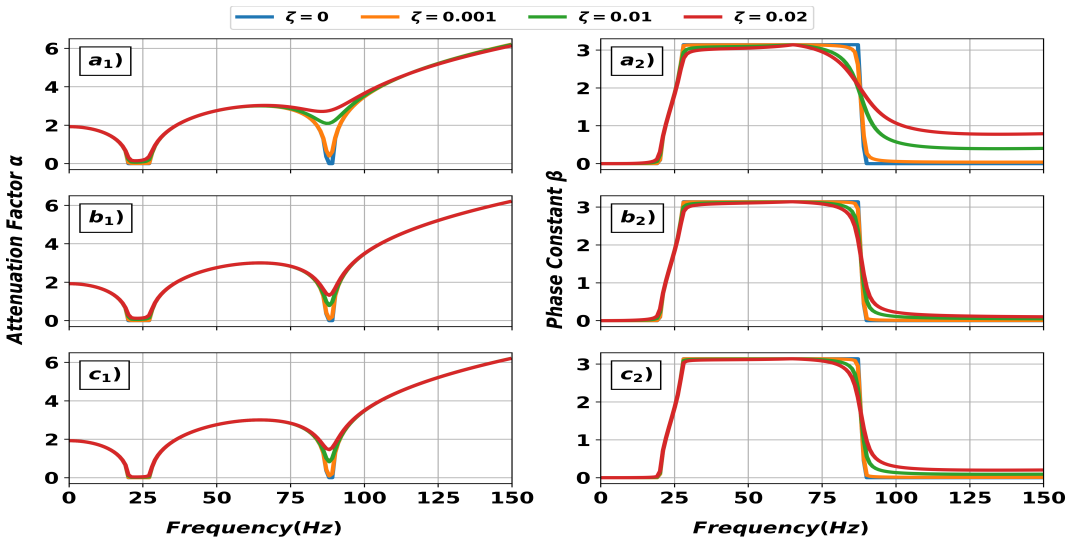

Source: The author.

The dispersion diagram in Figure 4.16 is in accordance with the FRF results obtained in Figure 4.15. The hysteretic and viscoelastic damping models possess similar values both in attenuation factor and phase constant across all the frequencies studied. The proportional viscous damping differs from the other models starting from 82 Hz, where it can be seen a high attenuation factor value between 82 - 95 Hz. As for the phase constant, both hysteretic and viscoelastic damping present similar values across all the frequencies. The phase constant of the proportional viscous damping diverges from the other models mentioned, with $\beta = 0.9$ for frequencies above 95 Hz, whereas the other models have $\beta = 0.2$ also for frequencies above 95 Hz.

Finally, the effect of temperature in the FRF of Case 2 is shown in Figure 4.17:

Figure 4.17 – FRF of Case 2 composed of ten cells for viscoelastic damping model with temperature effect

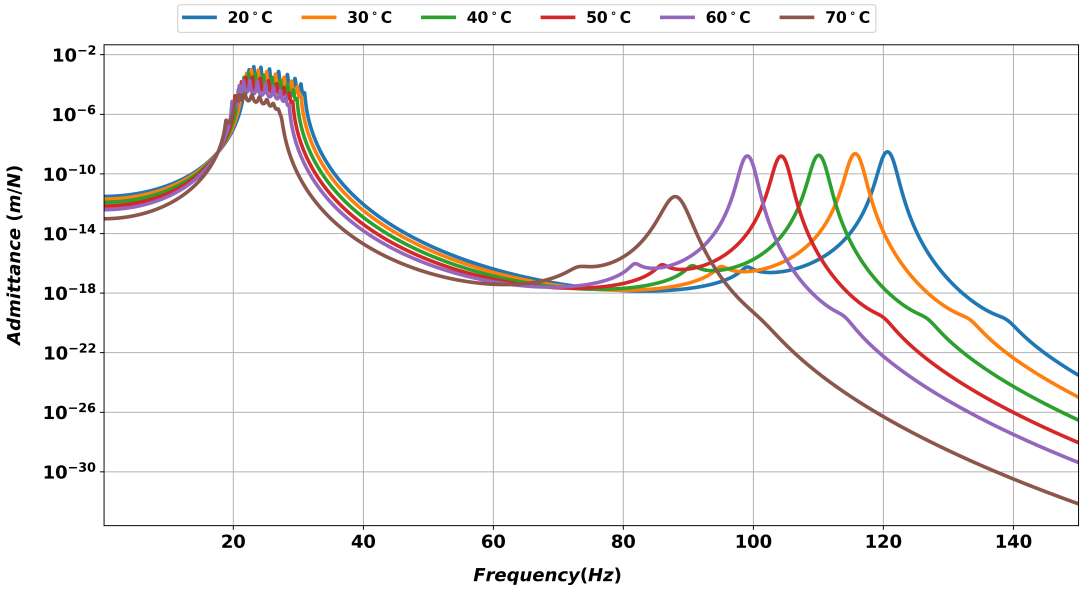

Source: The author.

As in Figure 4.9, the band gaps in Figure 4.17 are shifted when the temperature decreases due to increased stiffness at low temperatures. This effect was also observed in Case 1, where the FRF was shifted to lower frequencies as the temperature increases. Since the loss factor is high at elevated temperature, it is observed the smoothing of resonant peaks at increased temperature.

The dispersion diagram with the temperature effect is shown in Figure 4.18:

Figure 4.18 – Dispersion diagram of Case 2 for viscoelastic damping model with temperature effect

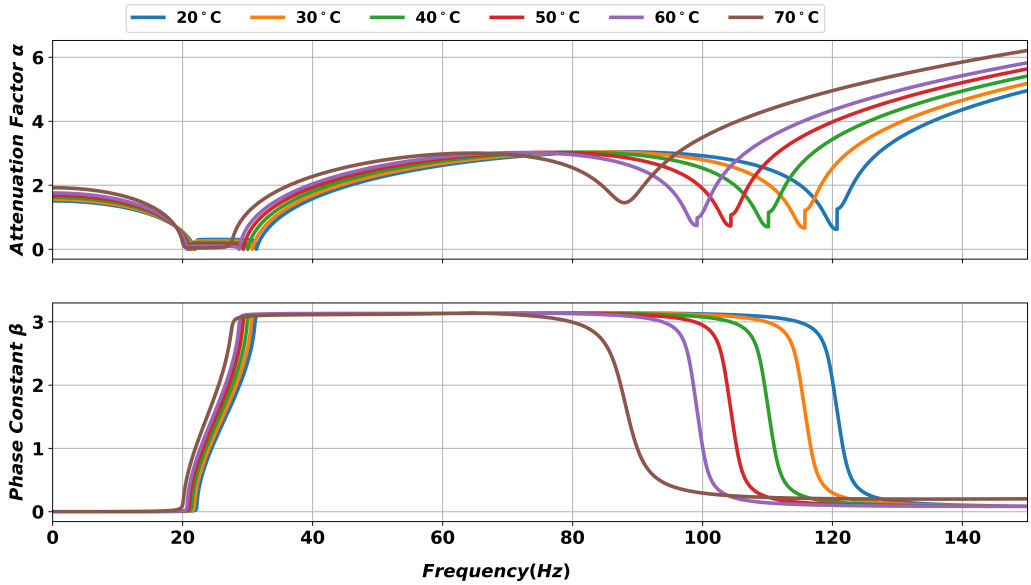

Source: The author.

Once again, the dispersion diagram of Figure 4.18 corroborates the FRF in Figure 4.17. It is observed the shift in the attenuation factor and in the phase constant plots. Moreover, the attenuation factor increases with temperature, which was expected due to the higher loss factor presented in the master curves in Figure 4.8 at higher frequencies and temperatures.

From all the results obtained above, the followings comments are made. First, it could be observed a new band gap region at low frequency, this being a contribution from the grounded springs and dampers attached to the masses. As for the effect of damping models, as opposed to Case 1, it was observed different level of attenuation in the pass bands when varying the damping ratios. The proportional viscous damping presented a high level of attenuation in the second pass band region, leading to a band gap merging phenomenon between the second and third band gap region. The hysteretic damping also provided some level of attenuation in the second pass band region. The viscoelastic damping model provided similar level of attenuation compared to hysteretic damping in the second pass band region when varying the damping ratio. When using the frequency-temperature effect on the viscoelastic material, similar results were obtained as in Case 1, where the band gaps and pass bands are shifted, and the attenuation in pass bands increases with temperature.

4.1.3 Case 3: Damped monoatomic metamaterial

The third case investigated is a damped monoatomic metamaterial. In this case, this is the classical vibration absorber system, with an absorber mass attached to the periodic structure. This topology generates the classical local resonance at low frequencies in periodic structures. Herein, the contribution of adding dampers to the resonant masses and their effect in band gaps and pass bands is investigated. The system along with its unit cell is depicted in Figure 4.19:

Figure 4.19 – FRF of the unit cell for different damping ratios, a) non prop viscous damping, b) proportional viscous damping and c) hysteretic damping

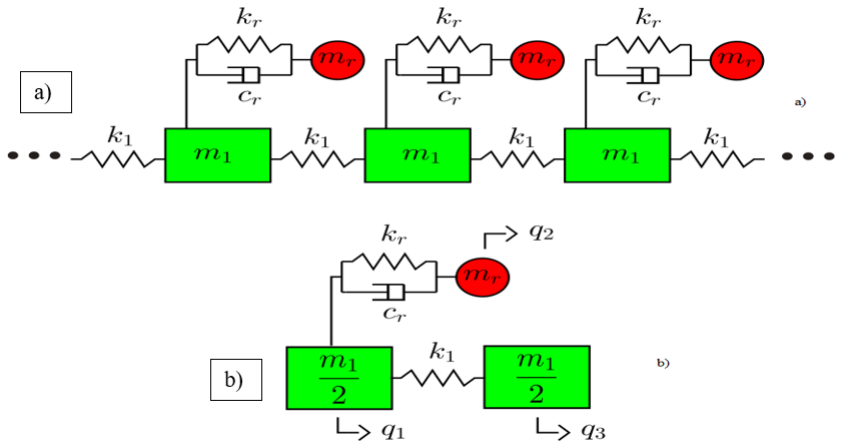

Source: The author.

The equations of motion for the unit cell are:

$$\begin{aligned} \frac{m_1}{2}\ddot{q}_1 + c_r\left(\dot{q}_1 - \dot{q}_2\right) + k_1\left(q_1 - q_3\right) + k_r\left(q_1 - q_2\right) &= f_1 \\ m_r\ddot{q}_2 + c_r\left(\dot{q}_2 - \dot{q}_1\right) + k_r\left(q_2 - q_1\right) &= f_2 \\ \frac{m_1}{2}\ddot{q}_3 + k_1\left(q_3 - q_1\right) &= f_3 \end{aligned} \tag{4.14}$$

Placing Eq. 4.14 in matrix form, the mass, damping and stiffness matrix are obtained:

$$\mathbf{M} = \begin{bmatrix} \frac{m_1}{2} & 0 & 0 \\ 0 & m_r & 0 \\ 0 & 0 & \frac{m_1}{2} \end{bmatrix}, \mathbf{C} = \begin{bmatrix} c_r & -c_r & 0 \\ -c_r & c_r & 0 \\ 0 & 0 & 0 \end{bmatrix}, \mathbf{K} = \begin{bmatrix} k_1 + k_r & -k_r & -k_1 \\ -k_r & k_r & 0 \\ -k_1 & 0 & k_1 \end{bmatrix} \tag{4.15}$$

Unlike the previous cases, it can be seen in Eq 4.15 that there is no way to build a damping matrix proportional to the stiffness matrix. In this manner, only non-proportional viscous and hysteretic damping analysis will be available in this section.

The damping ratio expression for the first vibrating mode is:

$$\zeta_1 = \frac{0.597 c_r}{2\omega_1} \tag{4.16}$$

The FRF for the unit cell and periodic structure using different damping models and damping ratios are shown in Figure 4.20 and Figure 4.21:

Figure 4.20 – FRF of the unit cell for different damping ratios: a) non-proportional viscous damping and b) hysteretic damping

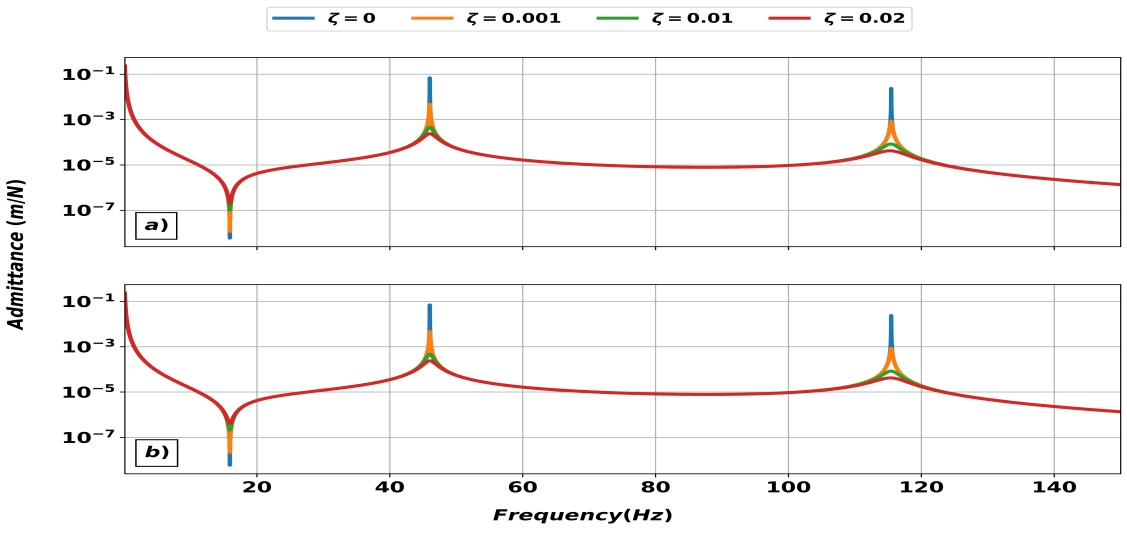

Source: The author.

Figure 4.21 – FRF of Case 3 for: a) non-proportional viscous damping and b) hysteretic damping

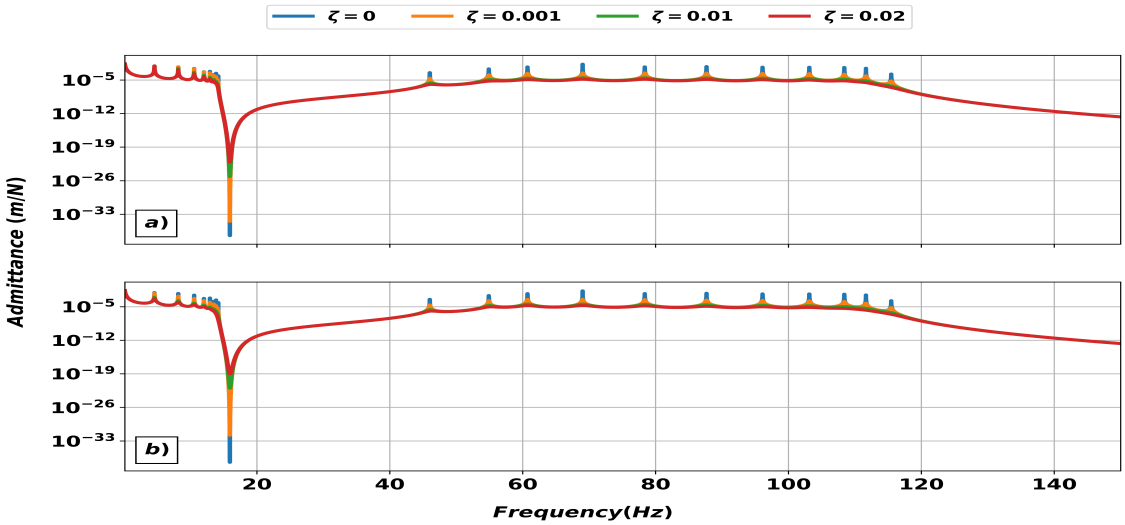

Source: The author.

In Figure 4.21 the band gap due to a local resonance is found at the frequency value of approximately 15.9 Hz. The damping ratio contributes to lower the admittance level in that band gap region, thus it is not convenient to add a damper in the resonant mass if the intention is to lower the vibration amplitude of the periodic structure. Moreover, it is observed that hysteretic damping provides more attenuation in the local resonance. This is explained by the fact that the damping ratio values for all resonant frequencies are the same, regardless of excitation frequency, as observed in Eq. 3.20, whereas viscous damping ratio values increases proportionally with frequency, as in Eqs. 3.17 and 3.18.

The dispersion diagram of the damped monoatomic MM is illustrated in Figure 4.22:

Figure 4.22 – Dispersion diagram of Case 3 for: a) non-proportional viscous damping and b) hysteretic damping

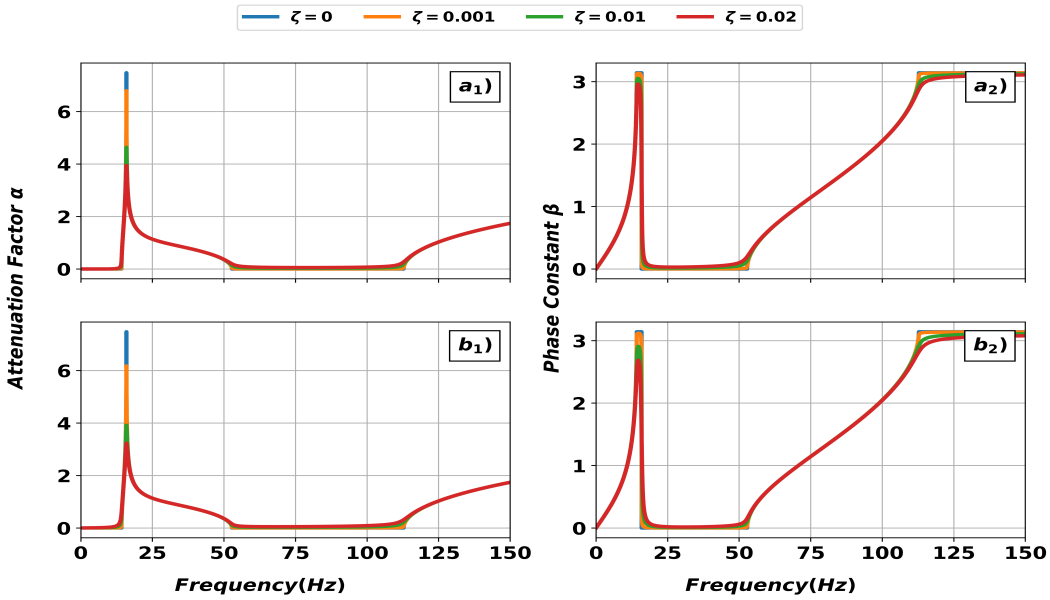

Source: The author.

The dispersion diagram in Figure 4.22 shows the attenuation factor being reduced at the frequency range of approximately 16 Hz when the damping ratio is increased, corroborating the FRF in Figure 4.21. The phase constant value for both damping models did not change too much, excep in the resonance frequency of 16 Hz where it is observed a lower phase constant value of the hysteretic damping compared to the non-proportional viscous damping.

Lastly, we incorporate the viscoelastic damping model in case 3. In Figure 4.23 it is plotted the FRF of the periodic structure using the non-proportional viscous damping (NPVD) , hysteretic damping (HD) and viscoelastic damping model (VD).

Figure 4.23 – FRF of Case 3 for: a1) attenuation factor for NPVD b1) attenuation factor for HD, c1) attenuation factor for VD, a2) phase constant for PVD, b2) phase constant for HD, c1) phase constant for VD

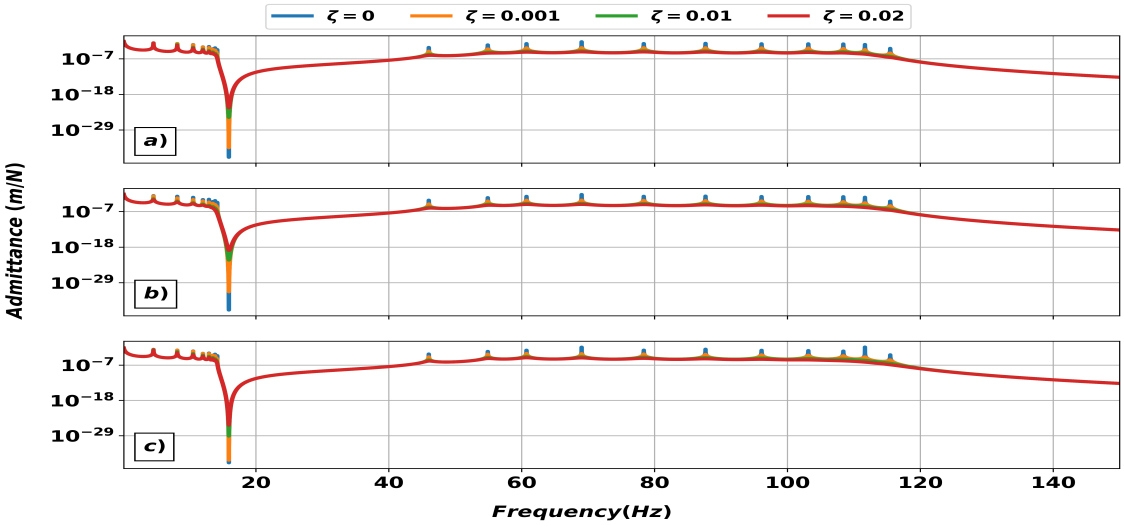

Source: The author.

The admittance level of the periodic structure using the viscoelastic damping model in Figure 4.23 c) is similar to the NPVD in Figure 4.23 a) at the resonant frequency of 16 Hz, whereas the hysteretic damping model in Figure 4.23 b) has the highest admittance level compared to the other models.

The dispersion diagram with the viscoelastic damping model is shown in Figure 4.24:

Figure 4.24 – Dispersion diagram of Case 3: a1) attenuation factor for NPVD b1) attenuation factor for HD, c1) attenuation factor for VD, a2) phase constant for PVD, b2) phase constant for HD, c1) phase constant for VD

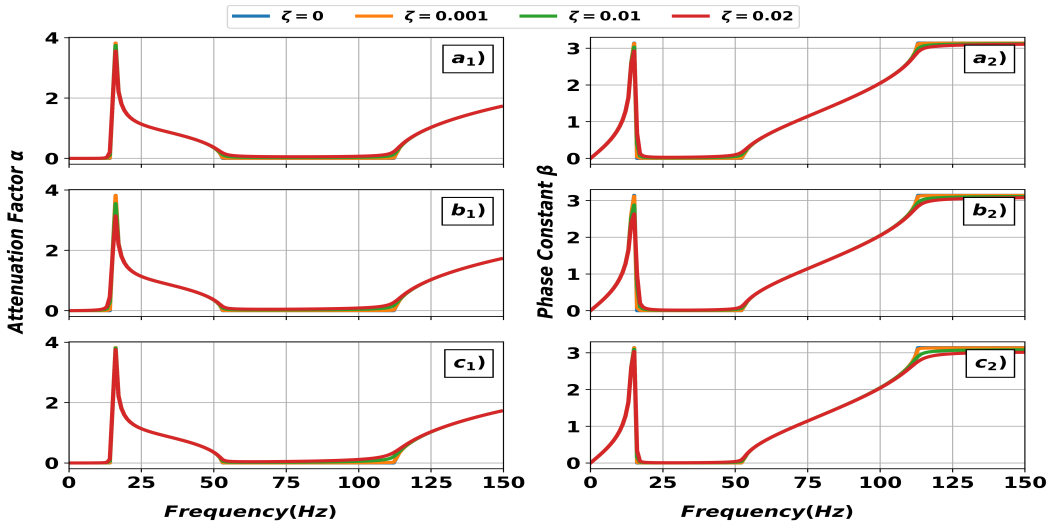

Source: The author.

From Figure 4.24 it is observed the similarities in the magnitude of the attenuation factor of the NPVD and VD, corroborating the FRF of the periodic structure in 4.23.

Finally, the effect of temperature in the periodic structure for Case 3 is depicted in Figure 4.25, showing the FRF of the periodic structure.

Figure 4.25 – FRF of Case 3 composed of ten cells for viscoelastic damping model with temperature effect

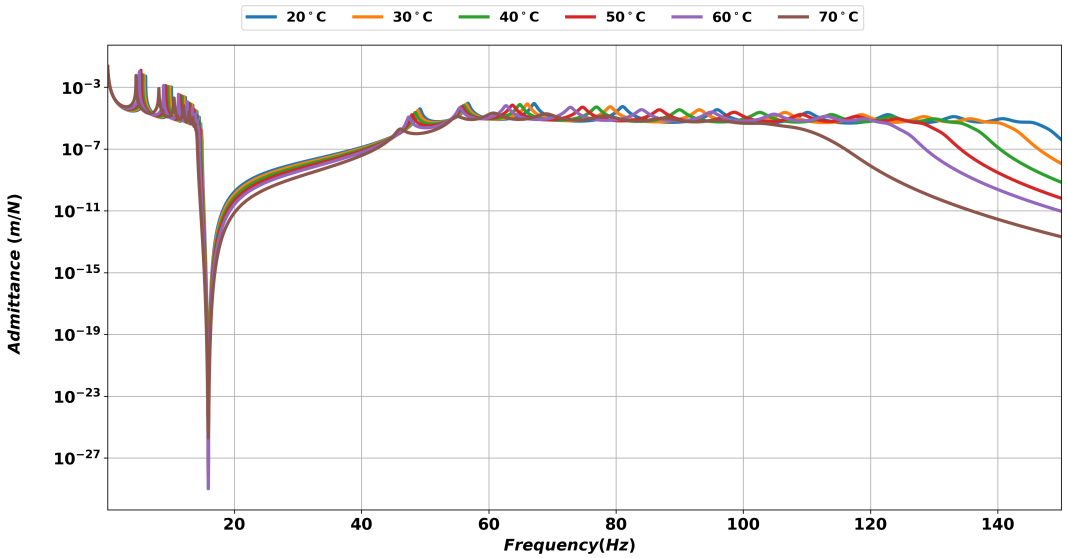

Source: The author.

Observing Figure 4.25, it is noticed that the local resonance around the frequency of 16 Hz attains its minimum value at a temperature of 70 ^{o}C, and its maximum value at a temperature of 60 ^{o}C rather than 20 ^{o}C, even though the loss factor decreases with temperature. In this case, there is a tradeoff between the stiffness and loss factor. The loss factor is predominant for the behavior of the local resonance peak at 70 ^{o}C whereas the stiffness is dominant at the temperature of 60 ^{o}C and below, meaning that the local resonance decreases as the stiffness of the VEM increases with lower temperatures, as seen in Figure 4.8. Moreover, it is observed a shift in the band gap with its origin at the frequency of 100 Hz at 70 ^{o}C. As the temperature decreases, this band gap is shifted to higher frequencies. In Figure 4.26 it is shown the dispersion diagram of the periodic structure of Case 3:

Figure 4.26 – Dispersion diagram of Case 3 for viscoelastic damping model with temperature effect

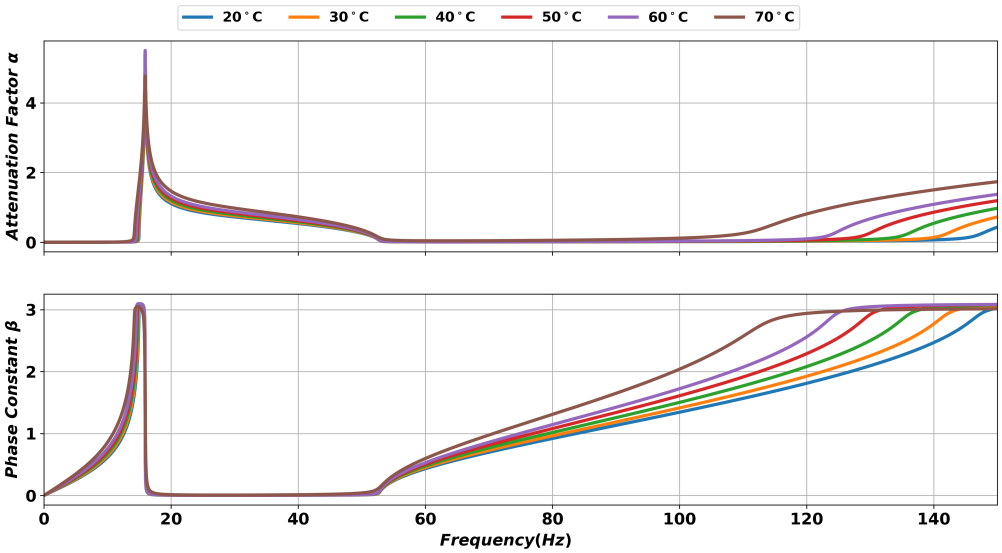

Source: The author.

Similarly to what was obtained in the FRF of Figure 4.25, it is observed that the attenuation factor value at 16 Hz decreases with temperature in the dispersion diagram. It is also noticed the shift in band gaps to lower frequencies as the temperature increases. Same conclusions are obtained for the phase constant in the dispersion diagram.

It could be observed that the local resonance is affected when applying different damping models. The hysteretic damping did attenuate the local resonance compared to the non-proportional viscous damping. Both damping models also attenuate the resonant peaks, and no effects on band gaps related to shifting or band gap merging was observed. The viscoelastic damping model has also attenuated the local resonance, with results similar to the other damping models. When introducing the frequency-temperature dependency, shifts in band gaps were observed at higher frequencies, and a minimal level of attenuation was observed in the local resonance, with a slightly shift of the local resonance when increasing the temperature.

4.1.4 Case 4: Damped monoatomic metamaterial with damped mass chain

The last case is a damped monoatomic metamaterial with damped mass chain. This system is similar to Case 3, except that there are dampers attached to the main mass chain, and so the contribution of these dampers are investigated herein. The system topology and its unit cell are represented in Figure 4.27 a) and b):

Figure 4.27 – FRF of the unit cell for different damping ratios, a) non prop viscous damping, b) proportional viscous damping and c) hysteretic damping

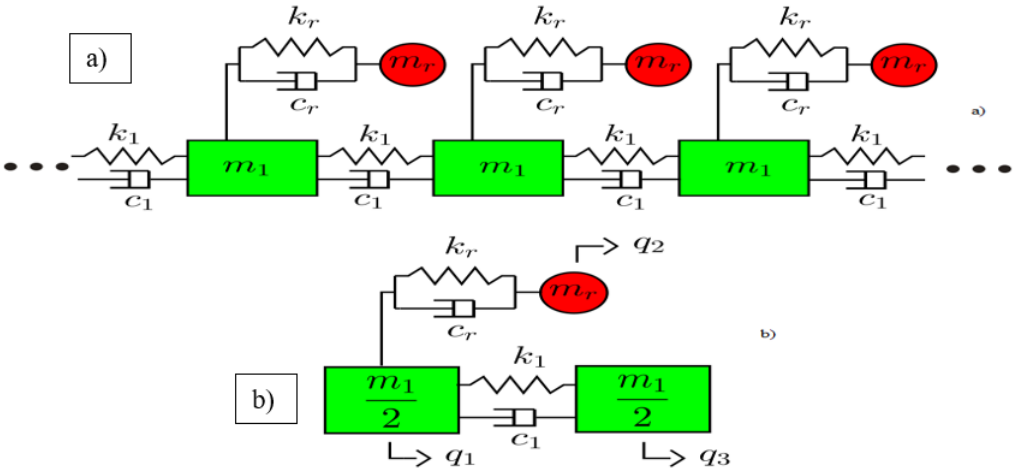

Source: The author.

The equations of motion for the unit cell are given in Eq. (4.17):

$$\begin{aligned} \frac{m_1}{2}\ddot{q}_1 + c_1\left(\dot{q}_1 - \dot{q}_3\right) + c_r\left(\dot{q}_1 - \dot{q}_2\right) + k_1\left(q_1 - q_3\right) + k_r\left(q_1 - q_2\right) &= f_1 \\ m_r\ddot{q}_2 + c_r\left(\dot{q}_2 - \dot{q}_1\right) + k_r\left(q_2 - q_1\right) &= f_2 \\ \frac{m_1}{2}\ddot{q}_3 + c_1\left(\dot{q}_3 - \dot{q}_1\right) + k_1\left(q_3 - q_1\right) &= f_3 \end{aligned} \tag{4.17}$$

Next, the mass, damping and stiffness matrix are obtained from Eq. (4.17):

$$\mathbf{M} = \begin{bmatrix} \frac{m_1}{2} & 0 & 0 \\ 0 & m_r & 0 \\ 0 & 0 & \frac{m_1}{2} \end{bmatrix}, \mathbf{C} = \begin{bmatrix} c_1 + c_r & -c_r & -c_1 \\ -c_r & c_r & 0 \\ -c_1 & 0 & c_1 \end{bmatrix}, \mathbf{K} = \begin{bmatrix} k_1 + k_r & -k_r & -k_1 \\ -k_r & k_r & 0 \\ -k_1 & 0 & k_1 \end{bmatrix} \tag{4.18}$$

The expression for the damping ratio of the first vibrating mode of the unit cell is shown below:

$$\zeta_1 = \frac{0.239c_1 + 0.597c_r}{2\omega_1} \tag{4.19}$$

In this case, Eq. (4.19) shows that the damper of the resonant mass has more influence in the overall damping of the unit cell, as its coefficient is greater than the damper between the two masses.

For the FRF of the unit cell and periodic structure, the damper value between the two masses is set to $c_1 = 1$, thus c_r is calculated from chosen ζ values. Figure 4.28 and Figure 4.29 show the FRF of the unit cell and the periodic structure respectively:

Figure 4.28 – FRF of the unit cell for different damping ratios, a) non prop viscous damping, b) proportional viscous damping and c) hysteretic damping

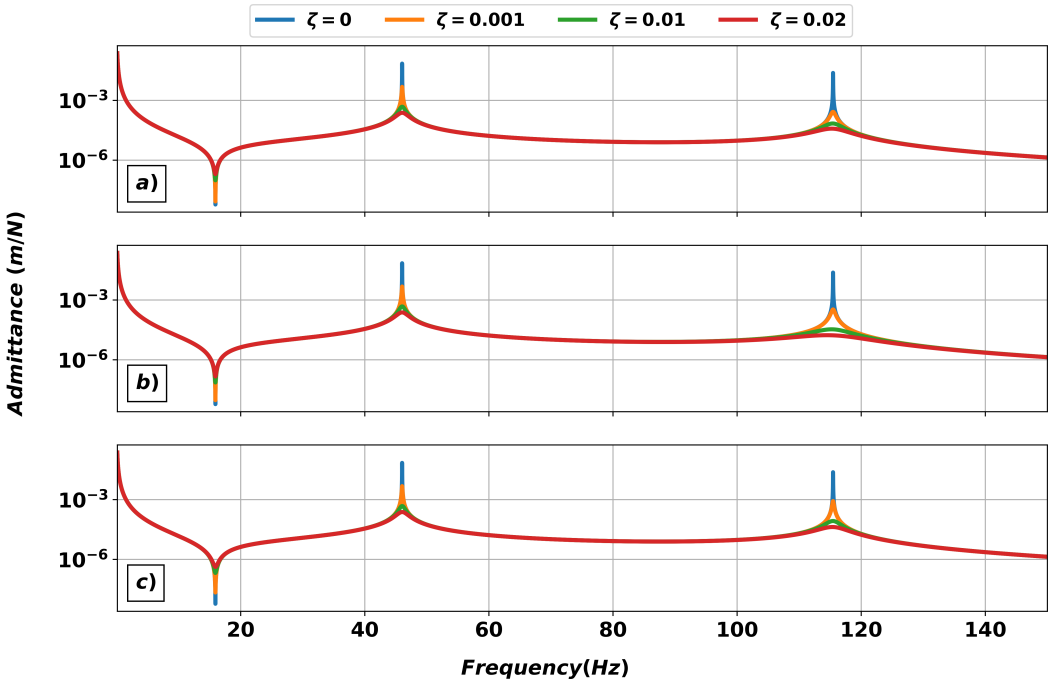

Source: The author.

Figure 4.29 – FRF of the periodic structure composed of ten unit cells in Case 4 for: a) non prop viscous damping, b) proportional viscous damping and c) hysteretic damping

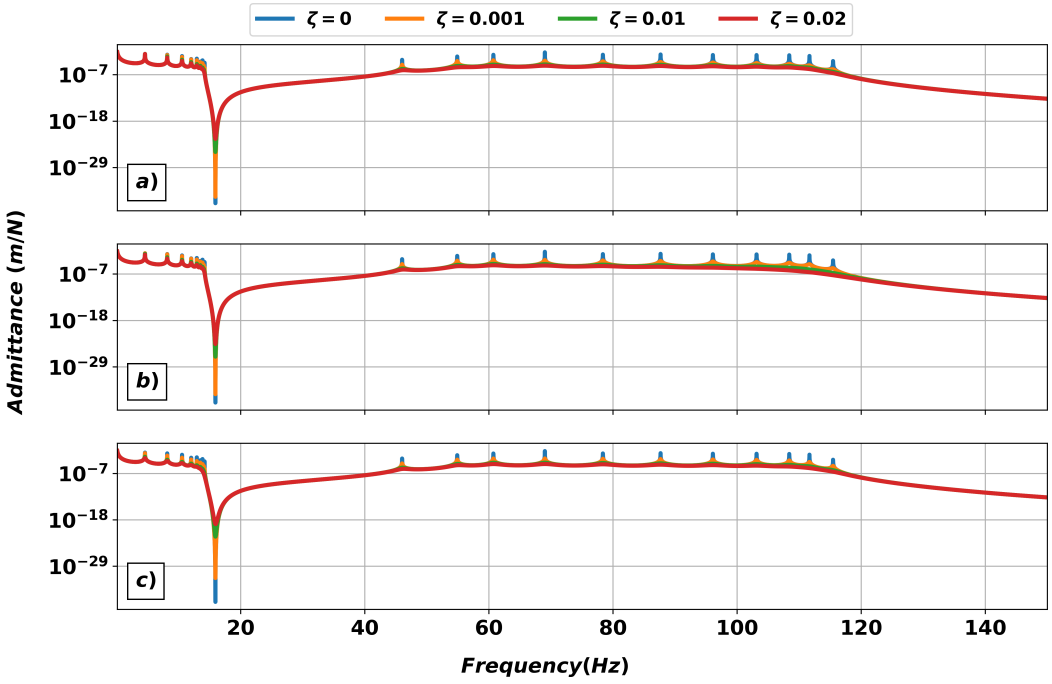

Source: The author.

The results expressed in the FRF plots above are similar to those obtained in section

4.1.3. The addition of a damper between the main masses of the unit cell did not affect the local resonance located at 16 Hz. Similar to Case 3, the increasing in the damping ratio value drives the local resonance to lower admittance level, hence helping elastic wave propagation along the structure. In Figure 4.30 the dispersion diagram is depicted, corroborating the FRF plots:

Figure 4.30 – Dispersion diagram of Case 1: a1) attenuation factor for NPVD, b1) attenuation factor for PVD, c1) attenuation factor for HD, a2) phase constant for NPVD, b2) phase constant for PVD, c1) phase constant for HD

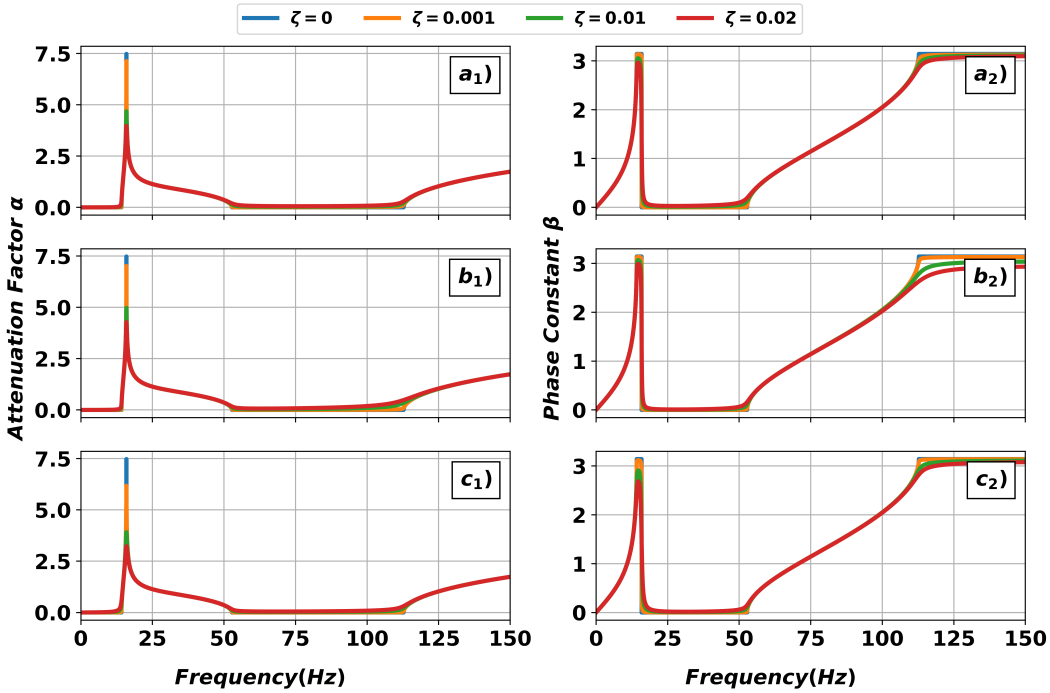

Source: The author.

The results for the dispersion curves depicted in Figure 4.30 is similar to those in Figure 4.22. The attenuation factor value around the local resonance frequency decreases as the damping ratio varies upward. The insertion of dampers in the main chain doesn't seem to affect the overall behavior of the wave propagation across the structure. Moreover, it can be seen in phase constant diagram the IBZ values not reaching its bounding values.

Next, it is compared the FRF of the periodic structure using the viscoelastic damping model against the proportional and hysteretic model. In Figure 4.31 it is shown such comparison:

Figure 4.31 – FRF of Case 4 composed of ten cells for a) proportional viscous damping, b) hysteretic damping and c) viscoelastic damping model

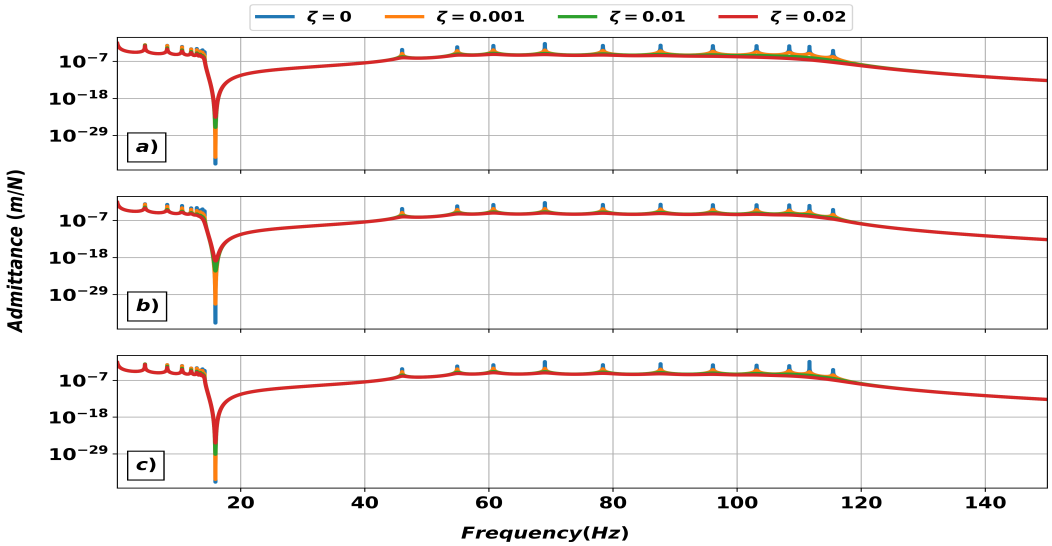

Source: The author.

The local resonance of the periodic structure using the viscoelastic damping model in Figure 4.31 c) is similar to that of the proportional damping model in Figure 4.31 a) due to similar loss factor value around the frequency of 16 Hz. Since the loss factor of the hysteretic damping model is greater than the other damping models, the local resonance admittance value around that frequency is smaller.

The dispersion diagram of Case 4 for the proportional, hysteretic and viscoelastic damping models is shown in Figure 4.32:

Figure 4.32 – Dispersion diagram of Case 4: a1) attenuation factor for PVD b1) attenuation factor for HD, c1) attenuation factor for VD, a2) phase constant for PVD, b2) phase constant for HD, c1) phase constant for VD for different damping ratios

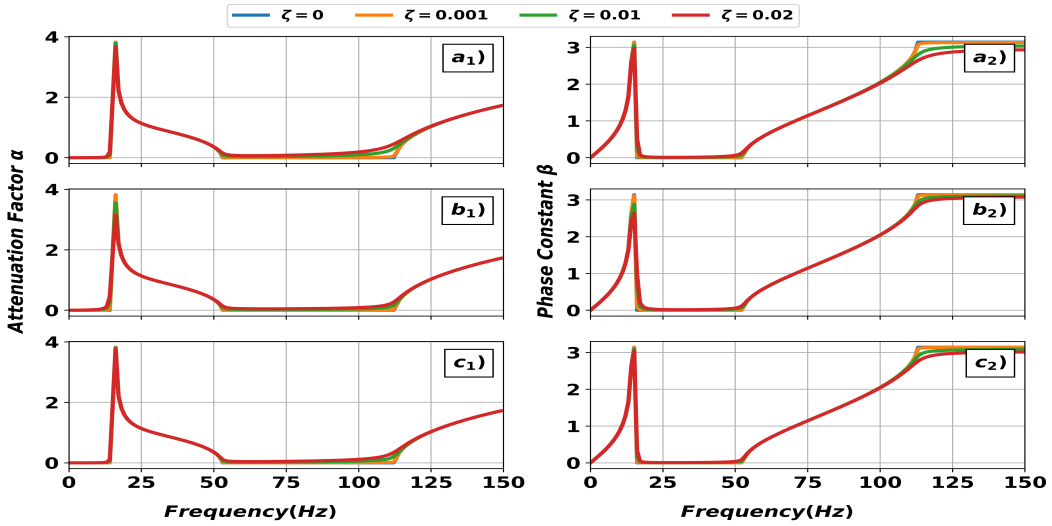

Source: The author.

Observing Figure 4.32 b_1) it is noticed the attenuation factor of the hysteretic damping model around the frequency of 16 Hz possessing a smaller value when compared to the other damping models, hence validating the FRF obtained in Figure 4.31.

The influence of temperature in the viscoelastic model for the FRF of the periodic structure of Case 4 is shown in Figure 4.33:

Figure 4.33 – FRF of Case 4 composed of ten cells for viscoelastic damping model with temperature effect

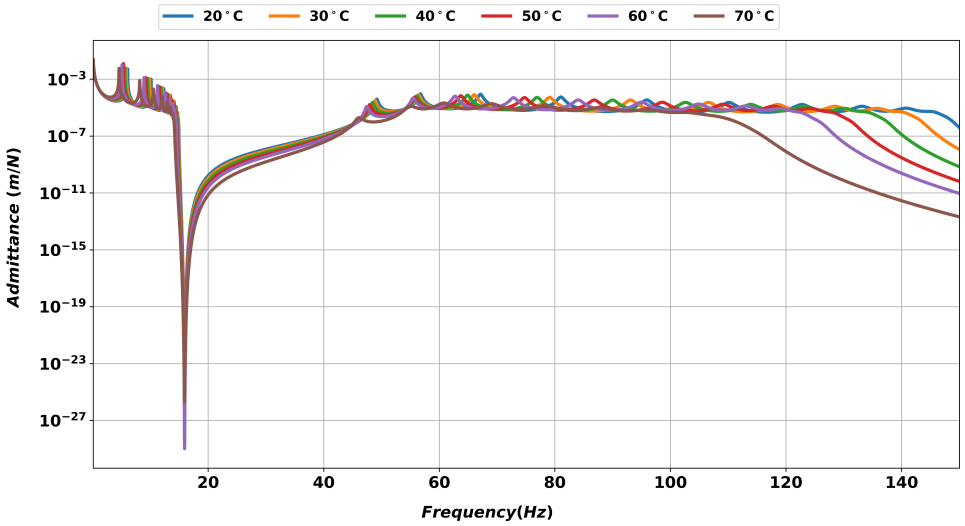

Source: The author.

It can be noticed in Figure 4.33 the shift in band gap starting from 100 Hz for higher temperatures. Interestingly, the temperature does not affect the location of resonance around 16 Hz. The width of the local resonance band gap is slightly increases with temperature. Regarding the peak value of the local resonance, the same conclusions drawn from Case 3 can be applied here, where there is a tradeoff between loss factor and VEM stiffness. The dispersion diagram of the unit cell of Case 4 is shown in Figure 4.34:

Figure 4.34 – Dispersion diagram of Case 4 for viscoelastic damping model with temperature effect

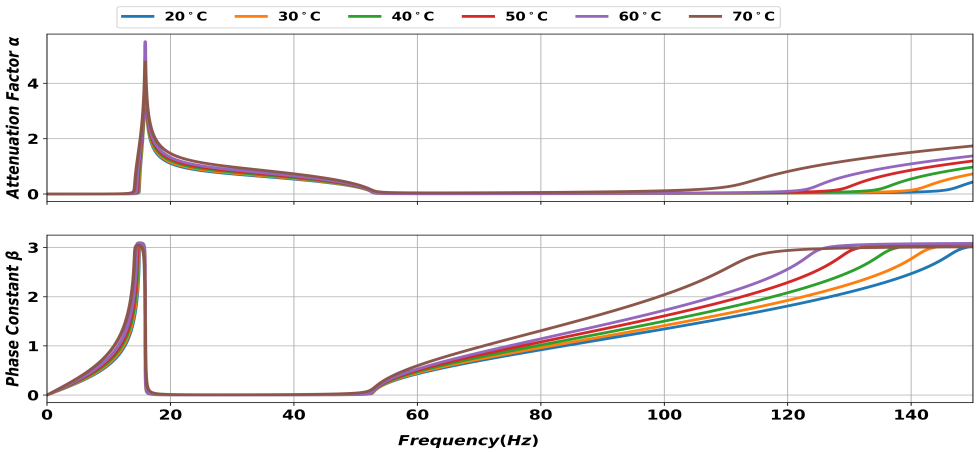

Source: The author.

The dispersion diagram of Figure 4.34 contain shifts in the attenuation factor and phase constant as the temperature increases, especially in higher frequencies, hence validating the FRF obtained in Figure 4.33.

It is not clear the contribution of the dampers to the periodic mass chain in Case 4. The results in terms of attenuation of band gaps and pass bands are similar to Case 3. With the addition of these dampers, it was possible to construct a stiffness proportional damping matrix, enabling the study of proportional viscous damping in this structure. Nonetheless, results between proportional and non-proportional viscous damping looks similar. Using viscoelastic damping model with frequency-temperature dependency, the shifts in band gaps to higher frequencies could be observed when increasing the temperature, similar to Case 3.

To summarize the results of this section, the following observations are made:

- Regardless of damping model, those contribute to the attenuation of pass bands, whereas the band gaps do not change in width nor location, except when using the viscoelastic damping model with frequency-temperature effect.
- With a minimal level of damping, the phase constant does not reach the bounding values zero or π, meaning that the phase difference of adjacent unit cells motion will never stay totally in or out of phase.
- Adding damping to the resonant masses in metamaterials contribute to lower the level of vibration attenuation. In this case, it is not ideal to add dampers, as it does not contribute to decrease the overall vibration in the structure.
- The viscoelastic damping model with frequency-temperature effect shifts the location of band gaps. Moreover, it also contributes to the attenuation of pass bands when subjected to higher temperatures. However, in reality, these effects will vary depending on the viscoelastic material utilized in the structure.

4.2 Damping modeling in periodic continuous systems

In this section the investigation of dissipative effects will take place in continuous systems, namely composite rods and sandwich beams, which are common periodic structures employed in mechanical systems to increase vibration attenuation. The finite element method will be employed to obtain the mass matrix and stiffness matrix of these systems. These matrices are required in the transfer matrix method to obtain the dispersion diagrams, as already shown in section 2.1.

For each system, different damping models will be applied similar to those in section 4.1 and the results in terms of FRF and dispersion diagrams are obtained. For the viscoelastic

damping model in particular, the effect of temperature in FRF and dispersion diagram is also investigated.

The proportional viscous damping is modeled by using the stiffness matrix factor υ previously shown in Eq. (3.15). In this case, the damping ratio ζ is obtained by adjusting the υ values.

The hysteretic damping is modeled by introducing the loss factor η, as in Eq. (3.20). The damping ratio ζ is given by adjusting the values of η.

Lastly, the viscoelastic damping is modeled via the Generalized Maxwell Model discussed in section 3.4. The damping ratio is obtained by adjusting the form factors γ_α and γ_ρ of the viscoelastic material.

4.2.1 Periodic Composite Rods

A rod is a slender member that supports only axial loads (DOYLE, 1991), and it is one of simplest components to model frames and trusses, being commonly found in periodic structures. Using the combination of a harder and softer material, it is possible to create mechanical impedance mismatches, leading to the formation of band gaps in the structure. This section will cover the influence of the damping models in band gaps and pass bands of composite rods. The next section will introduce the equations of motion of the composite rod using the finite element method.

4.2.1.1 Finite element modeling of rod

Consider the following rod element in Figure 4.35 with its degrees of freedom:

Figure 4.35 – Rod element

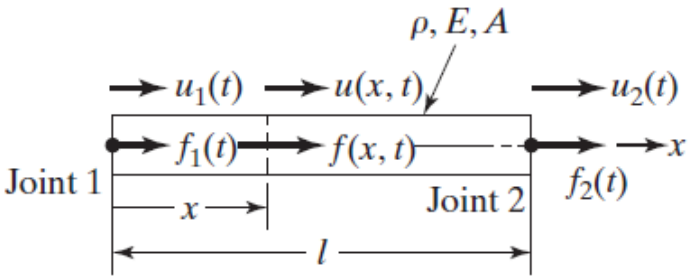

Source: (RAO, 2017).

The axial displacement of the rod is given by Eq. (4.20):

$$\mathbf{u}(x,t) = \mathbf{N_1}(x)u_1(t) + \mathbf{N_2}(x)u_2(t) \tag{4.20}$$

where the shape functions $\mathbf{N_1}$ and $\mathbf{N_2}$ are:

$$\begin{aligned} \mathbf{N_1}(x) &= (1 - \frac{x}{l}) \\ \mathbf{N_2}(x) &= \frac{x}{l} \end{aligned} \tag{4.21}$$

The strain energy of the rod element is given by:

$$V(t) = \int_0^l EA \left\{ \frac{\partial u(x,t)}{\partial x} \right\}^2 dx = \frac{1}{2} \frac{EA}{l} (u_1^2 - 2u_1 u_2 + u_2^2) \tag{4.22}$$

Defining:

$$\mathbf{u}(t) = \begin{bmatrix} u_1(t) \\ u_2(t) \end{bmatrix} \tag{4.23}$$

and by placing Eq. (4.22) in matrix form as:

$$V(t) = \frac{1}{2} \mathbf{u}(t)^T [\mathbf{K}] \mathbf{u}(t) \tag{4.24}$$

it can be seen that the stiffness matrix $\mathbf{K}$ is:

$$\mathbf{K} = \frac{EA}{L} \begin{bmatrix} 1 & -1 \\ -1 & 1 \end{bmatrix} \tag{4.25}$$

As for the mass matrix, the kinetic energy of the rod element:

$$T(t) = \frac{1}{2} \int_0^l \rho A \left\{ \frac{\partial u(x,t)}{\partial x} \right\}^2 dx = \frac{1}{2} \frac{\rho Al}{3} (\dot{u_1}^2 + \dot{u_1}\dot{u_2} + \dot{u_2}) \tag{4.26}$$

By placing Eq. (4.26) in matrix form we obtain:

$$T(t) = \frac{1}{2} \dot{\mathbf{u}}(t)^T [M] \mathbf{u}(t) \tag{4.27}$$

The mass matrix $\mathbf{M}$ is readily available from Eq. (4.27):

$$\mathbf{M} = \frac{\rho AL}{2} \begin{bmatrix} 1 & 0 \\ 0 & 1 \end{bmatrix} \tag{4.28}$$

The stiffness and mass matrices are used for the elastic and viscoelastic materials. In the next section, results for FRF and dispersion diagram of the composite rod are presented.

4.2.1.2 Results for periodic composite rod

In the work herein, the composite rod is composed of aluminum and the viscoelastic material ISD 112. In Figure 4.36 it is shown the composite rod structure:

Figure 4.36 – a) Composite rod composed of aluminum (green) and viscoelastic material (cyan) and b) Unit cell of composite rod

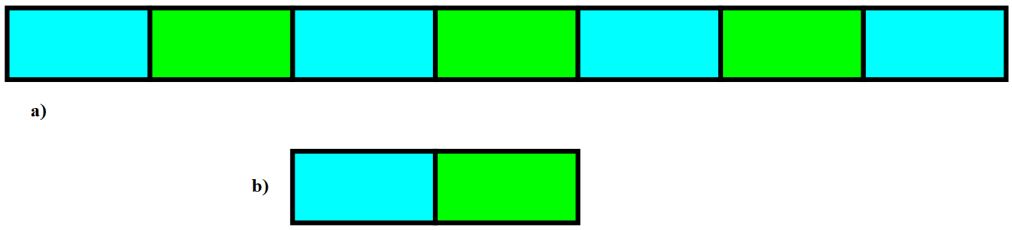

Source: The author.

The unit cell of the composite rod will be divided into twenty rod elements. For the unit cell of the composite rod, the dimensions and material parameters are listed in the table below:

Table 4.3 – Periodic composite rod material parameters at 24 ^{o}C.

Parameter	Value	Unit
E_{aluminum}	70	GPa
E_{ISD112}	1.28	MPa
L_{aluminum}	0.05	m
L_{ISD112}	0.05	m
A_{aluminum}	0.001	m^2
A_{ISD112}	0.001	m^2
d_{aluminum}	2700	kg/m^3
d_{ISD112}	1000	kg/m^3
ρ_i	[9.1 x 10^{-5}, 1.6 x 10^{-3}, 7.2 x 10^{-3}, 8.4 x 10^{-1}, 9.4 x 10^{-1}]	s
α_i	[13.2, 1.2, 0.2, 0.05, 0.02]	dimensionless

Source: The author.

where E is the elastic modulus, L is the length, d is the material density, A is the cross-sectional area, ρ_i is the relaxation time and α_i is the relative moduli of ISD 112 at a reference temperature of 24 ^{o}C.

The results of three damping models are retrieved. The damping ratio values are obtained for each damping model and the differences are observed. Similarly to what was done in section 4.1, the damping ratio is only applied to the first vibrating mode of the unit cell under free free boundary conditions, and its effect over the FRF of the last cell and dispersion diagram is observed along the periodic structure composed of ten unit cells.

The master curves of the viscoelastic material for various damping ratio are plotted in

Figure 4.37:

Figure 4.37 – Storage modulus and loss factor for several damping ratio values

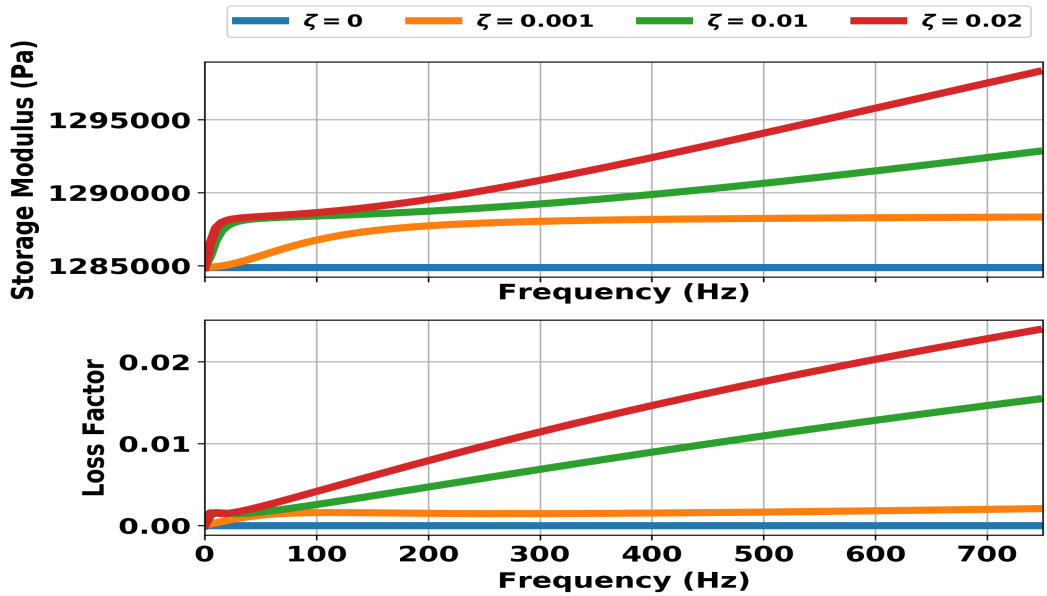

Source: The author.

In Figure 4.38 below the FRF response of the composite rod is depicted for the three damping models:

Figure 4.38 – FRF of composite rod for: a) proportional viscous damping, b) hysteretic damping and c) viscoelastic damping

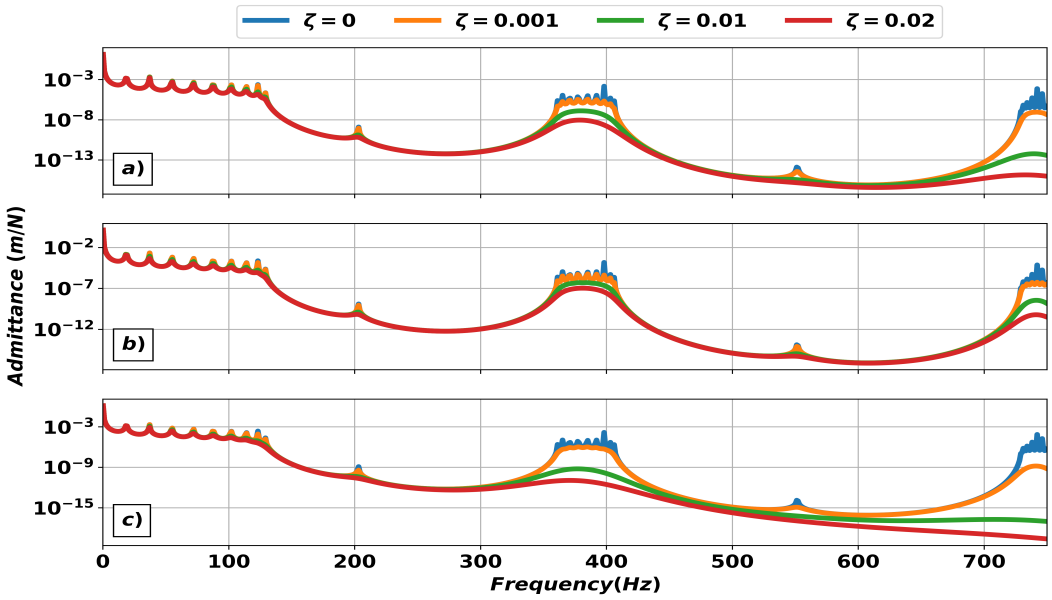

Source: The author.

In Figure 4.38 a) it is observed the FRF using the proportional viscous damping. It is noticed the attenuation of the resonant peaks as the damping ratio values increase. Also, it

is observed that the band gaps do not change in width nor location in the frequency range.

The hysteretic damping model in Figure 4.38 b) possess similar FRF results compared to viscous proportional damping in Figure 4.38 a). Since the damping ratio is the same across all resonant peaks, the attenuation response in higher frequencies is less aggressive compared to the proportional viscous damping.

The viscoelastic damping model in Figure 4.38 c) presents similar results compared to the other damping models. For frequencies above 300 Hz it is noticed that the damping is increased. This fact can be explained by looking at the loss factor plot in Figure 4.37, where the loss factor increases linearly with frequency for non-null damping ratio. The band gaps are also located in the same frequency range regardless of damping ratio value. The storage modulus does not vary too much in the frequency range studied, hence the band gaps width or location in the frequency range are not affected.

The dispersion diagram of all three damping models of the periodic composite rod is shown in Figure 4.39:

Figure 4.39 – Dispersion diagram of composite rod for: a_1) attenuation factor for proportional viscous damping, b_1) phase constant for proportional viscous damping, a_2) attenuation factor for hysteretic damping, b_2) phase constant for hysteretic damping, c_1) attenuation factor for viscoelastic damping, c_2) phase constant for viscoelastic damping

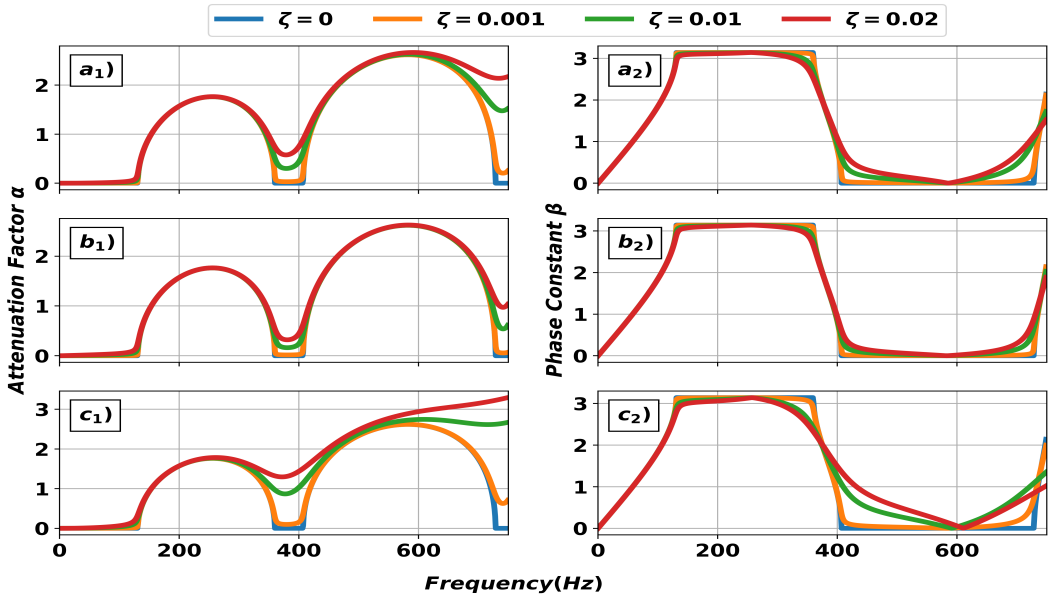

Source: The author.

The dispersion diagram in Figure 4.39 corroborates the FRF of the composite rod obtained in Figure 4.38. Notice the increased attenuation in the passband region of 350-410 Hz of the viscoelastic damping model in Figure 4.38 c_1).

4.2.1.3 Temperature dependency of viscoelastic damping model

In this subsection the effect of temperature on the viscoelastic material is investigated. In the previous section a temperature value of 24 ^{o}C was selected to compare the different damping models. Herein, a temperature range of -23 to 77 ^{o}C is selected, and the effect of temperature dependency in FRF and dispersion diagram is investigated. The form factor of the viscoelastic material is hold constant.

In Figure 4.40 it is depicted the storage modulus and loss factor varying with temperature:

Figure 4.40 – Storage Modulus and Loss Factor for viscoelastic material

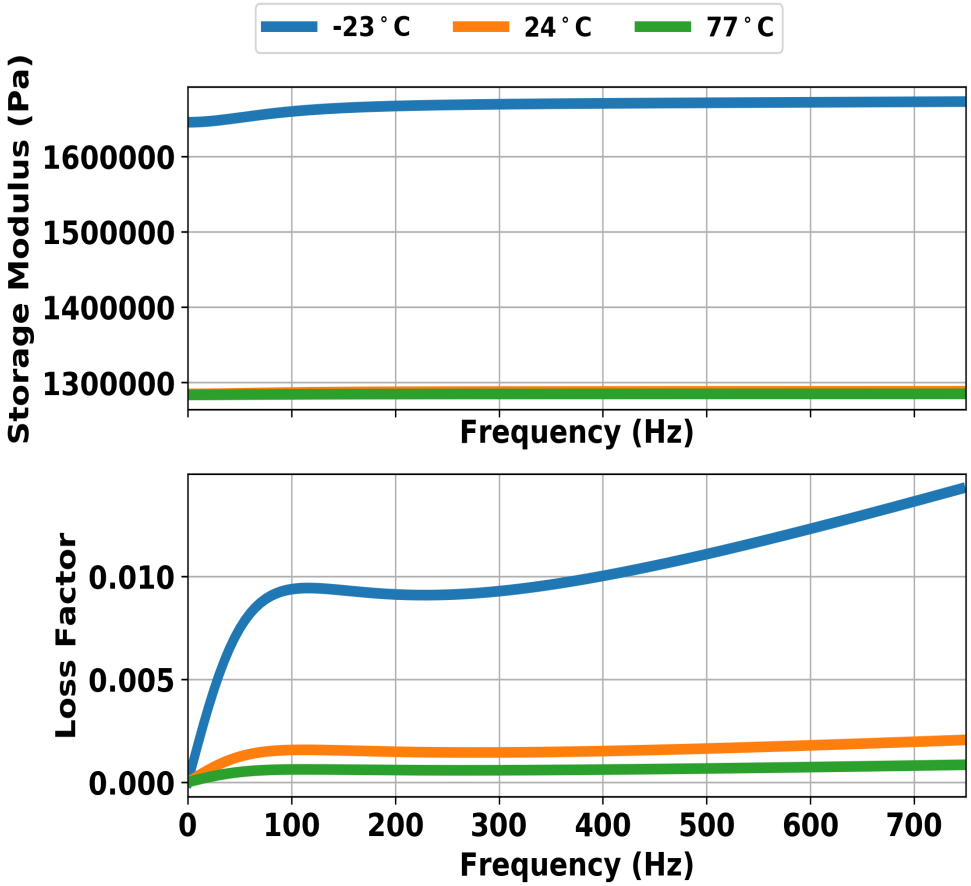

Source: The author.

It is shown in Figure 4.40 that the material storage modulus possess high stiffness and loss factor at low temperatures. It is noticed that the loss factor at the temperature of -23 ^{o}C is greater than 24 ^{o}C and 77 ^{o}C. Hence, as the temperature increases the storage modulus decreases and the loss factor increases its values.

In Figure 4.41 it is observed the effect of temperature in the FRF of the periodic composite rod:

Figure 4.41 – FRF of periodic composite rod subjected to different temperature range

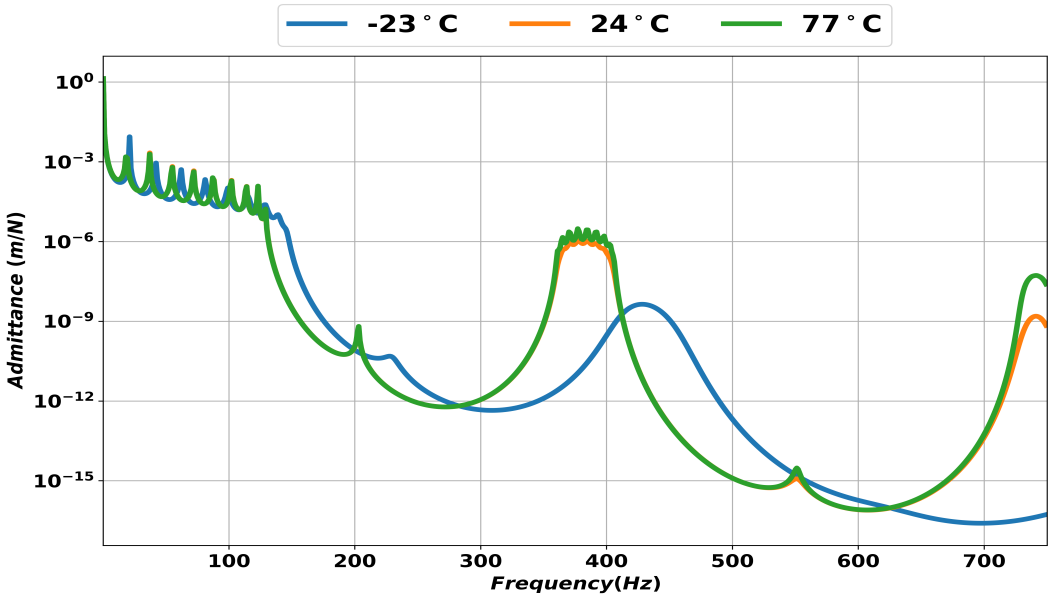

Source: The author.

The FRF of the composite rod in Figure 4.41 shows a shift in the band gaps previously located at the starting frequencies of 130 and 400 Hz. At the temperature of -23 ^{o}C, the viscoelastic material possess high storage modulus and loss factor compared to the temperatures of 24 ^{o}C and 77 ^{o}C, as seen in Figure 4.40. Hence, it is observed a shift in the band gaps towards the lower frequencies as the temperature decreases, as well as more damping due to higher loss factor at low temperatures for this particular material. This fact demonstrates the complex behavior of viscoelastic materials under different temperature and operating frequency, posing a challenge when designing periodic structures with viscoelastic materials. On the other hand, it also implies the control of band gaps location by adjusting the temperature where the composite rod is currently operating.

The dispersion diagram of the composite rod under different temperatures is depicted in Figure 4.42:

Figure 4.42 – Dispersion diagram of periodic composite rod subjected to different temperature range

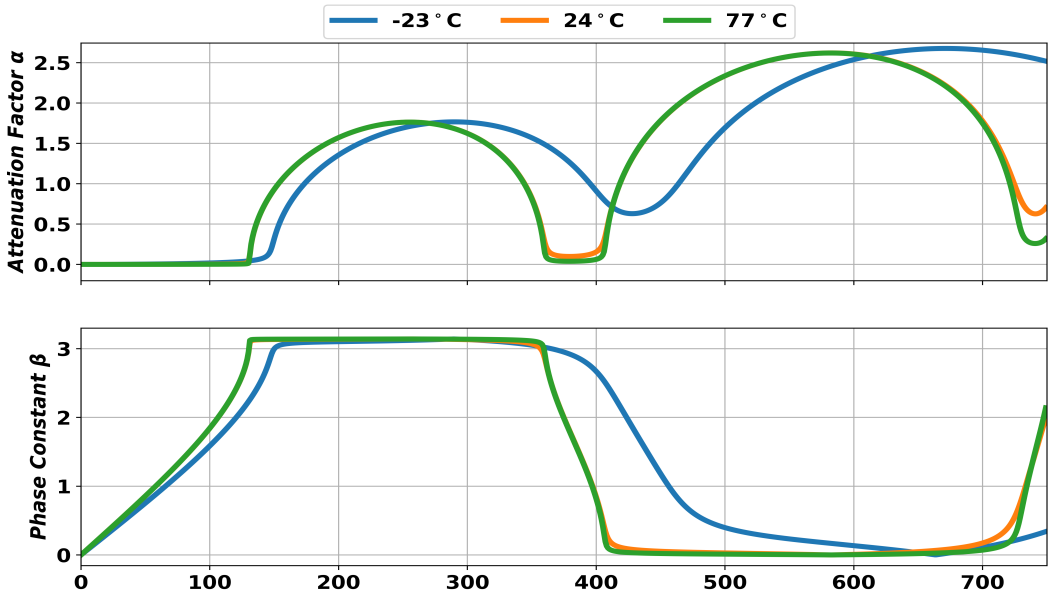

Source: The author.

The dispersion diagram in Figure 4.42 clearly shows the shift in band gaps from right to left as the temperature decreases. Moreover, the effect of the loss factor of is more pronounced at the temperature of -23 ^{o}C, where the pass bands are highly attenuated.

The following observations for the sandwich rod are:

- The damping models applied to the sandwich rod did not influence the location nor width of band gaps, except when using the frequency-temperature dependency of the viscoelastic material.
- Similar to the case of discrete systems, the damping models influence the level of attenuation of pass bands.
- The viscoelastic damping model provided more attenuation at higher frequencies, followed by the proportional viscous damping. This high level of attenuation leads to the formation of the band gap merging phenomenon.
- In the case of rod, it is sufficient to study band gaps using the discrete system cases, as the results obtained herein are similar, especially when comparing to Case 1 and 2.

4.2.2 Periodic Sandwich Beam

Sandwich beams are widely used in automotive, marine, civil and other high performance structures due to their specific strength and stiffness, fatigue resistance and other superior properties compared to conventional metallic structures (PRASAD *et al.*, 2014). The sandwich beam is composed of two face sheets with high strength and middle core with low

strength and low density (GUO; SHENG; PAN, 2017). These structures may vibrate easily due to their low weight, causing noise problems and suffering from fatigue due to increased vibration. However, since periodic structures are able to filter elastic waves over a range of frequencies, the concept will be applied herein. For instance, Badran, Tawfik and Negm (2008) studied different configurations of middle core in the sandwich beam, namely, a homogeneous soft middle core, a homogeneous middle hard core, and a periodic configuration of soft and hard core using six unit cells. In Figure 4.43 it is shown the FRF of the sandwich beam for each configuration:

Figure 4.43 – FRF of sandwich beam for different configurations of material middle core

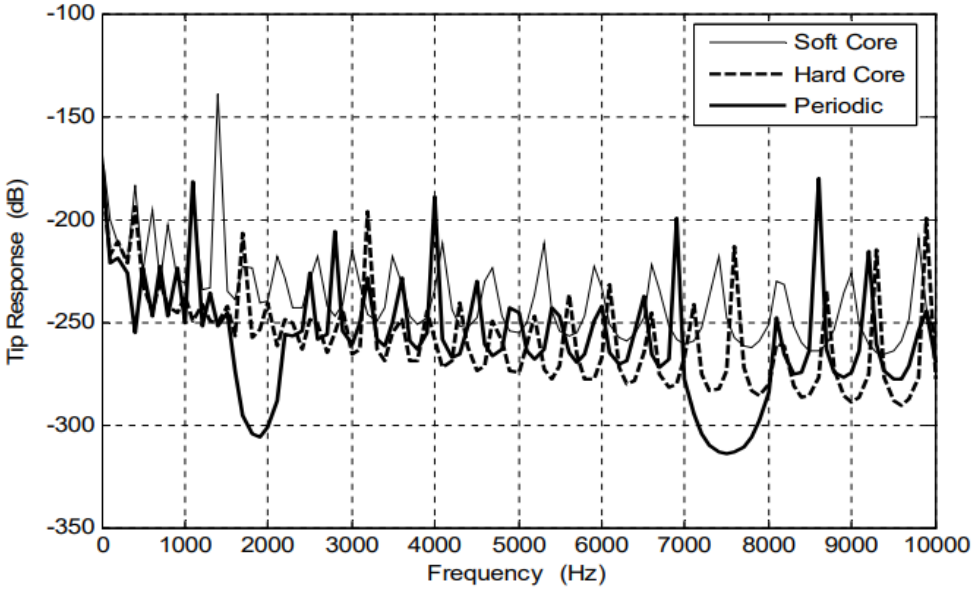

Source: (BADRAN; TAWFIK; NEGM, 2008).

It can be seen that adding material periodicity in the middle core create two band gap regions between 1500 - 2200 Hz and 7000 - 8000 Hz, thus demonstrating the advantage of using periodicity for filtering elastic wave propagation.

In this subsection, two different types of materials will be used in the sandwich beam core, allowing band gaps to occur. Different damping models applied to the core materials are investigated, namely the proportional viscous damping, hysteretic damping and viscoelastic damping. The next subsection will cover the development of the sandwich beam equations using the finite element method for drawing the dispersion diagrams and FRFs.

4.2.2.1 Finite element model of periodic sandwich beam

In this subsection the finite element model of a sandwich beam is derived. The kinematics of the sandwich beam along with its state variables are shown in Figure 4.44:

Figure 4.44 – Kinematics of sandwich beam

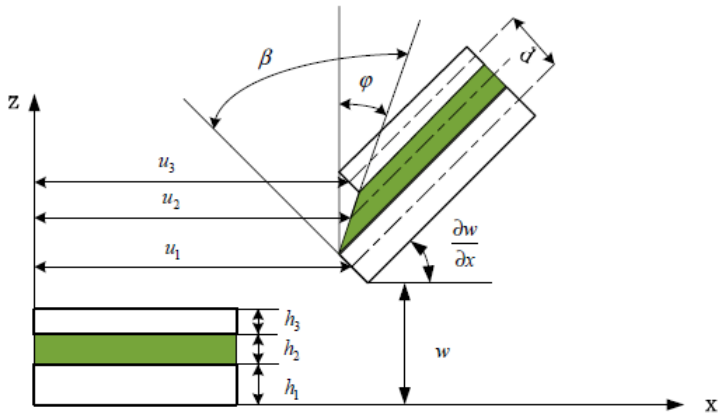

Source: (HUANG *et al.*, 2019).

In Figure 4.44 the thickness of the base beam, viscoelastic layer and constraining layer are represented by h_1, h_2, h_3. The transverse deflection and rotation angle of the sandwich beam are represented by w and $\frac{\partial w}{\partial x}$. The longitudinal displacements for each layer are u_1, u_2 and u_3. The distance of the centerlines is d and finally, the shear angle and shear strain are stated by φ and β.

It can be shown that the displacements of the top and bottom surface of the viscoelastic layer are given by Eq. (4.29) (HUANG *et al.*, 2019):

$$\begin{aligned} u_{top} &= u_3 + \frac{h_3}{2}\frac{\partial w}{\partial x} \\ u_{bottom} &= u_1 - \frac{h_1}{2}\frac{\partial w}{\partial x} \end{aligned} \tag{4.29}$$

The displacement of the viscoelastic layer in the x direction is expressed by Eq. (4.30):

$$u_2 = \frac{u_{top} + u_{bottom}}{2} \tag{4.30}$$

The mid-plane displacement of the viscoelastic layer in the x direction is obtained by substituting Eq. (4.29) in Eq. (4.30):

$$u_2 = \frac{1}{2}\left[(u_3 + u_1) + \frac{h_3 - h_1}{2}\frac{\partial w}{\partial x}\right] \tag{4.31}$$

Using the geometric relation of the sandwich beam, the shear angle of the viscoelastic layer in the y-axis is given by:

$$\varphi = \frac{u_{top} - u_{bottom}}{h_2} \tag{4.32}$$

The mid-plane shear angle is then obtained by substituting Eq. (4.29) in Eq. (4.32):

$$\varphi = \frac{1}{h_2}\left[(u_3 - u_1) + \frac{h_3 + h_1}{2}\frac{\partial w}{\partial x}\right] \tag{4.33}$$

The shear strain of the viscoelastic layer is given by Eq. (4.34):

$$\beta = \frac{1}{h_2}\left[(u_3 - u_1) + \left(\frac{h_3 + h_1}{2} + h2\right)\frac{\partial w}{\partial x}\right] \tag{4.34}$$

In Figure 4.45 it is shown the sandwich beam element with its degrees of freedom:

Figure 4.45 – Sandwich beam element

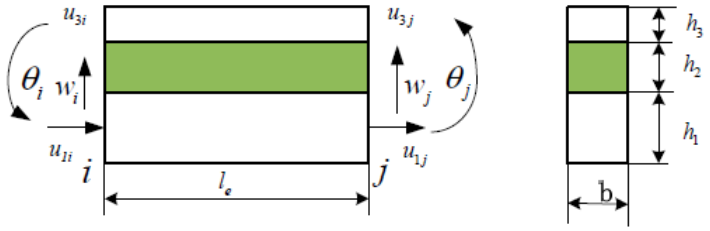

Source: (HUANG *et al.*, 2019).

The nodal degrees of freedom are the transverse displacement w, the longitudinal displacement u and the rotation angle θ. The beam element length is l_e, and the thickness of each layer is h. The displacement at any point of the sandwich beam element is given by the shape interpolation function as follow (HUANG *et al.*, 2019):

$$z^e = [u_{1i}\ \ u_{3i}\ \ w_i\ \ \theta_i\ \ u_{1j}\ \ u_{3j}\ \ w_j\ \ \theta_j]^T \tag{4.35}$$

$$z = [u_1\ \ u_3\ \ w\ \ \theta]^T = \mathbf{N}z^e \tag{4.36}$$

where $\mathbf{N}$ is the shape function matrix, given by $\mathbf{N} = [\mathbf{N_1}\ \ \mathbf{N_2}\ \ \mathbf{N_3}\ \ \mathbf{N_4}]$. The components of the shape function matrix are:

$$\begin{aligned}
\mathbf{N_1} &= \left[\ (1-\chi)\ 0\ 0\ 0\ \chi\ 0\ 0\ 0\ \right] \\
\mathbf{N_2} &= \left[\ 0\ (1-\chi)\ 0\ 0\ 0\ \chi\ 0\ 0\ \right] \\
\mathbf{N_3} &= \left[\ 0\ 0\ (1-3\chi^2+2\chi^3)\ (\chi-2\chi^2+\chi^3)l_e\ 0\ 0\ (3\chi^2-2\chi^3)\ (-\chi^2+\chi^3)l_e\ \right] \\
\mathbf{N_4} &= \left[\ 0\ 0\ \frac{6\chi(\chi-1)}{l_e}\ (1-4\chi+3\chi^2)\ 0\ 0\ \frac{6\chi(1-\chi)}{l_e}\ (-2\chi+3\chi^2)\ \right]
\end{aligned} \tag{4.37}$$

where $\chi = \frac{x}{l_e}$.

The displacements of the sandwich beam element represented by the shape functions in Eq. (4.37) are given by Eq. (4.38):

$$\begin{aligned} u_1 &= \mathbf{N_1} z^e \\ u_3 &= \mathbf{N_2} z^e \\ w &= \mathbf{N_3} z^e \\ \theta &= \mathbf{N_4} z^e \end{aligned} \tag{4.38}$$

The expression for u_2 is obtained by substituting Eq. (4.38) in Eq. (4.31):

$$u_2 = \underbrace{\frac{1}{2}\left[(\mathbf{N_1}+\mathbf{N_2}) + \left(\frac{h_3-h_1}{2}\right)\mathbf{N_4}\right]}_{\mathbf{N_5}} z^e \tag{4.39}$$

Substituting Eq. (4.38) into Eq. (4.34) gives the shear strain represented by shape functions:

$$\beta = \underbrace{\frac{1}{2}\left[(\mathbf{N_1}-\mathbf{N_2}) + \left(\frac{h_1+h_3}{2}\right)\mathbf{N_4}\right]}_{\mathbf{N_6}} z^e \tag{4.40}$$

Next, to obtain the mass and stiffness matrices it is necessary to integrate the strain and kinetic energy of the sandwich beam element. The total strain energy of the system is given by summing the extensional, bending and shear effects, hence:

$$U = U_{e1} + U_{e3} + U_{b1} + U_{b3} + U_s \tag{4.41}$$

where U_{e1} and U_{e3} are the extensional strain energy of the base and constraining layer respectively, U_{b1} and U_{b3} the bending strain energy and U_s the shear strain energy of the viscoelastic layer. The equations for each strain energy are obtained in Eq. (4.42) :

$$\begin{aligned} U_{e1} &= \frac{1}{2}E_1A_1\int_0^{l_e}\left(\frac{\partial u_1}{\partial x}\right)^2 dx = \frac{1}{2}z^{e^T}\mathbf{K^e_{e1}}z^e \\ U_{e3} &= \frac{1}{2}E_3A_3\int_0^{l_e}\left(\frac{\partial u_3}{\partial x}\right)^2 dx = \frac{1}{2}z^{e^T}\mathbf{K^e_{e3}}z^e \\ U_{b1} &= \frac{1}{2}E_1I_1\int_0^{l_e}\left(\frac{\partial^2 w}{\partial x^2}\right)^2 dx = \frac{1}{2}z^{e^T}\mathbf{K^e_{b1}}z^e \\ U_{b3} &= \frac{1}{2}E_3I_3\int_0^{l_e}\left(\frac{\partial^2 w}{\partial x^2}\right)^2 dx = \frac{1}{2}z^{e^T}\mathbf{K^e_{b3}}z^e \\ U_s &= \frac{1}{2}G_2A_2\int_0^{l_e}\beta^2 dx = \frac{1}{2}z^{e^T}\mathbf{K^e_v}z^e \end{aligned} \tag{4.42}$$

The expression for the stiffness matrices are obtained by applying the shape functions, and they are shown in Eq. (4.43):

$$\begin{aligned}
\mathbf{K}^e_{e1} &= E_1 A_1 l_e \int_0^1 \left[\frac{\partial \mathbf{N_1}}{\partial x}\right]^T \left[\frac{\partial \mathbf{N_1}}{\partial x}\right] d\chi \\
\mathbf{K}^e_{b1} &= E_1 I_1 l_e \int_0^1 \left[\frac{\partial^2 \mathbf{N_3}}{\partial x^2}\right]^T \left[\frac{\partial^2 \mathbf{N_3}}{\partial x^2}\right] d\chi \\
\mathbf{K}^e_{e3} &= E_3 A_3 l_e \int_0^1 \left[\frac{\partial \mathbf{N_2}}{\partial x}\right]^T \left[\frac{\partial \mathbf{N_2}}{\partial x}\right] d\chi \\
\mathbf{K}^e_{b3} &= E_3 I_3 l_e \int_0^1 \left[\frac{\partial^2 \mathbf{N_3}}{\partial x^2}\right]^T \left[\frac{\partial^2 \mathbf{N_3}}{\partial x^2}\right] d\chi \\
\mathbf{K}^e_{visco} &= G_2 A_2 l_e \int_0^1 \mathbf{N_6}^T \mathbf{N_6} d\chi
\end{aligned} \tag{4.43}$$

As for the mass matrices, the kinetic energy of the sandwich beam is evaluated by summing the kinetic energies for the base beam, constraining layer and viscoelastic layer. The total kinetic energy is given in Eq. (4.44):

$$T = T_{e1} + T_{e2} + T_{e3} + T_{b1} + T_{b2} + T_{b3} \tag{4.44}$$

where T_{e1}, T_{e2} and T_{e3} are the extensional kinetic energy of the base, viscoelastic and constraining layer respectively, and T_{b1}, T_{b2}, T_{b3} are the bending kinetic energy of each layer. The equations for each kinetic energy are obtained in Eq. (4.45) :

$$\begin{aligned}
T_{e1} &= \frac{1}{2}\rho_1 A_1 \int_0^{l_e} \left(\frac{\partial u_1}{\partial t}\right)^2 dx = \frac{1}{2} z^{e^T} \mathbf{M^e_{e1}} z^e \\
T_{e2} &= \frac{1}{2}\rho_2 A_2 \int_0^{l_e} \left(\frac{\partial u_2}{\partial t}\right)^2 dx = \frac{1}{2} z^{e^T} \mathbf{M^e_{e2}} z^e \\
T_{e3} &= \frac{1}{2}\rho_3 A_3 \int_0^{l_e} \left(\frac{\partial u_3}{\partial t}\right)^2 dx = \frac{1}{2} z^{e^T} \mathbf{M^e_{e3}} z^e \\
T_{b1} &= \frac{1}{2}\rho_1 A_1 \int_0^{l_e} \left(\frac{\partial w}{\partial t}\right)^2 dx = \frac{1}{2} z^{e^T} \mathbf{M^e_{b1}} z^e \\
T_{b2} &= \frac{1}{2}\rho_2 A_2 \int_0^{l_e} \left(\frac{\partial w}{\partial t}\right)^2 dx = \frac{1}{2} z^{e^T} \mathbf{M^e_{b2}} z^e \\
T_{b3} &= \frac{1}{2}\rho_3 A_3 \int_0^{l_e} \left(\frac{\partial w}{\partial t}\right)^2 dx = \frac{1}{2} z^{e^T} \mathbf{M^e_{b3}} z^e
\end{aligned} \tag{4.45}$$

The mass matrices are obtained in a similar fashion:

$$
\begin{aligned}
\mathbf{M}^e_{e1} &= \rho_1 A_1 l_e \int_0^1 \mathbf{N_1}^T \mathbf{N_1} d\chi \\
\mathbf{M}^e_{b1} &= \rho_1 A_1 l_e \int_0^1 \mathbf{N_3}^T \mathbf{N_3} d\chi \\
\mathbf{M}^e_{e2} &= \rho_2 A_2 l_e \int_0^1 \mathbf{N_5}^T \mathbf{N_5} d\chi \\
\mathbf{M}^e_{b2} &= \rho_2 A_2 l_e \int_0^1 \mathbf{N_3}^T \mathbf{N_3} d\chi \\
\mathbf{M}^e_{e3} &= \rho_3 A_3 l_e \int_0^1 \mathbf{N_2}^T \mathbf{N_2} d\chi \\
\mathbf{M}^e_{b3} &= \rho_3 A_3 l_e \int_0^1 \mathbf{N_3}^T \mathbf{N_3} d\chi
\end{aligned}
\tag{4.46}
$$

The expressions for the full stiffness and mass matrices of the sandwich beam element are given in Eq. (4.47):

$$
\begin{aligned}
\mathbf{K}^e &= \underbrace{\mathbf{K}^e_{e1} + \mathbf{K}^e_{b1} + \mathbf{K}^e_{e3} + \mathbf{K}^e_{b3}}_{\mathbf{K}^e_{elastic}} + \mathbf{K}^e_{visco} \\
\mathbf{M}_e &= \mathbf{M}^e_{e1} + \mathbf{M}^e_{b1} + \mathbf{M}^e_{e2} + \mathbf{M}^e_{b2} + \mathbf{M}^e_{e3} + \mathbf{M}^e_{b3}
\end{aligned}
\tag{4.47}
$$

With the stiffness and mass matrices ready, it is now possible to apply the damping models of section 4.2.1. For the viscoelastic damping specifically, the $\mathbf{K}_{elastic}$ and $\mathbf{K}_{visco}$ of Eq. (4.47) are plugged respectively in the matrices $\mathbf{K}_s$ (representing the elastic portion) and $\mathbf{K}_v$ (representing the visco portion) of Eq. (3.34).

4.2.2.2 Results for sandwich beam

The sandwich beam core will be modeled using two different materials, the soft material ISD 112 and the hard viscoelastic material LD-400 from (SOOVERE; DRAKE, 1985). The sandwich beam dimensions and material properties are listed in Table 4.4 below:

Table 4.4 – Periodic sandwich beam material parameters at 24 °C.

Parameter	ALUMINUM (BASE)	ISD 112	LD-400	ALUMINUM (CONSTRAINT LAYER)
E (GPa)	70	0.0013	0.16	70
G (GPa)	25.9	0.00043	0.053	25.9
L (m)	0.6	0.3	0.3	0.6
A (m^2)	1 x 10^{-4}	2.5 x 10^{-4}	2.5 x 10^{-4}	1 x 10^{-4}
d (kg/m^3)	2700	1000	1000	2700

Source: The author.

The viscoelastic parameters for ISD 112 were listed in Table 4.3 whereas the viscoelastic parameters for the LD-400 are listed in Table 4.5:

Table 4.5 – Viscoelastic Parameters for LD-400 at 24 °C.

Parameter	Value	Unit
ρ_i	[6.7 x 10^{-5}, 6.9 x 10^{-4}, 4 x 10^{-3}, 1.4 x 10^{-2}, 6.8 x 10^{-1}]	s
α_i	[18.7, 18.7, 18.7, 18.7, 12.2]	dimensionless

Source: The author.

Following the same steps of the composite rod in section 4.2.1, the FRF and dispersion diagrams for each damping model are obtained. Since the sandwich beam have rotational, longitudinal and flexural degrees of freedom, only the flexural band gaps and the effect of damping models on those will be investigated. Moreover, the solution of the eigenvalue problem in Eq. (2.13) leads to an eigenvalue tracking problem, where it becomes difficult to track the correct branch along the frequencies due to branch crossing and veering (COLLET *et al.*, 2011). In this case, only the attenuation factor of the sandwich beam is plotted.

The master curves of ISD 112 and LD-400 for selected damping ratios are plotted below:

Figure 4.46 – Master curve of ISD 112 for different damping ratio values and reference temperature of 24 °C

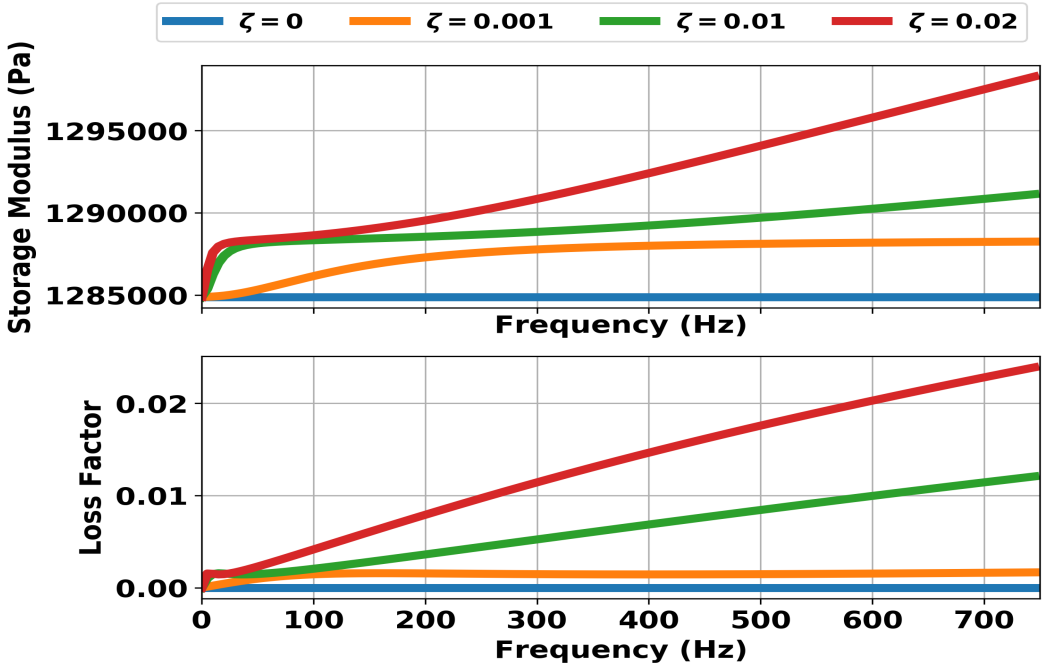

Source: The author.

Figure 4.47 – Master curve of LD-400 for different damping ratio values and reference temperature of 24 ^{o}C

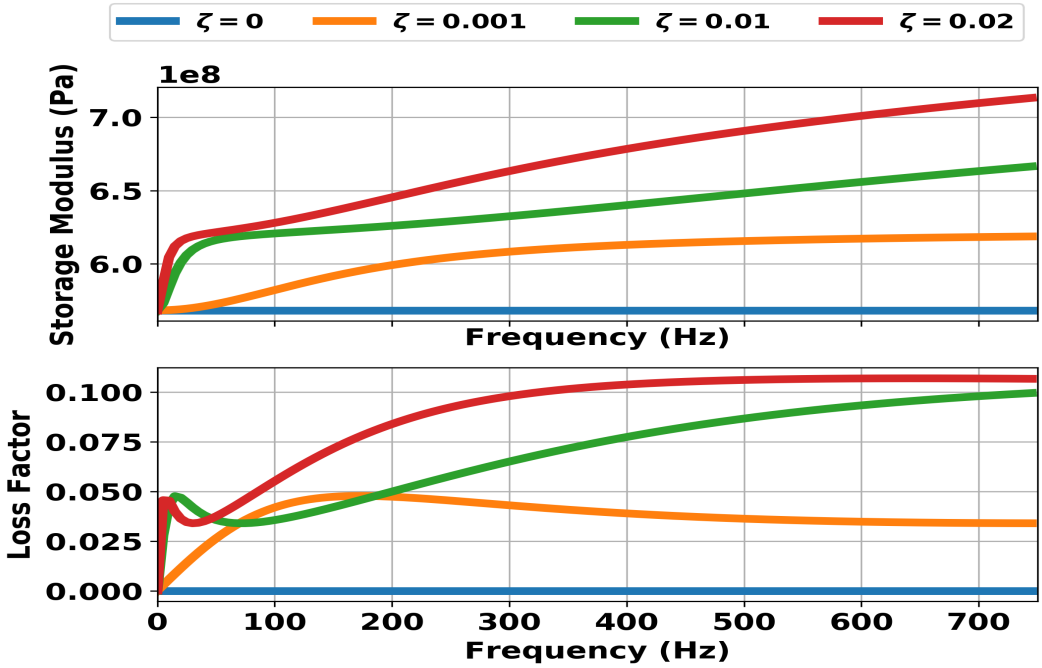

Source: The author.

The effect of each damping model on the FRF are observed in Figure 4.48:

Figure 4.48 – FRF of periodic sandwich beam for: a) proportional viscous damping, b) hysteretic damping and c) viscoelastic damping

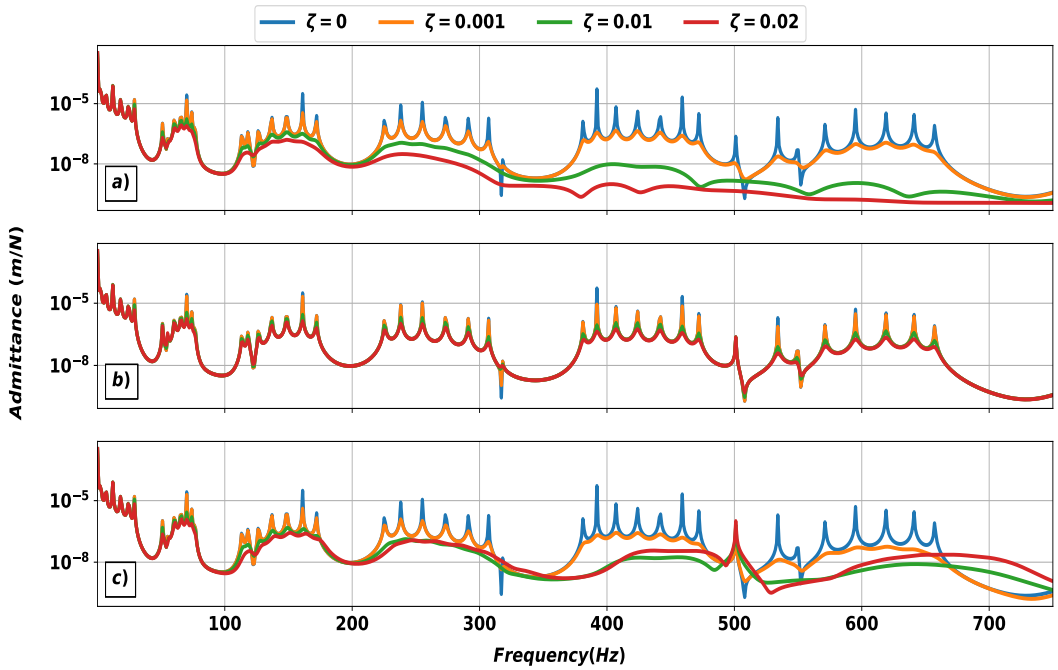

Source: The author.

In Figure 4.48 a) it is observed the effect of proportional viscous damping in the FRF

response for different damping ratio values. The level of vibration attenuation increases with frequency, as expected from Eq. (3.17). For the hysteretic damping model in Figure 4.48 b), the vibration attenuation around the resonance across the frequencies are the same. This behavior is given by Eq. (3.20). Finally, the viscoelastic damping model presents an increase in vibration attenuation with frequency similar to that of the proportional viscous damping. Around the frequency of 400-500 Hz and beyond it can be seem the vibration attenuation resembling Case 3 in section 4.1.3 and Case 4 in section 4.1.4 where an increased damping ratio raises the level of vibration around the resonances.

The dispersion diagram for each damping model is depicted in Figure 4.49:

Figure 4.49 – Dispersion diagram showing the attenuation factor of sandwich beam under various damping ratios for a) proportional viscous damping, b) hysteretic damping and c) viscoelastic damping

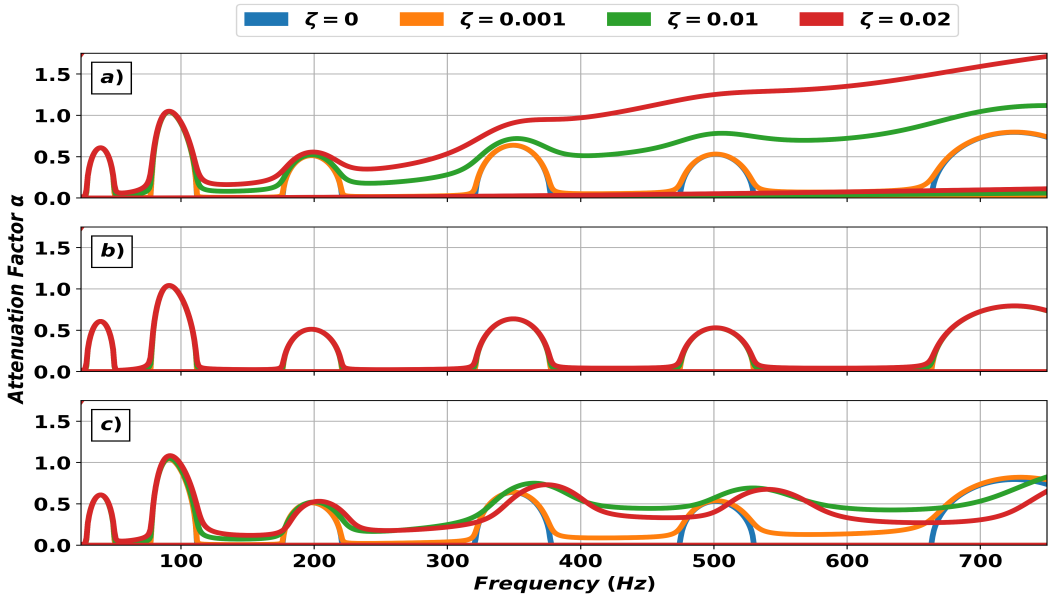

Source: The author.

In Figure 4.49 a) it is observed that the attenuation increases with frequency, which is in accordance to Eq. (3.17). No shift in band gaps are presented, and it is possible to observe the band gap merging phenomenon due to the high level of damping of the pass band starting from 100 Hz for $\zeta = 0.01$ and $\zeta = 0.02$. Next, the hysteretic damping model in Figure 4.49 b) shows almost no effect on the attenuation factor for different damping ratios, possibly due to presenting the same damping ratio in the resonant peaks regardless of frequency, as seen in Eq. (3.20). Finally, the viscoelastic damping model in Figure 4.49 c) shows increased attenuation when the operational frequency is increased. It is also observed the shifts in band gaps for $\zeta = 0.01$ and $\zeta = 0.02$. These shifts in band gaps are explained by the elevated change in the stiffness of the VEM cores, as observed in Figure 4.46 and Figure 4.47.

The effect of temperature is investigated herein. In figure below we plot the master curves for ISD 112 and LD 400 for different temperatures:

Figure 4.50 – Master Curve of ISD at different temperatures

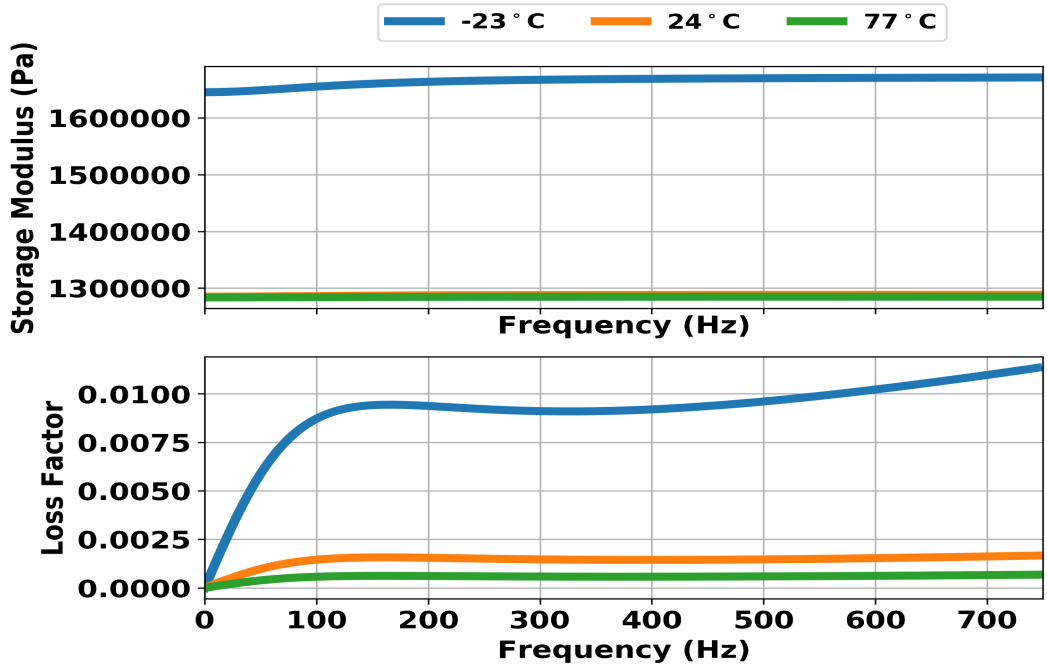

Source: The author.

Figure 4.51 – Master Curve of LD-400 at different temperatures

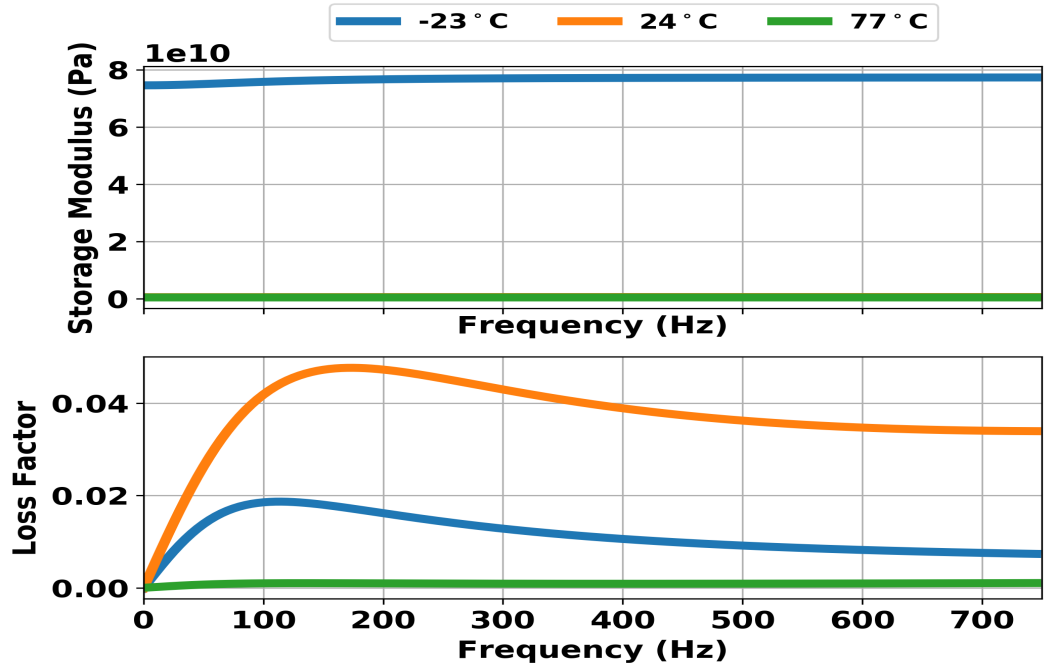

Source: The author.

The effect of temperature in FRF of the periodic sandwich beam at different temperatures is depicted in Figure 4.52:

Figure 4.52 – FRF of periodic sandwich beam at various temperature levels

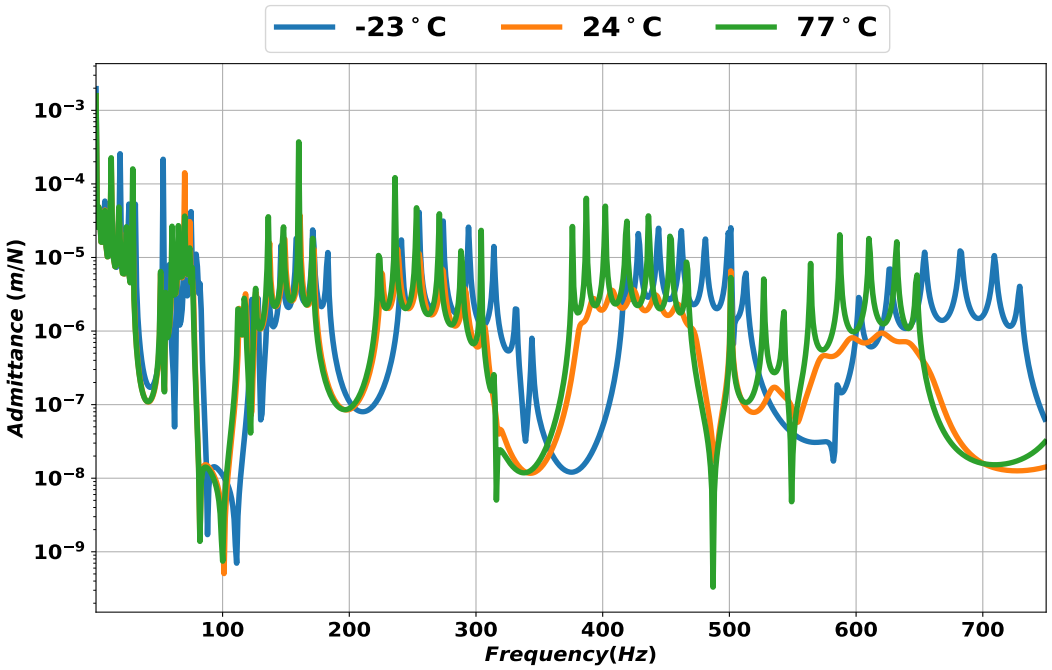

Source: The author.

It is concluded from Figure 4.52 that the band gaps are shifted when the temperature increases. Also, it is possible to notice the maximum attenuation is obtained at 24 ^{o}C. This attenuation is mainly driven by the loss factor of LD-400, which attain maximum value at 24 ^{o}C. The dispersion diagram in Figure 4.53 showing the attenuation factor of the sandwich beam illustrates the shift in band gaps according to temperature:

Figure 4.53 – Dispersion diagram showing the attenuation factor of the periodic sandwich beam

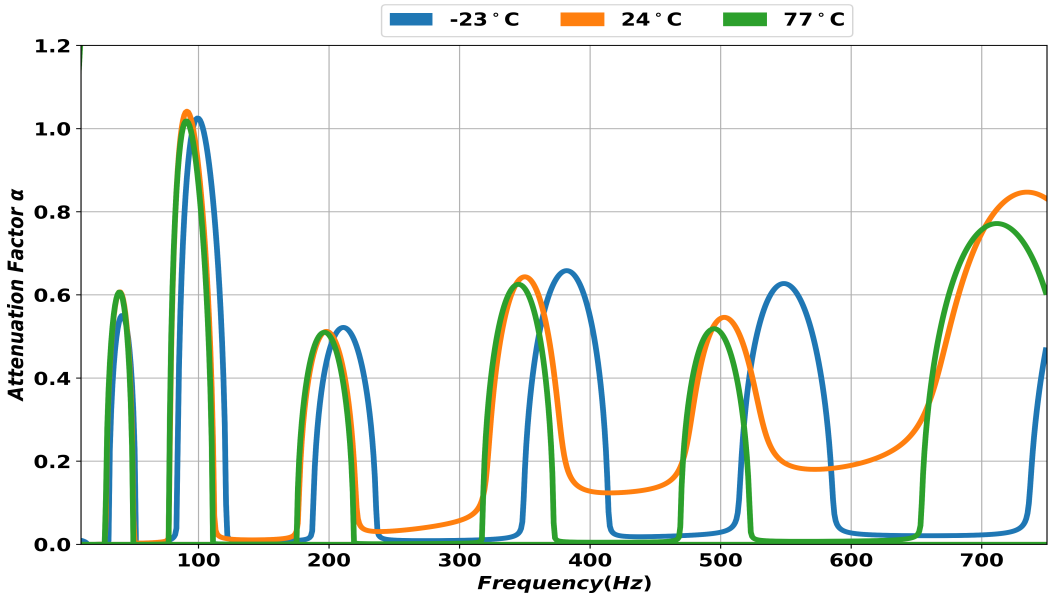

Source: The author.

From the dispersion diagram showing the attenuation factor in Figure 4.53 it is concluded that the band gaps shift to the range of lower frequencies as the temperature decreases. The attenuation increases for higher frequencies at the temperature of 24 ^{o}C, mainly due to the high loss factor of LD-400.

Hence, the following observations are made for periodic sandwich beams:

- Six band gap regions were observed in the frequency range of 0 - 750 Hz.
- The proportional viscous and viscoelastic damping models created the band gap merging phenomenon starting from a frequency of 200 Hz. This is explained by the fact that in both models the damping ratio (or loss factor) increases for higher frequencies.
- It was observed shift in band gaps for the viscoelastic damping model when varying the damping ratio. This is possible explained by the change in stiffness of LD-400 and ISD 112 with frequency.
- The hysteretic damping did not provide any change in band gaps. Only a small level of attenuation was observed in the pass bands.
- Shift in band gaps were observed using the viscoelastic damping model with frequency-temperature dependency, similar to what was observed with the periodic composite rod.

Overall, adding a damping model to periodic continuous systems change the behavior of dispersion curves. Hence, the analyst must take damping into account when designing periodic structures to suppress sound or vibration at desired frequencies, especially when using viscoelastic materials, where temperature plays a major role in the location of band gaps in the frequency range.

Chapter 5

Conclusion

In this dissertation, different types of damping models and their effect on band gaps and pass bands of periodic structures were investigated. In particular, these damping models were added to lumped mass spring damper systems and continuous systems, and the dispersion curves and frequency response function were calculated for each case.

A revision of the bibliography of metamaterials was made, showing different usages of this class of materials. Periodic materials fall into the class of metamaterials, and they can be used to filter elastic waves, thus reducing vibration level. An introduction of periodic materials was discussed, and the transfer matrix method was used to model the periodic structure. The transfer matrix method was applied to a periodic beam, where the pass bands, band gaps and frequency response function were calculated. There was excellent agreement between inhouse code and Ansys Workbench regarding the location of band gaps, and these results were also validated with previous works on periodic beams.

Different damping models were discussed in this dissertation, along with their impact on band gaps and pass bands of periodic materials. Since most of the studies on energy dissipation in periodic structures focus on the $\omega(k)$ approach, the alternative approach $k(\omega)$ is chosen, as it is commonly found in engineering problems where a harmonic excitation is present.

The first damping model introduced was the viscous damping, divided into proportional viscous damping, also called classical Rayleigh, where the damping matrix is a linear combination of the mass and stiffness matrix, and non-proportional viscous damping. For the phononic crystals studied in this dissertation, it was shown that both damping models eliminate the pass bands regions, as the attenuation factor becomes different from zero in the frequency intervals where a pass band was located with undamped phononic crystals. This elimination of pass bands creates a band gap merging phenomenon. For the phase constant diagrams, it was shown that the phase constant values do not reach the bounding values of zero and π when the damping ratio value increases. In the case of metamaterials,

damping decreases the local resonance admittance values, thus helping on the propagation of elastic waves across the structure. This result is corroborated with the depicted dispersion curves, especially when looking at the attenuation factor diagram.

The second damping model studied was the hysteretic damping, characterized by the loss factor η of the material. Similar results compared to viscous damping models were obtained for phononic crystals and metamaterials. Since the damping ratio value is the same regardless of frequency, the same level of attenuation is observed for all the resonant frequencies of phononic crystals and metamaterials.

The last damping model investigated was the viscoelastic damping model, characterized by variation in storage modulus and loss factor within frequency and temperature. It was shown that the band gaps are shifted in frequency when the temperature increases due to changes in the storage modulus. This behavior is noticed in both lumped and continuous systems. Moreover, it was also shown that the attenuation level and phase constant of the structure also varies with frequency and temperature.

REFERENCES

ASIRI, S.; ALJAWI, A. Periodic mounts to isolate the vibrations of automotive vehicle engine. *Engineering Sciences*, Scientific Publishing Center, v. 17, n. 1, 2006. Cited 2 times in pages 18 and 20.

ASIRI, S. A.; AL-ZAHRANI, Y. Z. Theoretical Analysis of Mechanical Vibration for Offshore Platform Structures. *World Journal of Mechanics*, 2014. ISSN 2160-049X. Cited in page 21.

ASSOUAR, M. B. *et al.* Broadband plate-type acoustic metamaterial for low-frequency sound attenuation. *Applied Physics Letters*, American Institute of Physics, v. 101, n. 17, p. 173505, 2012. Cited in page 20.

BADRAN, H.; TAWFIK, M.; NEGM, H. Vibration characteristics of periodic sandwich beams. In: *Proceedings of the 13th International Conference on Applied Mechanics and Mechanical Engineering*. [S.l.: s.n.], 2008. Cited in page 88.

BAHRAINI, S. M. S. *et al.* Large deflection of viscoelastic beams using fractional derivative model. *Journal of Mechanical Science and Technology*, Springer, v. 27, n. 4, p. 1063–1070, 2013. Cited in page 45.

BANERJEE, B. *An introduction to metamaterials and waves in composites*. [S.l.: s.n.], 2011. ISSN 13697021. ISBN 9781439841587. Cited in page 17.

BAZ, A. M. *Active and Passive Vibration Damping*. [S.l.: s.n.], 2019. Cited 4 times in pages 31, 44, 45 and 46.

BEARDS, C.; MIOA, M. Structural Vibration: Analysis and Damping. *Elsevier*, 1996. ISSN 0264682X. Cited 2 times in pages 42 and 43.

BELLE, L. V. Vibro-acoustic performance of locally resonant metamaterials with damping. 2019. Cited 2 times in pages 23 and 30.

BRILLOUIN, L. Wave Propagation in Periodic Structures: electric filters and crystal lattices. *Nature*, 1946. ISSN 0028-0836. Cited in page 18.

CAUGHEY, T. K.; O'KELLY, M. E. Classical normal modes in damped linear dynamic systems. *Journal of Applied Mechanics, Transactions ASME*, 1964. ISSN 15289036. Cited in page 40.

CHAKRABORTY, B. C.; RATNA, D. *Polymers for vibration damping applications*. [S.l.]: Elsevier, 2020. Cited 2 times in pages 43 and 44.

CHEN, Y. *et al.* Dissipative elastic metamaterials for broadband wave mitigation at subwavelength scale. *Composite Structures*, Elsevier, v. 136, p. 358–371, 2016. Cited in page 22.

COLLET, M. *et al.* Floquet–bloch decomposition for the computation of dispersion of two-dimensional periodic, damped mechanical systems. *International Journal of Solids and Structures*, Elsevier, v. 48, n. 20, p. 2837–2848, 2011. Cited in page 94.

CUI, T. J.; LIU, R.; SMITH, D. R. *Introduction to Metamaterials*. Boston, MA: Springer US, 2010. 1–19 p. ISBN 978-1-4419-0572-7. Cited in page 17.

DEYMIER, P. A. *Acoustic Metamaterials and Photonic Crystals*. [S.l.: s.n.], 2013. 1–386 p. ISBN 9783642312311. Cited in page 17.

DOMADIYA, P. G. *et al.* Numerical and experimental investigation of stop-bands in finite and infinite periodic one-dimensional structures. *Journal of Vibration and Control*, SAGE Publications Sage UK: London, England, v. 22, n. 4, p. 920–931, 2016. Cited in page 30.

DOYLE, J. F. *Static and dynamic analysis of structures: with an emphasis on mechanics and computer matrix methods*. [S.l.]: Springer Science & Business Media, 1991. v. 6. Cited in page 80.

FARZBOD, F. Analysis of Bloch Formalism In Undamped And Damped Periodic Structures. v. 3, n. October, 2010. Cited in page 22.

FRAZIER, M. J. Dissipative Wave Propagation in Phononic Crystals and Metamaterials: Models and Analysis. *ProQuest Dissertations and Theses*, p. 141, 2015. Cited 3 times in pages 19, 23 and 25.

FRISWELL, M. I.; INMAN, D. J.; LAM, M. J. On the realisation of ghm models in viscoelasticity. *Journal of Intelligent Material Systems and Structures*, TECHNOMIC PUBLISHING CO., INC. 851 New Holland Ave., Box 3535, Lancaster, PA . . . , v. 8, n. 11, p. 986–993, 1997. Cited in page 45.

GOPALAKRISHNAN, S. *Wave propagation in materials and structures*. [S.l.]: Crc Press, 2016. Cited in page 34.

GUO, H. *et al.* Power flow analysis in a hybrid phononic crystal structure. *Chinese Physics B*, IOP Publishing, v. 27, n. 3, p. 036302, 2018. Cited in page 23.

GUO, Z.; SHENG, M.; PAN, J. Flexural wave attenuation in a sandwich beam with viscoelastic periodic cores. *Journal of Sound and Vibration*, Elsevier, v. 400, p. 227–247, 2017. Cited in page 88.

HUANG, Z. *et al.* A finite element model for the vibration analysis of sandwich beam with frequency-dependent viscoelastic material core. *Materials*, Multidisciplinary Digital Publishing Institute, v. 12, n. 20, p. 3390, 2019. Cited 2 times in pages 89 and 90.

HUSSEIN, M.; KHAJEHTOURIAN, R.; ABEDINNASAB, M. Finite-strain bloch wave propagation by the transfer matrix method. *arXiv preprint arXiv:1412.2131*, 2014. Cited in page 30.

HUSSEIN, M. I.; FRAZIER, M. J. Band structure of phononic crystals with general damping. *Journal of Applied Physics*, v. 108, n. 9, 2010. ISSN 00218979. Cited in page 23.

IDESMAN, A.; NIEKAMP, R.; STEIN, E. Finite elements in space and time for generalized viscoelastic maxwell model. *Computational Mechanics*, Springer, v. 27, n. 1, p. 49–60, 2001. Cited in page 45.

INJETI, S. S.; DARAIO, C.; BHATTACHARYA, K. Metamaterials with engineered failure load and stiffness. *Proceedings of the National Academy of Sciences of the United States of America*, 2019. ISSN 10916490. Cited in page 17.

KHELIF, A.; ADIBI, A. *Phononic crystals*. [S.l.]: Springer, 2015. Cited in page 18.

KRATTIGER, D.; PHANI, A. S.; HUSSEIN, M. I. Wave propagation in damped lattice materials. *Dynamics of Lattice Materials*, John Wiley & Sons, Ltd Chichester, UK, p. 93–106, 2017. Cited in page 24.

KULIK, V.; BOIKO, A. Physical principles of methods for measuring viscoelastic properties. *Journal of Applied Mechanics and Technical Physics*, Springer, v. 59, n. 5, p. 874–885, 2018. Cited in page 47.

LIANG, Z.; LEE, G. C. Damping of Structures : Part 1 - Theory of Complex Damping by. *National Center for Earthquake Engineering Research*, 1991. Cited in page 41.

MEAD, D. J. Free wave propagation in periodically supported, infinite beams. *Journal of Sound and Vibration*, 1970. ISSN 10958568. Cited in page 18.

MEAD, D. J. A new method of analyzing wave propagation in periodic structures; applications to periodic timoshenko beams and stiffened plates. *Journal of Sound and Vibration*, Elsevier, v. 104, n. 1, p. 9–27, 1986. Cited in page 33.

MELLOTT, E. *Evaluating boom height control performance with variable boom roll damping in a suspended boom system on self-propelled sprayers*. Thesis (Doctorate) — Iowa State University, 2019. Cited in page 35.

PENDRY, J. B. Negative refraction makes a perfect lens. *Physical Review Letters*, 2000. ISSN 00319007. Cited in page 17.

PHANI, A. S.; HUSSEIN, M. I. *Dynamics of lattice materials*. [S.l.]: John Wiley & Sons, 2017. Cited in page 30.

PRASAD, M. S. *et al.* Analysis of sandwich beam. *International Journal of Science Engineering and Advance Technology*, v. 2, n. 12, p. 901–908, 2014. Cited in page 87.

RAO, S. *Mechanical Vibrations, eBook in SI Units*. Pearson Education, 2017. ISBN 9781292178615. Available in: <https://books.google.com.br/books?id=REQ4DwAAQBAJ>. Cited in page 80.

RUDYKH, S.; BOYCE, M. C. Transforming wave propagation in layered media via instability-induced interfacial wrinkling. *Physical Review Letters*, 2014. ISSN 00319007. Cited in page 17.

RUI, X.; WANG, G.; ZHANG, J. *Transfer matrix method for multibody systems: theory and applications*. [S.l.]: John Wiley & Sons, 2018. Cited in page 28.

SIGALAS, M. M.; ECONOMOU, E. N. *Elastic and acoustic wave band structure*. 1992. Cited in page 18.

SILVA, C. W. de. *Vibration Damping, Control, and Design*. [S.l.: s.n.], 2007. 600 p. Cited in page 35.

SONTI, V. R.; NARAYANA, T. Propagation constants from the response of a finite periodic beam. *Noise control engineering journal*, [Poughkeepsie, NY: Institute of Noise Control Engineering, c1982-, v. 54, n. 3, p. 194–200, 2006. Cited in page 30.

SOOVERE, J.; DRAKE, M. *Aerospace Structures Technology Damping Design Guide. Volume 3. Damping Material Data*. [S.l.], 1985. Cited in page 93.

WAN, Q.; SHAO, C.; CHENG, Y. A hybrid phononic crystal for roof application. *The Journal of the Acoustical Society of America*, Acoustical Society of America, v. 142, n. 5, p. 2988–2995, 2017. Cited 2 times in pages 20 and 21.

WANG, C. *et al.* Study on bandgap characteristics of particle damping phononic crystal. *Applied Acoustics*, Elsevier, v. 166, p. 107352, 2020. Cited in page 24.

WU, B. I. *et al.* A study of using metamaterials as antenna substrate to enhance gain. *Progress in Electromagnetics Research*, 2005. ISSN 10704698. Cited in page 17.

YILMAZ, C.; HULBERT, G. M. Dynamics of locally resonant and inertially amplified lattice materials. *Dynamics of Lattice Materials; Phani, AS, Hussein, MI, Eds*, p. 233, 2017. Cited in page 30.

ZHAO, Y. P.; WEI, P. J. The band gap of 1D viscoelastic phononic crystal. *Computational Materials Science*, Elsevier B.V., v. 46, n. 3, p. 603–606, 2009. ISSN 09270256. Cited in page 22.

ZHENG, L.; LI, Y.-n.; BAZ, A. Attenuation of wave propagation in a novel periodic structure. *Journal of Central South University*, v. 18, n. 2, p. 438–443, apr 2011. ISSN 2095-2899. Cited in page 23.